COMPACT MUON SOLENOID EXPERIMENT DISCOVERY POTENTIAL FOR SUPERSYMMETRY IN SAME-CHARGE DI-LEPTON EVENTS

By

YURIY ALEKSANDROVICH PAKHOTIN

A DISSERTATION PRESENTED TO THE GRADUATE SCHOOL
OF THE UNIVERSITY OF FLORIDA IN PARTIAL FULFILLMENT
OF THE REQUIREMENTS FOR THE DEGREE OF
DOCTOR OF PHILOSOPHY

UNIVERSITY OF FLORIDA

2010

To Natalia, who has encouraged me and believed in me from the very beginning

ACKNOWLEDGMENTS

I would like to thank my adviser, Prof. Guenakh Mitselmakher, for his support, encouragement, instructions and patient pointing me to the goal. I believe his advises shaped my personality and improved myself in many different ways. I want to thank Prof. Andrey Korytov. This thesis would never has been finished (or even has been started) without his help, support and invaluable contribution. I am grateful to Prof. Konstantin Matchev for theoretical guidance of this work and all time he spent explaining me the essence of Supersymmetry. I would like to thank Prof. Darin Acosta for all his help, and advises. I thank Prof. Vladimir Rakov who kindly agreed to become an external member of my committee and review this work.

Thanks to all people whose help I have received. I thank Richard Cavanaugh (now at the University of Illinois at Chicago) for his help, support and contribution into the analysis from the very beginning, for his patience while introducing me to the basics of CMS software and data management. I thank Bobby Scurlock with whom I started this analysis. His physics and software advises were really helpful.

This thesis would be unfinished without hard work and important contributions made by Didar Dobur and Ronny Remington. I am really thankful to them. I would like to thank Alexey Drozdetskiy, Khristian Kotov and Victor Barashko for numerous answers on my questions and important advises they gave me. I want to thank John Yelton, Paul Avery, Ivan Furic, Dayong Wang, Mingshui Chen, Trey Sellers, Lana Muniz, Sean Goldberg, Joe Gartner, Gian Piero Di Giovanni, Jonatan Piedra, Nick Kypreos, Michael Schmitt, Valdas Rapsevicius for all help I received from them.

I would like to thank all UF Tier2 and HPC people Bockjoo Kim, Dimitri Bourilkov, Yujun Wu, Yu Fu, Charlie Taylor, Craig Presscott and Jorge Rodriguez (now at the Florida International University) for keeping very complex computer system running and providing smooth access to it.

I am grateful to former conveners of the CMS SUSY group, Maria Spiropulu and Luc Pape, for introducing me to the community and providing support for my work. I would like to thank all current and recent conveners of the CMS SUSY group, Jeff Richman, Alex Tapper, David Stuart, Frederic Ronga, Oliver Buchmuller and Sarah Eno for their guidance and valuable feedback on this work. I acknowledge as well all other CMS colleagues from whom I received help concerning different physics and computing issues.

I would like to thank UF, Fermilab and CERN assistant staff who were always helpful and supportive in solving different technical and organizational issues. I am really honored to be a part of these great institutions together with them.

I am grateful to Professors and Instructors of Physics Department at the Novosibirsk State University and Physics Department at the University of Florida. The impact that these instructors have had on my education and life is invaluable.

A debt of gratitude is owed to late Prof. Guram Kezerashvili who was my adviser at the Budker Institute for Nuclear Physics at Novosibirsk. He introduced me into the world of the experimental High Energy Physics. His passion for physics will encourage me for the rest of my life. His memory will never be forgotten, at least not in my heart. During my five years in the BINP I have been privileged to work with Elena Kremyanskaya, Nikolai Muchnoi and Anton Bogomyagkov, who I am truly thankful for collaboration.

I am grateful to my school teachers Irina Lapina and Raisa Balabanova. Irina revealed to me the beauty and logical elegance that physics is. Raisa built broad and deep foundation of my mathematical knowledge.

I want to thank my friend, Gena Kukartsev, for interesting discussions and valuable advises. His help and firm support over last 15 years is invaluable. I thank my friend, Denis Filimonov, for sharing his time and spirit (in all senses) with me. Whenever I was in need he always was there to help.

I would like to thank my friends, (Rom)An En Khvan and Denis Esin, for keeping my home-city running. Whenever I am back to Novosibirsk I always know that they are glad to see me. It is really supportive.

Thanks to Prof. David Denslow of Economics Department at the University of Florida for being graduate advisor of my wife in her successful pursuit of PhD degree in Economics. I am truly grateful for his infinite kindness, care and support.

I am thankful to my dear parents, Natalya and Aleksandr, for all they have sacrificed and done for me. I also thank my little sister, Yulia, for all joy and fun we had together. I would like to thank my farther-in-law, Valeriy, for constant support of my pursuit of academic carrier. I am grateful to my mother-in-law, Olga, for coaching my children in the busy period of my life. The support from the rest of my family has never wavered.

I am deeply grateful to my wife, Natalia, for her love, appreciation, and undying support in our life journey. I have been really blessed to have her beside me. This thesis is dedicated to her. I also would like to thank two little angels, my twin daughters, Alevtina and Polina. You were my support team during long nights when I wrote major part of this work. I believe we will continue to be a friendly team for the rest of my life.

I stand in humble gratitude to all who helped me, taught me and loved me.

TABLE OF CONTENTS

APPENDIX

LIST OF TABLES

LIST OF FIGURES

Figure page

Abstract of Dissertation Presented to the Graduate School
of the University of Florida in Partial Fulfillment of the
Requirements for the Degree of Doctor of Philosophy

COMPACT MUON SOLENOID EXPERIMENT DISCOVERY POTENTIAL FOR SUPERSYMMETRY IN SAME-CHARGE DI-LEPTON EVENTS

By

Yuriy Aleksandrovich Pakhotin

August 2010

Chair: Guenakh Mitselmakher
Cochair: Andrey Korytov
Major: Physics

Same-charge di-lepton events provide a very clean experimental signature for Supersymmetry (SUSY) search. This work studies the Compact Muon Solenoid (CMS) experiment search potential for new physics with same-charge, isolated di-leptons accompanied by jets and large missing transverse energy. The results show that CMS sensitivity for new physics at 7 TeV with integrated luminosity 100 pb^{-1} will exceed current Tevatron limits.

Muon detection for SUSY discovery in the forward direction is accomplished using cathode strip chambers (CSC). These detectors identify muons, provide a fast muon trigger, and give a precise measurement of the muon trajectory. There are 468 six-plane CSCs in the system. The efficiency of finding muon trigger primitives (muon track segments) was studied using 36 CMS CSCs and cosmic ray muons during the Magnet Test and Cosmic Challenge (MTCC) exercise conducted by the CMS experiment in 2006. The efficiency of finding 2-dimensional trigger primitives within 6-layer chambers was found to be $99.93 \pm 0.03\%$.

CHAPTER 1
PREFACE

This dissertation describes a study of the Compact Muon Solenoid (CMS) experiment search potential for new physics in same-charge di-lepton events. The aim of the work was to demonstrate that CMS sensitivity for new physics in this signature with initial data collected at $\sqrt{s}$ = 7 TeV will exceed current experimental limits from LEP and Tevatron.

The author explains steps of the study. Starting with theoretical motivation of the new physics search. Following by the description of the experimental setup. Continuing with details of simulated data analysis. And finishing with explanation of measurement of efficiency to find muon trigger primitives.

Chapter 2 introduces the motivation for search for physics phenomena beyond Standard Model (SM). One of the favorite candidates for new physics is Supersimmetry (SUSY). It is outlined in this Chapter. The simplest SUSY model, Minimal Supergarvity (mSUGRA), is also described in the Chapter 2. Finally, the current bounds from different experimental searches for SUSY are reviewed.

Chapter 3 focuses on a description of the Large Hadron Collider (LHC) and the CMS detector. Major systems of the facilities are reviewed. At the end of the Chapter results obtained during cosmic and first collider runs are outlined.

Chapter 4 is the core of the dissertation. It focuses on an explanation of analysis path and optimization procedure using simulated events with same-charge, isolated di-leptons accompanied by jets and large missing transverse energy. Projected 95%CL exclusion limits and 5σ discovery contours for mSUGRA are reported for 100 pb^{-1} of integrated luminosity at the LHC energies $\sqrt{s}$ = 7 TeV and $\sqrt{s}$ = 10 TeV. It is shown that the CMS can probe SUSY at 7 TeV with initial integrated luminosity 100 pb^{-1} beyond current LEP and Tevatron limits.

For same-charge di-muons study in the CMS Endcap Muon System (EMU) the efficiency of finding muon trigger primitives in the Cathode Strip Chambers (CSC) is measured with cosmic muons. Chapter 5 describes this measurement. The obtained efficiency had exceeded the design specification and was used as a benchmark in later studies.

The work described in this dissertation is done by the author, as a member of the CMS collaboration.

CHAPTER 2
STATUS OF THE FIELD

2.1 Introduction

Understanding of the building blocks of matter has undergone huge development during last 2500 years. Starting at ancient era from Aristotle's five basic elements (earth, water, air, fire, and aether) and Democritus' atomic hypothesis, progressing through Descartes' mechanical description of matter, it came to the conceptions of waves, atoms and molecules by the end of 19th century. During the 20th century, 12 elementary particles and 4 fundamental forces were discovered. Development of quantum mechanics has led to a successful modern theory of particles – Standard Model (SM). A thorough review of theoretical developments and discoveries of elementary particles and fields from a historical perspective is well beyond scope of this work and can be found elsewhere [1–4]. The current status of the field is briefly reviewed in this section.

2.2 Elementary Particles

2.2.1 Leptons

The electron [5] was the first discovered elementary particle. It is negatively electrically charged with magnitude $e = 1.6 \times 10^{-19}$ C which is commonly used as a unit of electric charge[1] . There are two other observed charged particles, muon [6] and tau [7] that have all the same properties as electron except the mass and mean life time. These particles were called leptons. There are three other observed neutral flavors of leptons — neutrinos [8]. Common notation for charged leptons is l, and for neutral — ν. The six currently discovered leptons join into pairs forming three generations. Properties of leptons are summarized in Table 2-1.

Masses and mean life times of electrons, muons and taus are well measured. Neutrino oscillations give compelling evidence that neutrinos are massive [9, 10].

[1] Natural units ($e = m_e = c = \hbar = 1$) are used throughout this work

Table 2-1. Properties of leptons [12].

Generation	Flavor		Charge	Mass	Mean life time
	name	notation	(e)	(MeV/c^2)	(s)
1	electron	e	-1	0.51	$> 4.6 \times 10^{26}$
	electrron neutrino	ν_e	0	$< 2 \times 10^{-6}$	large
2	muon	μ	-1	106	2.2×10^{-6}
	muon neutrino	ν_μ	0	< 0.19	large
3	tau	τ	-1	1777	2.9×10^{-13}
	tau neutrino	ν_τ	0	< 18.2	large

Direct electron neutrino mass measurement is underway [11]. Measured lower levels on mean life times for neutrinos are large and depend on mass ranges and mixing parameters [12]. They are not reported in Table 2-1.

2.2.2 Quarks

After the discovery of atomic nuclei components — protons [13] and neutrons [14], their structural parts (partons) were predicted [15–19] and then observed [20–26]. These particles were called quarks. Common notation for quarks is q. Six currently discovered quarks join into pairs forming three generations. Properties of quarks are summarized in Table 2-2.

Table 2-2. Properties of quarks [12].

Generation	Flavor		Charge	Mass (in the $\overline{MS}$ scheme)
	name	notation	(e)	(MeV/c^2)
1	up	u	$+2/3$	1.5 to 3.0
	down	d	$-1/3$	3 to 7
2	charm	c	$+2/3$	$1.25 \pm 0.09 \times 10^3$
	strange	s	$-1/3$	95 ± 25
3	top	t	$+2/3$	$172.3\ ^{+10.2}_{-7.6} \times 10^3$
	bottom	b	$-1/3$	$4.20 \pm 0.07 \times 10^3$

By convention, quarks have positive parity and antiquarks have negative parity. Quarks have the additive baryon number $1/3$, antiquarks $-1/3$. Due to color confinement (see subsec. 2.3.1 for more details) quarks are never found in isolation and were observed only indirectly within other particles. Particles made of quarks are called hadrons. All quarks carry fractional electrical charge, however, hadrons always have integer electrical charge. Bound quarks q and antiquarks $\bar{q}'$ (the flavors of q and $\bar{q}'$ may be different) form mesons, for example: π, ρ, η, ω, ϕ, J/ψ, K, D, B, Υ, etc. All mesons have baryon number 0. Three bound quarks form baryons, for instance: p, n, Δ, Λ, Σ, Ξ, Ω, etc. All baryons have baryon number 1. Note, that exotic mesons (glueballs [27, 28], tetraquarks [29], hybrids [30], etc) and exotic baryons (pentaquarks [31, 32], H di-baryon [33], supersymmetric R-baryon [34], etc) are predicted in some theories but were not convincingly observed yet [12]. Quark masses are measured indirectly through their influence on the properties of hadrons and are dependent on the particular theoretical framework that is used to define them.

All leptons and quarks are fermions because they have spin $1/2$ and obey Fermi-Dirac statistics. Hence, only one fermion can occupy a quantum state at a given time.

No experimental evidences for leptons and quarks constituents, preons [35], have been found. Therefore, leptons and quarks are currently considered as elementary point-like particles.

A fourth generation of leptons and quarks has been searched for but no evidence has been observed [12]. It has been indirectly shown [36] that no more than three generations (with light neutrino) exist. Only the first generation of leptons and quarks generally are common in the modern universe. Higher generation particles are unstable and decay quickly. To create these particles and to study their properties high energy collisions at particle accelerators are used.

2.2.3 Antiparticles

Each charged particle (lepton or quark) has an oppositely charged twin called antiparticle. Antiparticles were theoretically predicted [37] based on charge conjugation (C) symmetry and then were successfully observed in experiment [38]. Antimatter is not common in the modern universe. Baryogenesis is the process thought to be responsible for the matter-antimatter asymmetry [39]. The model of baryogenesis includes the following three conditions: 1) baryon number violation, 2) charge conjugation and parity (*CP*) symmetry violation and 3) no thermal equilibrium of particle-antiparticle interactions in early universe.

All properties of an antiparticle are identical with a particle, but antiparticles have opposite electrical charge. A charged particle and its antiparticle annihilate emitting photons. Antineutrinos are neutral and it is not certain yet if they are completely identical to neutrinos (Majorana neutrinos) or not (Dirac neutrinos). Note, that only the electron's antiparticle has unique name – positron.

2.3 Fundamental Forces

Elementary particles interact with each other. There are four fundamental forces (strong, electromagnetic, weak, and gravitational) currently known. In modern theory all interactions have carrier particles. The properties of fundamental forces and their carrier particles are summarized in Table 2-3 and reviewed in following four subsections.

Table 2-3. Properties of fundamental forces [12].

Force			Carrier particle			
name	range (m)	strength at $\sim$1 GeV	name	notation	charge (e)	mass (MeV/c^2)
strong	10^{-15}	1	gluon	g	0	0
electromagnetic	∞	$1/137$	photon	γ	0	$< 1 \times 10^{-24}$
weak	10^{-18}	10^{-6}	intermediate vector boson	$W^{\pm}$	± 1	80.4×10^3
				Z^0	0	91.2×10^3
gravity	∞	10^{-39}	graviton	G	0	$< 8 \times 10^{-26}$

All interaction carriers are bosons because they have spin 1 (2 for gravitons) and obey Bose-Einstein statistics. Hence, several bosons can occupy the same quantum state.

The intriguing similarity between lepton and quark sectors can be explained with a hypothetical interaction between them in framework of technicolor theory [40, 41]. No evidence for the interaction between leptons and quarks carried with leptoquark bosons was observed yet. For leptoquark couplings of electromagnetic strength, leptoquarks with masses up to 275-325 GeV are ruled out [42].

2.3.1 Strong interaction

The strong interaction provides the “glue” to hold the quarks together to make hadrons, mesons and baryons. It also holds protons and neutrons (both are baryons) together in atomic nuclei. The strong force is the ”strongest” of the four known fundamental interactions.

Color (strong charge) was introduced as a new quantum number for every quark to resolve observation of the Δ^{++} baryon [43] with spin $1/2$ (an antisymmetric state of three *uuu* quarks). It can have one of three values — red, green or blue. Free quarks have never been observed, therefore it is strongly suggested that only colorless states are allowed as real particles. The carrier of strong color-conserving interaction, a bi-colored massless particle of spin one that carries color information from one quark to another was called a gluon (g). Gluon was indirectly observed in events with three jets at PETRA [44] experiment in DESY. Assuming three colors only 8 bi-colored gluons are allowed. Gluons, being bi-colored objects, have a strong charge, therefore, they interact directly among themselves.

The strong interaction is currently described within framework of Quantum Chromodynamics (QCD), which is a part of the Standard Model (more details in subsection 2.4.1).

2.3.2 Electromagnetic interaction

The electromagnetic interaction provides the force between electrically charged particles. It holds together electrons and nuclei in atoms. It is also responsible for intermolecular forces that form most small-scale bodies except gravitationally formed large-scale astronomical objects.

Two types of electrical charges and forces between them (causing attraction and repulsion) have been known for centuries. Also permanent magnets were common. Both forces, electric and magnetic, were combined together in the framework of classical electromagnetic theory [45, 46]. It was the first successful unification of forces that seem completely different. It was shown that changing an electric field creates a magnetic field and vice versa. This theory naturally predicts a magnetic charge (Dirac monopole) that has not been observed so far [12]. The wave nature of light was explained in framework of the theory and later experimentally confirmed [47]. The theoretical prediction of the constant speed of light broke the Galilean invariance principle of classical mechanics and led to an extension known as the theory of special relativity [48], which is compatible with classical electromagnetism. Observation of the photoelectric effect [49, 50] revealed the quantum nature of light [51]. The carrier of the electromagnetic charge-conserving interaction is an electrically neutral massless particle of spin one, which is called the photon (γ). There is only one type of photon. Photons, being electrically neutral objects, have zero electric charge and do not interact directly among themselves. Photons were experimentally discovered as radiation emitted from radium.

The high-precision quantum perturbation theory of interactions between electrically charged particles by the exchange of photons is called Quantum Electrodynamics (QED). Electromagnetic interactions are currently described within unified Electroweak (EW) theory that is a part of the Standard Model (more details in subsection 2.4.2).

2.3.3 Weak interaction

The weak interaction is responsible for the decay of massive quarks and leptons into lighter quarks and leptons, i.e. flavor changing. Observation of β-decay (a process in which a neutron disappears and is replaced by a proton and emitted electron and electron neutrino) was resolved by introducing a massive charged carrier of the weak interaction, $W^{\pm}$-boson. The unstable charged leptons always decay into their own type of neutrino, emitting a W-boson, therefore, weak interaction conserve lepton number of each type. Any quark can convert to any other quark type (although the probabilities are different by order of magnitude as described by the Cabibbo-Kobayashi-Maskawa or CKM matrix) with a different electric charge by emitting W-boson. Weak decay processes always proceed from a more massive particle to a less massive particle. Scattering processes can involve the reverse transitions, provided sufficient energy is available. This explains why the modern universe mostly consists of leptons and quarks of first generation, i.e. the lightest particles. The W-bosons were observed with UA1 and UA2 experiments at CERN [52, 53].

The weak interaction is currently described within unified Electroweak (EW) theory that is a part of the Standard Model (more details in subsection 2.4.2). The electroweak theory predicted an additional neutral massive carrier of weak interaction, Z^0-boson. It was indirectly observed in neutral current processes [54, 55] and later directly discovered with UA1 and UA2 experiments at CERN [56, 57].

2.3.4 Gravitational interaction

Gravity is the weakest fundamental interaction, but it is the main force to shape large scale structure in the universe. This subsection is the only mention of gravity in this work because it is usually irrelevant at the elementary particle scale.

In the late 17th century Isaac Newton developed a mathematical description of the gravitational force [58] which is proportional to the masses of the interacting objects and depends on the inverse square of the distance between them. A great success of the theory was the derivation of Kepler's three laws of planetary motion, including the elliptical orbits for planets. The modern mathematical notation of the Newton's law is following:

$$F_G = G\frac{m_1 \cdot m_2}{|r_{12}|^3}\hat{\mathbf{r}}_{12},$$

where $G = 6.67428 \times 10^{-11}$ N·kg^2/m^2 is the gravitational constant that was first measured [59] in 1797 by Henry Cavendish. Newton's law of gravity continues to be used as an excellent approximation of the effects of gravity. However, some astronomical observations were not in accord with the predictions of Newton's theory.

In 1915 Albert Einstein developed the general theory of relativity [60]. In the framework of this geometric theory, gravity is a result of space-time being curved by matter and energy and it is described with Einstein's field equations:

$$R_{\mu\nu} - \frac{1}{2}g_{\mu\nu}R + g_{\mu\nu}\Lambda = \frac{8\pi G}{c^4}T_{\mu\nu},$$

where $R_{\mu\nu}$ is the Ricci curvature tensor, $g_{\mu\nu}$ is the metric tensor, R is the scalar curvature, Λ is the cosmological constant, c is the speed of light, and $T_{\mu\nu}$ is the stress-energy tensor. The first success of this theory was Einstein's calculation of perihelion precession of Mercury [61] precisely as astronomically observed. During the 20th century the general relativity was tested and confirmed in several experiments: measurements of deflection of light by the Sun [62], observations of the gravitational redshift of light [63, 64], identifications of gravitationally lensed object (Twin Quasar) [65], tests of light travel time delay [66, 67], tests of the equivalence principle [68, 69], frame-dragging tests [70], and indirect detection of gravitational waves from binary pulsars [71, 72]. Gravitational radiation observatories [73, 74] have been built to directly observe gravitational waves. No detection has been made so far [75].

In 1999 the Supernova Cosmology Project made an observation of the accelerating expansion of the universe [76]. A favorite explanation of this observation is a non-zero cosmological constant $\Lambda \sim 10^{-35}$ s^{-2} in Einstein's field equations, which leads to the hypothesis of dark (or vacuum) energy present in the universe which exerts negative pressure. The most recent measurements [77] implied a value of dark energy density $\Omega_\Lambda = 0.726$ which is the fraction of the total mass-energy density of a flat universe.

During the 20th century a few approaches (string theory, loop quantum gravity, etc) to quantum gravity were developed [78]. However, there is no complete, consistent and experimentally tested theory so far. The graviton, a hypothetical carrier of gravitational interaction appeared naturally in number of those quantum gravity theories. This particle has not been directly observed, but it is expected to have spin 2 and mass zero.

2.4 Standard Model

The Standard Model (SM) is the modern relativistic quantum field theory of fundamental particles and their interactions. This theory includes the strong interaction due to color charges of quarks called Quantum Chromodynamics (QCD) and a combined theory of weak and electromagnetic interaction due to weak and electric charges of quarks and leptons, known as Electroweak (EW) theory. Dynamic of fermions in framework of SM is described by the Dirac Lagrangian

$$\mathcal{L}_D = \bar{\psi}\gamma_\mu(i\partial^\mu)\psi - m\bar{\psi}\psi, \tag{2–1}$$

where ψ is a complex four component spinor of fermion field with mass m. The dynamics of bosons is determined by the Klein-Gordon Lagrangian

$$\mathcal{L}_{KG} = \partial_\mu\phi^*\partial^\mu\phi - M^2\phi^\dagger\phi, \tag{2–2}$$

where ϕ is a complex scalar of boson field with mass M.

The SM have a local symmetry described by gauge groups. Mathematically the SM is a non-Abelian[2] Yang-Mills[3] type gauge field theory based on the group $SU(3)_C \times SU(2)_L \times U(1)_Y$.

2.4.1 Quantum Chromodynamics

The color symmetry group of strong interaction, $SU(3)_C$, is assumed to be unbroken. Hence gluons are massless vector bosons and form an octet of color symmetry.

[2] Non-abelian (non-commutative) group is a group in which the result of applying the group operation to two group elements depends on their order.

[3] YangMills theory is a gauge theory based on $SU(n)$, the special unitary group of the $n \times n$ matrices with determinant 1.

The strong interaction coupling constant varies with respect to momentum transfer, Q^2. It is large at low Q^2 and becomes smaller at high Q^2. The former fact is called asymptotic freedom, and it explains that in very high-energy collisions, quarks and gluons interact very weakly. As a result QCD becomes a perturbative theory at high energies and predicts experimental results with high precision. Since the force between quarks and gluons increases with distance, then it is considered that quarks and gluons can not be found free outside of hadrons. This aspect of QCD is called confinement.

2.4.2 Unified Electroweak Model

The electroweak model is a unification of quantum electrodynamic and weak interactions. Although these two interactions behave differently at currently studied energy range ($\sim 10^2$ GeV), there are strong indications that they merge into one force at very high energy scale ($\sim 10^{15}$ GeV). Predictions of the electroweak model were successfully confirmed in experiments.

The symmetry group of electroweak interaction, $SU(2)_L \times U(1)_Y$, is spontaneously broken to $U(1)_{EM}$ by the Higgs mechanism. This mechanism is the introduction of one extra field with nonzero vacuum expectation value, which means the space is filled with the field and particles interacting with it acquire masses. As a result of this breaking, the carriers of weak force, $W^\pm$ and Z^0 bosons become massive, but the electromagnetic force carrier, the photon, stays massless. One degree of freedom of the newly introduced field manifests itself as a scalar particle called the Higgs boson.

No observation of the Higgs boson has been made so far. It is one of the main goals of currently running high-energy experiments with the Large Hadron Collider (LHC).

2.4.3 Standard Model Lagrangian

The modern mathematical framework of the Standard Model is based on the postulating of symmetries described above and constructing most general renormalizable Lagrangian that conserves these symmetries. The exact formulation of the SM

Lagrangian can be found elsewhere [12]. A graphical representation of SM Lagrangian is shown on Figure 2-1. This figure describes all possible tree-level interactions between particles in framework of SM. Solid lines represents interactions between particles and force carriers. Dashed lines represent not yet observed interaction between massive particles and Higgs particle. Dash-dotted line represent interaction between neutrino and Higgs particle. Former interaction is not included in modern SM but there are strong indications [9, 11] that neutrinos are massive and this interaction is valid. Loop lines for g, H and W represent self interactions, i.e. $3g$, $4g$, $3H$, $4H$ and $4W$ couplings.

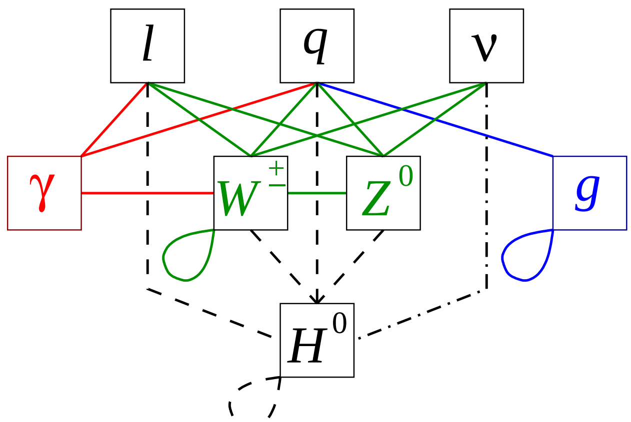

Figure 2-1. Scheme of tree-level interactions in Standard Model.

The SM Lagrangian depends on 19 parameters measured by experiments.

2.5 Supersymmetry

Supersymmetry (SUSY) is a symmetry relating bosonic and fermionic degrees of freedom:

$$|S = 0 \; or \; S = 1\rangle \longleftrightarrow |S = \frac{1}{2}\rangle.$$

Originally proposed as a pure mathematical trick [79–84], the SUSY arose as a possible solution for various Standard Model ”imperfections”.

First, SUSY alleviates ”SM fine-tuning problem” due to reciprocal cancellation of quadratically divergent fermionic and bosonic loops, provided that supersymmetric particles have masses no larger than a few TeV.

Second, there are three quantitative predictions of SUSY that favor it as a great candidate for physics beyond Standard Model. These predictions are following:

- Precision fits to electroweak data shows that the mass of Higgs boson is less than 200 GeV. There are no constraints on the mass of the Higgs particle in the framework of the SM. In contrast, the simplest SUSY model limits the mass of the lightest Higgs particle as no heavier than 140 GeV.
- All three inversed gauge couplings run linearly with ln Q^2. They convincingly meet all together at scale $Q^2 \sim 10^{15}$ in framework of SUSY. This is not the case for running couplings calculated within SM.
- In SUSY models the evolution of the Higgs mass from the GUT scale ($Q^2 = 10^{16}$) to the electroweak scale ($Q^2 = 10^2$) gives a negative value of the correct order of magnitude and is more naturally motivated than within SM.

Detailed explanation of all these arguments in favor of SUSY can be found elsewhere [85–87].

2.5.1 Minimal Supersymmetric Standard Model Extension

The simplest SUSY theory is the Minimal Supersymmetric Standard Model MSSM [88]. In the framework of this model each SM particle acquires one and only one superpartner. Each fermion (quark or lepton) has a superpartner with spin 0 called sfermion. By analogy, each SM interaction carrier boson acquires superpartner of spin $1/2$ called gaugino. Finally, it turns out that one superpartner for the Higgs boson is not enough to make MSSM model complete. There are two Higgs bosons, and correspondingly two Higgs superpartner (called higgsino) doublets were introduced. The SM particles and their MSSM superpartners together with their transformation properties under the SM symmetry groups are summarized in Table 2-4.

After electroweak symmetry breaking is introduced into MSSM, charged winos $\tilde{W}^{\pm}$ and higgsinos $\tilde{H}_u^+$, $\tilde{H}_d^-$ have the same quantum numbers and therefore mix. These mixed states (mass eigenstates of the system) would be physically observed as particles called charginos ($\tilde{\chi}_1^{\pm}$ and $\tilde{\chi}_2^{\pm}$). By convention, mass of $\tilde{\chi}_1^{\pm}$ is considered to be the lightest one out of these two states. Similarly, the neutral zino $\tilde{Z}^0$, bino $\tilde{B}^0$ and higgsinos $\tilde{H}_u^0$, $\tilde{H}_d^0$ are

Table 2-4. Particles and their superpartners within the MSSM framework.

Particle			Gauge transformation			Superparticle		
spin	name	notation	$SU(3)_C$	$SU(2)_L$	$U(1)_Y$	notation	name	spin
1/2	*leptons* (×3 *gen.*)	$L=\begin{pmatrix}\nu_{eL}\\ e_L\end{pmatrix}$	**1**	**2**	-1	$\widetilde{L}=\begin{pmatrix}\widetilde{\nu}_{eL}\\ \widetilde{e}_L\end{pmatrix}$	*sleptons* (×3 *gen.*)	0
		e_R	**1**	**1**	2	$\widetilde{e}_R$		
1/2	*quarks* (×3 *gen.*)	$Q=\begin{pmatrix}u_L\\ d_L\end{pmatrix}$	**3**	**2**	$\frac{1}{3}$	$\widetilde{Q}=\begin{pmatrix}\widetilde{u}_L\\ \widetilde{d}_L\end{pmatrix}$	*squarks* (×3 *gen.*)	0
		u_R	$\mathbf{3}^*$	**1**	$-\frac{4}{3}$	$\widetilde{u}_R$		
		d_R	$\mathbf{3}^*$	**1**	$\frac{2}{3}$	$\widetilde{d}_R$		
1	*gluons*	g	**8**	**1**	0	$\widetilde{g}$	*gluinos*	1/2
	W bosons	$W^{\pm}$	**1**	**3**	0	$\widetilde{W}^{\pm}$	*winos*	
	Z boson	Z^0				$\widetilde{Z}^0$	*zino*	
	B boson	B^0	**1**	**1**	0	$\widetilde{B}^0$	*bino*	
0	*Higgs bosons*	$H_u=\begin{pmatrix}H_u^+\\ H_u^0\end{pmatrix}$	**1**	**2**	1	$\widetilde{H}_u=\begin{pmatrix}\widetilde{H}_u^+\\ \widetilde{H}_u^0\end{pmatrix}$	*Higgsinos*	1/2
		$H_d=\begin{pmatrix}H_d^0\\ H_d^-\end{pmatrix}$	**1**	**2**	-1	$\widetilde{H}_d=\begin{pmatrix}\widetilde{H}_d^0\\ \widetilde{H}_d^-\end{pmatrix}$		

mixed. These mixed states would be physically observed as particles called neutralinos ($\tilde{\chi}_1^0$, $\tilde{\chi}_2^0$, $\tilde{\chi}_3^0$ and $\tilde{\chi}_4^0$). By convention the mass of $\tilde{\chi}_1^0$ is considered to be the lightest one out of these four states.

2.5.2 Minimal Supergravity

If SUSY is exact, superpartners must be degenerate with SM particles. Since superpartners are not observed, SUSY must be broken. There are two favored supersymmetry breaking mechanisms, gravity mediated (supergravity or SUGRA) and gauge mediated (GMSB).

The most popular (due to simplicity) minimal supergravity model [89] called mSUGRA with only one supercharge will be assumed in the rest of this work. Within this model supersymmetry is broken due to gravitational interactions between visible and hidden sectors. The superpartner of the graviton, called a gravitino, is heavy and interacts with other particles only gravitationally, i.e. extremely weakly. Therefore, gravity introduced into this model breaks supersymmetry but plays no other role in any calculations or predictions.

2.5.3 R-Parity

The MSSM Lagrangian conserves the discrete quantum number

$$R = (-1)^{L+3B+2S}, \tag{2–3}$$

where L is lepton number, B is baryon number and S is spin. This number is called R-parity. It is conventionally constructed in such a way that all SM particles have $R = +1$ but their superpartners have $R = -1$. If R-parity is exactly conserved then there are important consequences: the sparticles are always produced in pairs, and the lightest SUSY particle (LSP) is stable.

A stable neutral LSP leads to an expectation of missing energy in high-energy collisions due to the LSP escaping detection. This property is widely used in searches for SUSY events.

2.5.4 Search for SUSY with Same-charge Di-lepton Events

Supersymmetry may be discovered at hadron colliders by searching for events with two isolated leptons. In the case of gluino production, the most distinguishing feature is that in half the events the two leading isolated leptons are expected to have the same sign. This feature allows to distinguish SUSY signal out of SM background. Same-charge di-lepton signature was originally discussed in [90] and then further developed in [91–96].

A few experimental searches for SUSY with the same-charge di-lepton events have been done at CDF and D0 experiments at Tevatron collider [97–101]. No excess of events over SM background was observed in all these works.

Potential to discover supersymmetry in events with same-carge di-leptons, jets and missing energy with the CMS detector at LHC in pp collisions at $\sqrt{s} = 14$ TeV was studied using Monte Carlo technique in a few papers [102–104]. It was demonstrated

Table 2-5. Mass lower limits for sleptons at 95% C.L.

slepton		mass lower limit (GeV)
selectron	$(\tilde{e}_R)$	99.9
smuon	$(\tilde{\mu}_R)$	94.9
stau	$(\tilde{\tau}_R)$	86.6

that low mass SUSY can be observed up to mass scales of $\sim$ 1.5 TeV/c^2, including systematic effects given 10 fb^{-1} of data collected at $\sqrt{s}$ = 14 TeV.

2.5.5 Current Experimental Limits for Minimal Supergravity

High energy experiments have been searching for SUSY since the beginning of the 1980s. In this subsection we review various searches for SUSY in previous collider experiments. A more thorough review can be found in [12, 86].

2.5.5.1 Direct Search at LEP2

The CERN Large Electron Positron collider (LEP) was upgraded at 1995 after 6 years of running at energy $\sqrt{s} \simeq$ 91 GeV. Four LEP experiments (ALEPH [105], DELPHI [106], L3 [107] and OPAL [108]) collected data with the upgraded collider (LEP2) at energies ranging between $\sqrt{s} \simeq 183 - 208$ GeV.

All four LEP experiments have searched for charged sleptons ($\tilde{l}_R$) in the data taken at LEP2 [109–112]. The L-sleptons were assumed to be beyond the reach of the experiments because, in general, the cross section for R-sleptons is smaller than for L-sleptons. Charged sleptons were searched assuming following decay $\tilde{l} \rightarrow l\tilde{\chi}_1^0$, where the neutralino ($\tilde{\chi}_1^0$) is the LSP and escapes detection. Constraints have been derived in the context of the MSSM. The combination of the experiments shows no evidence for an excess of candidates compared to the estimated background. The expected and observed exclusion curves at 95% Confidence Level (C.L.) in the (slepton mass, neutralino mass) plane is shown in Figure 2-2 (left). Lower limits for slepton masses are summarized in Table 2-5. The limit on $m_{\tilde{e}_R}$ is broadest because the cross section for selectron pair production at LEP2 was greater than the cross sections for smuon or stau pairs production.

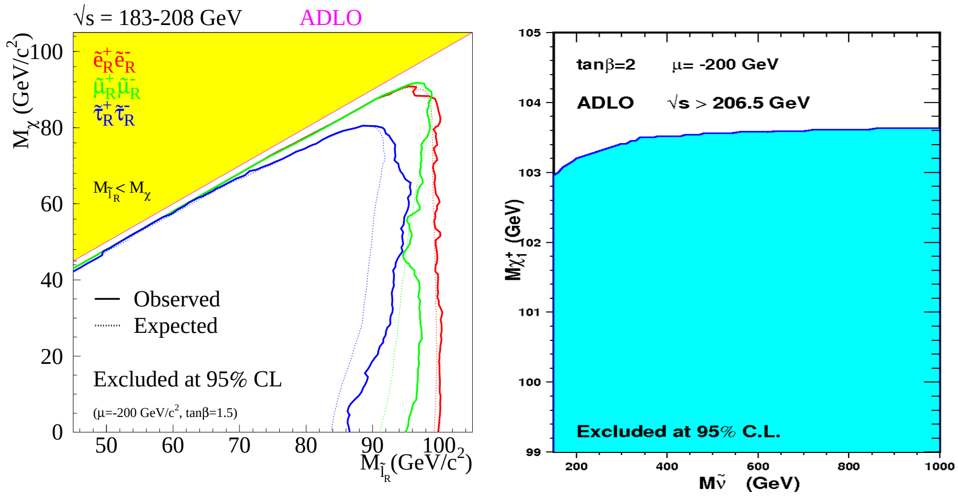

Figure 2-2. Exclusion limits (at 95% C.L.) on sparticle masses from the non-observation of any signal excess over background in LEP2 experiments. Left: Mass lower limit for sleptons ($m_{\tilde{l}_R}$). Right: Mass lower limit for charginos (χ^0_1).

All four LEP experiments analyzed the chargino (χ^+_1) decays into leptons, leptons plus jets, and jets [113]. The results from these channels were then combined. Cross sections and branching ratios have been calculated in the framework of the MSSM. The combination of the experiments shows no evidence for an excess of candidates compared to the estimated background. Obtained exclusion limits (at 95% C.L.) in the (sneutrino mass, chargino mass) plane is shown in 2-2 (right) for the combination of the 208 GeV data. The average lower bound on chargino mass is 103.5 GeV.

2.5.5.2 Direct Search at Tevatron

The FermiLab Tevatron collider was completed in 1983 and then upgraded in 1999. Two Tevatron experiments (CDF [114–116] and D∅ [117–119]) collected data with upgraded collider at center of mass energy $\sqrt{s}$ = 1.96 TeV.

Both Tevatron experiments are searching for squark-gluino production [120, 121]. Analyzed data shows no evidence for an excess of candidates compared to the estimated background. Obtained exclusion limits (at 95% C.L.) in the m_0-$m_{1/2}$ and $m_{\tilde{q}}$-$m_{\tilde{g}}$ planes are shown in Figure 2-3 for D∅ and in Figure 2-4 for CDF experiments.

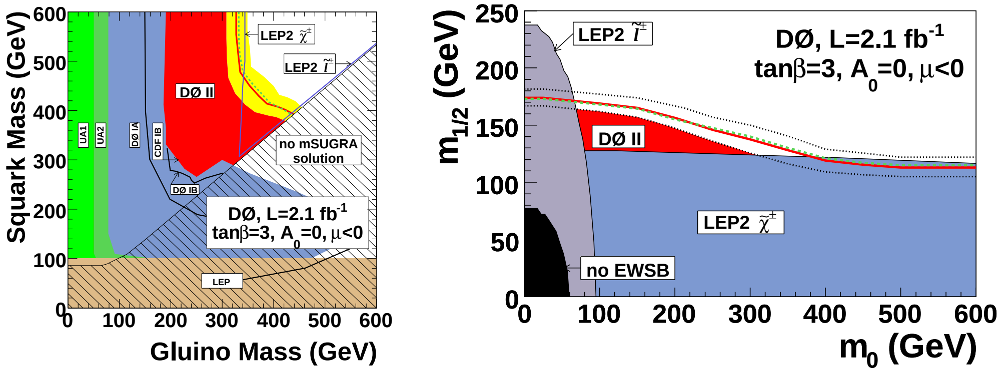

Figure 2-3. The red regions show the areas (left: in squark and gluino masses plane; right: in m_0-$m_{1/2}$ plane) excluded (at 95% C.L.) by D∅ experiment at Tevatron with 2.1 fb^{-1} of data from the non-observation of any signal excess over background in the framework of mSUGRA assuming R-parity conservation [120]. Exclusions by other experiments are also shown for comparison.

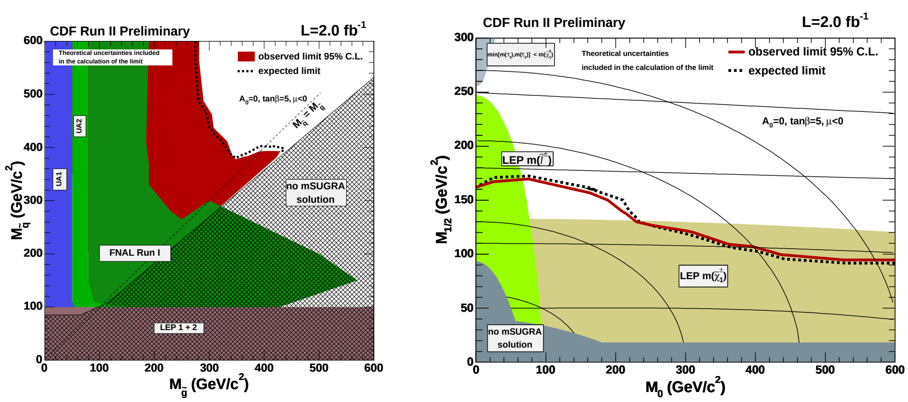

Figure 2-4. The red regions show the areas (left: in squark and gluino masses plane; right: in m_0-$m_{1/2}$ plane) excluded (at 95% C.L.) by CDF experiment at Tevatron with 2.0 fb^{-1} of data from the non-observation of any signal excess over background in the framework of mSUGRA assuming R-parity conservation [121]. Exclusions by other experiments are also shown for comparison.

Also both Tevatron experiments are searching for chargino-neutralino production in the trilepton signature [122–124]. Analyzed data shows no evidence for an excess of candidates compared to the estimated background. Obtained exclusion limits (at 95% C.L.) in the m_0-$m_{1/2}$ plane are shown in Figure 2-5 (left – CDF, right – D0).

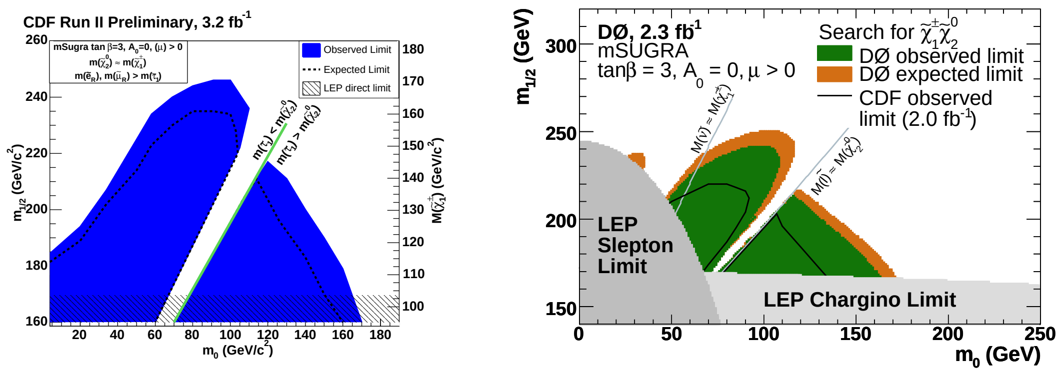

Figure 2-5. The blue regions on left plot show the areas (in m_0-$m_{1/2}$ plane) excluded (at 95% C.L.) by CDF experiment with 3.2 fb^{-1} of data from the non-observation of any tri-lepton signal excess over background in the framework of mSUGRA assuming R-parity conservation [123]. The green regions on right plot show the areas (in m_0-$m_{1/2}$ plane) excluded (at 95% C.L.) by D∅ experiment with 2.3 fb^{-1} of data from the non-observation of any tri-lepton signal excess over background in the framework of mSUGRA with R-parity conservation [124].

CHAPTER 3
STATUS OF THE EXPERIMENT

3.1 Introduction

There are two main approaches in experimental High Energy Physics: collider and non-collider. The ”standard” collider experiment includes two parts: the accelerator to produce, speed up and collide particles and the detector to observe what comes out of the particle interactions. A thorough review of accelerator physics, modern collider parameters and detector instruments and methods is available in [12].

The experimental setup for prospective SUSY search, as described in Chapter 4, is a collider experiment and consists of an accelerator – Large Hadron Collider (LHC) [125, 126] and a detector – Compact Muon Solenoid (CMS) [127, 128]. The measurement of efficiency of finding muon track trigger primitives in CMS Cathode Strip Chambers, as described in Chapter 5, has been done with cosmic rays detected by the CMS Muon Endcap System and therefore was a non-collider experiment.

A general review of non-collider instruments and methods (e.g. cosmic ray experiments, neutrino oscillation measurements, searches for double-beta decay, dark matter candidates, magnetic monopoles, etc.) is well beyond the scope of this work and can be found elsewhere [12].

3.2 The Large Hadron Collider

3.2.1 Physics Requirements

The Standard Model (SM) of particle physics has been tested with high precision during the past few decades. Yet it is considered to be an effective theory only up to roughly 1 TeV. Also experimental confirmation of the electroweak symmetry breaking (Higgs) mechanism at an energy scale below 1 TeV is still required to be found for the mathematical consistency of the SM.

There are several alternative models (supersymmetry, extra dimensions, etc.) beyond SM that may describe nature. Most of them predict new particles or phenomena at an energy of about 1 TeV. Hence there are many compelling reasons to investigate the 1 TeV energy scale.

Hadron colliders are well suited for the task of exploring new energy domains. Collisions of protons and anti-protons accelerated to an energy of about 1 TeV are successfully being used at the Tevatron at FNAL (Batavia, Illinois). Note that collisions take place between constituent particles (quarks and gluons) within the proton or antiproton. Only a fraction of the full proton or antiproton energy is carried by partons. Therefore, the energy region of only a few hundred GeV was studied with the Tevatron. The main results obtained at the Tevatron are discoveries of t-quark ($m_t \approx 175$ TeV), Ξ_b^-, Ω_b^-, Σ_b^- baryons, and observation of B_s oscillations.

The Large Hadron Collider (LHC), a proton proton collider with beam energy up to 7 TeV was proposed and approved in 1994 to be built at CERN (Geneva, Switzerland). The LHC is expected to provide a seven-fold increase in energy and a hundred-fold increase in integrated luminosity over the Tevatron collider experiments. It starts to operate in 2009 with reduced beam energy due to safety reasons. The primary goal of the LHC is to study the nature of electroweak symmetry breaking (Higgs mechanism). Another aim of the LHC is to search for evidence of physics phenomena beyond SM at the 1 TeV energy scale.

The LHC will also operate in Heavy Ion mode, with a design luminosity of $L = 10^{27}$ cm^{-2}s^{-1} and center-of-mass energy of 1312 TeV, that is 30 times higher than at the present day accelerators. It enables us to further extend the range of the heavy-ion physics program to include studies of hot nuclear matter. The heavy ion program will also seek for quark-gluon plasma production — a state of matter in which quarks and gluons behave like free particles, and which is believed to have existed at the very early times of the Universe.

3.2.2 Machine Layout

The LHC is a proton-proton accelerator and collider constructed at CERN near Geneva on the border of Switzerland and France as shown on map in Figure 3-1 (left). The LHC is installed in the existing 26.7 km tunnel that was constructed for the CERN LEP machine. The tunnel lies between 45 m and 170 m below the surface on a plane inclined at 1.41% sloping towards lake Leman with respect to the horizontal, thus giving height differences of up to 120 m across the tunnel diameter. The tunnel geometry was originally designed for the electron-positron machine, and there were eight crossing points flanked by long straight sections for RF cavities that compensated for the high synchrotron radiation losses. The LHC being a proton machine does not have the same synchrotron radiation rate and would ideally have longer arcs and shorter straight sections for the same circumference. But reusing the LEP tunnel and its injection chain was a cost saving solution that strongly influenced the decision to build the LHC at CERN.

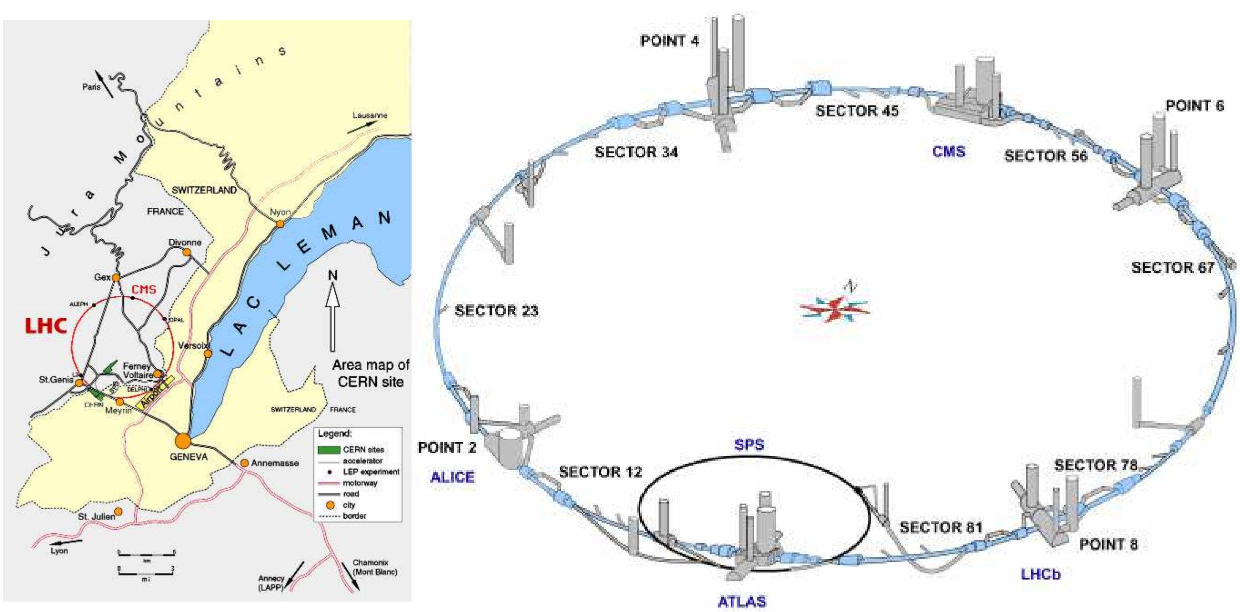

Figure 3-1. The LHC geographical location on map (left) and tunnel scheme (right).

It was decided to use only four of the possible eight interaction regions and to suppress beam crossing in the other four to prevent unnecessary disruption of the beams. Four experiments (ATLAS, CMS, ALICE and LHCb) are located in the interaction areas. The underground and surface structures at Points 1 and 5 were newly constructed for ATLAS and CMS, respectively, while those for ALICE and LHCb, at Points 2 and 8, respectively, were originally built for LEP.

The number of events per second generated in the LHC collisions is given by:

$$N_{events} = L \cdot \sigma$$

where σ is the cross section for the events under study and L is the machine luminosity. The machine luminosity is one of the main characteristics of the collider and it depends only on the beam parameters and can be written for a Gaussian beam distribution as:

$$L = \frac{N_b^2 n_b f_{rev} \gamma_r}{4\pi \epsilon_n \beta} F$$

where N_b is the number of particles per bunch, n_b is the number of bunches per beam, f_{rev} is the revolution frequency, γ_r is the relativistic gamma factor, ϵ_n is the normalized transverse beam emittance, β is the beta function at the collision point, and F is the geometric luminosity reduction factor due to the crossing angle at the interaction point. The exploration of rare events in the LHC collisions therefore requires both high beam energies and high beam intensities.

The maximum LHC beam intensity is limited to $N_b = 1.15 \times 10^{11}$ due to the mechanical aperture of the LHC and the nonlinear beam-beam interaction that each particle experiences when the bunches of both beams collide with each other.

The maximum LHC beam energy that can be reached is limited by the peak dipole field in the storage ring. The maximum nominal filed is 8.33 T, corresponding to an energy of 7 TeV.

The luminosity in the LHC is not constant over a physics run, but decays due to the degradation of intensities and emittances of the circulating beams. The main cause of the luminosity decay during nominal LHC operation is the beam loss from collisions.

Other contributions to beam losses come from Touscheck[1] effect, intra-beam[2] scattering, the nonlinear force of the beam-beam interaction, scattering of particles on residual gas, and radio frequency (RF) noise. The net estimate of the LHC luminosity lifetime is τ_L = 14.9 h.

The minimum LHC injection time is 16 minutes. The average time required for ramping the beam energy in the LHC from injection energy (450 GeV) to collision energy (currently 3.5 TeV, ultimately 7 TeV) is approximately 20 minutes. After a beam abort it takes approximately 20 minutes to ramp the magnets down. The average time to check all systems is 10 minutes. Hence, the minimum turnaround time for the LHC is of the order of 70 minutes. The practical experience of other experiments implies that average turnaround time will be $\sim$ 6 times longer, i.e. $\sim$ 7 hours.

Integrating the luminosity over one physics run gives,

$$L_{int} = \int_0^{T_{run}} L(t)dt = L_0\tau_L\left(1 - e^{T_{run}/\tau_L}\right)$$

where T_{run} is the total length of the run, L_0 is initial peak luminosity. Assuming the luminosity lifetime of 15 hours and average turnaround time of 7 hours, the optimum run time is 12 hours. Assuming peak luminosity $L_0 = 10^{32}$ cm^{-2}s^{-1} and continuous machine operation with 3.5 TeV beam energy during 2010-2011, the net integrated luminosity[3] of $L_{int} \approx 1$ fb^{-1} is expected to be delivered. The ultimate goal of the LHC is $L_{int} \approx 100$ fb^{-1}

[1] The Touschek effect is a single scattering effect which leads to the immediate loss of the colliding particles due to transformation of a small transverse momentum into a large longitudinal momentum.

[2] The intra-beam effect is a multiple scattering which leads to diffusion in all three directions and changes the beam dimensions.

[3] Common unit of integrated luminosity is inverse barn (symbol b^{-1}). Barn is a unit of area defined as 10^{-24} cm^2. Note that 1 fb^{-1} = 10^{39} cm^{-2}.

of integrated luminosity delivered per year with 7 TeV beam energy assuming 200 operation days per year and peak luminosity $L_0 = 10^{34}\ \mathrm{cm}^{-2}\mathrm{s}^{-1}$.

3.2.3 Magnetic and Cryogenic Systems

The tunnel in the LHC arcs has an internal diameter of 3.7 m as shown in Figure 3-2 (left). This makes it extremely difficult to install two separate proton rings in the tunnel. The hard limit on space led to the adoption of the ”two-in-one” (or ”twin-bore”) superconducting dipole magnets that consist of two sets of coils and beam channels within the same mechanical structure and cryostat with magnetic flux circulating in the opposite directions through the two channels. The disadvantage of the twin-bore design is that the rings are mechanically and magnetically coupled, which affects flexibility. The transverse cross-section of the LHC cryodipole is shown in Figure 3-2 (right).

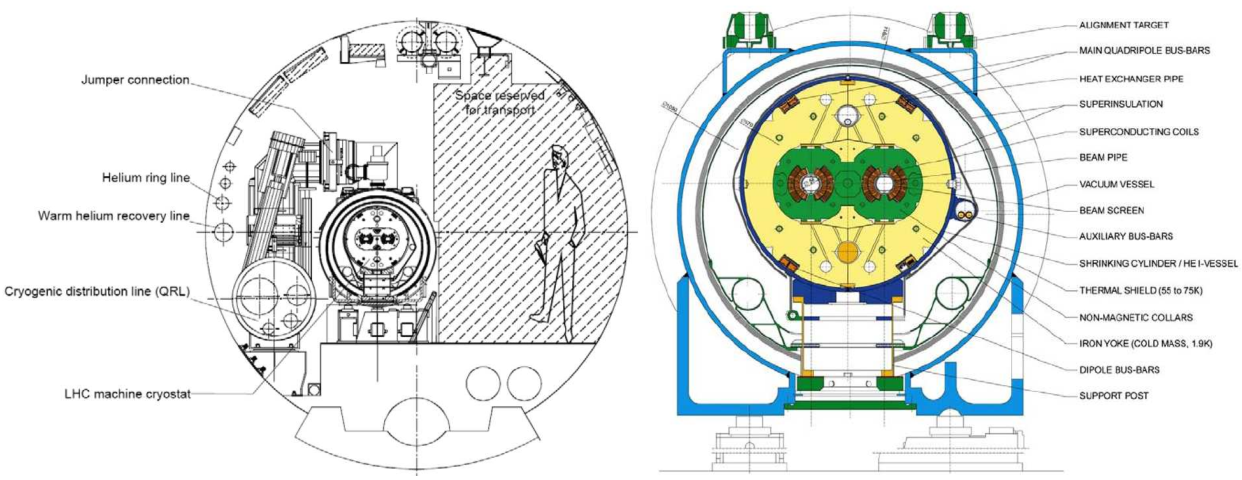

Figure 3-2. Transverse cross-sections of the LHC tunnel (left) and cryodipole (right).

The LHC ring accommodates 1232 main dipoles: 1104 in the arc and 128 in the dispersion suppression regions. They all have the same basic design. A dipole cold mass has an overall length of about 16.5 m, a diameter of 570 mm (at room temperature), and a mass of about 27.5 ton. The cold mass is curved in the horizontal plane with an apical angle of 5.1 mrad, corresponding to a radius of curvature of about

2812 m at 293 K, so as to closely match the trajectory of the particles. The nominal distance between beams in the LHC dipole magnets is 194 mm.

The LHC magnet system also includes single and twin aperture corrector magnets, insertion magnets (four dedicated to experiments, one for RF, two for beam cleaning and one for beam dumping), dispersion suppressor magnets, matching section quadrupole and separation dipole magnets, low-beta triplet magnets and compensator dipoles in the ALICE and LHCb experiments.

Other large superconducting accelerators (Tevatron (at FNAL), HERA (at DESY) and RHIC (at BNL)) all use classical NbTi superconductors, cooled by supercritical helium at temperatures slightly above 4.2 K, with fields below or around 5 T. The LHC magnet system, while still making use of the well-proven technology based on NbTi Rutherford cables, cools the magnets to a temperature below 1.9 K, using pressurized superfluid helium at about 0.13 MPa, and operates at fields above 8 T.

The LHC cryogenic system is separated into eight sectors between access points shown in Figure 3-1 (right). The cryogenic system has five "cryogenic islands" at access Points 1, 2, 4, 6 and 8, where all refrigeration and ancillary equipment is concentrated. Equipment at ground level includes electrical substations, warm compressors, cryogenic storage (helium and liquid nitrogen), cooling towers, and cold boxes. Underground equipment includes lower cold boxes, 1.8 K refrigeration unit boxes, interconnecting lines, and interconnection boxes. Each cryogenic island houses one or two refrigeration plants that feed one or two adjacent tunnel sectors, requiring distribution and recovery of the cooling fluids over distances of 3.3 km underground. The total amount of required superfluid helium is 96 ton. For a normal cool down of a sector, the 600 kW pre-cooler will use a maximum of 1260 ton of liquid nitrogen.

3.2.4 Vacuum System

The LHC has three vacuum systems: the insulation vacuum for cryomagnets, the insulation vacuum for helium distribution, and the beam vacuum. The insulation vacua before cool-down do not have to be better than 10^{-1} mbar, but at cryogenic temperatures, in the absence of any significant leak, the pressure will stabilize around 10^{-6} mbar. The requirements for the beam vacuum are much more stringent, driven by the required beam lifetime and background at the experiments. Equivalent hydrogen gas densities[4] should remain below 10^{15} H_2 m^{-3} to ensure the required 100 hours beam lifetime. In the interaction regions around the experiments, the densities will be below 10^{13} H_2 m^{-3} to minimize the background to the experiments. In the room temperature parts of the beam vacuum system, the pressure should be in the range 10^{10} to 10^{11} mbar.

All three vacuum systems are subdivided into manageable sectors by vacuum barriers for the insulation vacuum and sector valves for the beam vacuum. Sector lengths are 428 m for the helium distribution system and 214 m for the magnet insulation vacuum. The beam vacuum is divided into sectors of various lengths, in most cases the distance between two stand-alone cryomagnets. However, there are no sector valves in the cold arc, leading to a length for this single sector of approximately 3 km.

3.2.5 Beam Injection

The LHC is supplied with protons from the injector chain Duoplasmatron — RF quadrupoles — Linac2 — Proton Synchrotron Booster (PSB) — Proton Synchrotron (PS) — Super Proton Synchrotron (SPS), as shown in Figure 3-3.

Hydrogen gas is fed into a duoplasmatron cathode chamber with electrons. In the chamber the hydrogen atoms dissociate and form a H^+ plasma confined within the magnetic field. The plasma is constricted by a canal and extracted through the anode into an expansion chamber where a proton beam of 300 mA intensity is formed. The

[4] The requirements at cryogenic temperature are expressed as gas densities normalized to hydrogen, taking into account the ionization cross sections for each gas species.

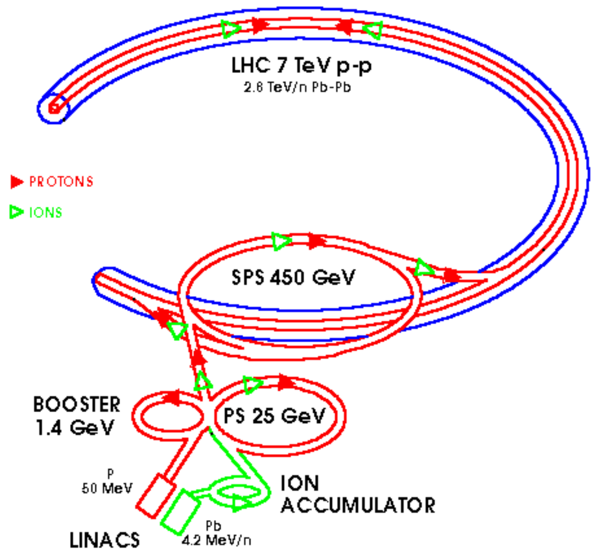

Figure 3-3. Schematic representation of the LHC injector chain (dimensions not proportional to machines real size).

LHC duoplasmatron operates at 92 keV. Then protons enter the RF quadrupole that provides transverse focusing of the beam and accelerates it to energy of 750 keV.

The next stage is a multi-chamber resonant RF cavity accelerator called Linac2. It accelerates a beam of current 180 mA up to 50 MeV. It also shapes the proton beam into short pulses of 30 μs length and low transverse emittance of 1.2 μm.

The Proton Synchrotron Booster (PSB) follows proton beam acceleration. The beam line to the PSB from the Linac is 80 m long, and 20 quadrupole magnets focus the beam along the line. The PSB boosts the protons up to 1.4 GeV and injects them into the Proton Synchrotron (PS). The PS has been upgraded for 40 and 80 MHz of RF operation for the LHC and allows to accelerate protons up to 28 GeV. The PS is also responsible for providing the 25 ns bunch separation for the LHC.

Converted for operation with the LHC, the SPS boosts protons up to 450 GeV for the LHC injection. Note that SPS was the injector for the LEP system, and the injection system was upgraded as well as the RF systems. SPS is fully LHC dedicated during fills (1-2 times per day). Also it serves for other experiments as a source of protons.

The LHC has two injection insertions at Points 2 and 8, each approximately 2.5 km in length, linking the LHC to the CERN accelerator complex.

3.2.6 The RF Systems

The injected beam will be captured, accelerated and stored using a 400.8 MHz superconducting cavity RF system. Transverse injection errors will be damped by a separate system of electrostatic deflectors. All RF and beam feedback systems are concentrated at Point 4 and extend into the tunnel on either side. Separate cavities are used for each beam. Consequently, the beam separation is increased in the RF region to 420 mm (from standard 194 mm) by means of special superconducting dipoles. With the increased separation and also by staggering the cavities longitudinally, the ”second” beam passes outside the cavity.

The minimum required voltage at 450 GeV (injection stage) is 8 MV/beam, and the maximum voltage at 7 TeV is 16 MV/beam. During acceleration the real power supplied to the beams is 275 kW/beam and the energy gain is 485 keV/turn. Note, that synchrotron radiation loss at 7 TeV beam energy is 7 keV/turn. A maximum of 4800 kW of RF power will be generated by sixteen 300 kW 400.8 MHz klystrons. The average waveguide length will be about 22 m.

3.2.7 Beam Dumping

A total beam current of 0.584 A corresponds to a stored energy of approximately 362 MJ. In addition to the energy stored in the circulating beams, the LHC magnet system has a stored electromagnetic energy of approximately 600 MJ, yielding a total stored energy of more than 1 GJ. This stored energy must be absorbed safely at the end of each run or in the case of a malfunction or an emergency.

The dedicated beam dumping system of the LHC is located at Point 6. The system is able to quickly extract the beam from each ring without losses, to an external absorber positioned sufficiently far away to allow for beam dilution, so as not to overheat the absorber material. The beam dumping system also is able to handle beams that are outside normal parameters, due to equipment failure or abnormal optics settings in the rings.

Assuming 200 days per year of LHC operation during 20 years of lifetime and assuming two beams (at nominal current) dumped per day the number of dumps at full intensity per beam in LHC operational lifetime is expected to be 2×10^4. A fault in the beam dump system could lead to severe damage to the system itself, to the LHC machine, and/or to the LHC experiments, due to uncontrolled beam losses on equipment. It is desired that total beam dump failures will not exceed a rate of 1 failure in 10^6 hours, or roughly one failure in 100 years.

The main part of the beam dumping system has two sets of 15 fast-pulsed extraction magnets. At least 14 out of the 15 kicker magnets must operate simultaneously on request. The service life of the magnets will be at least 20 years, and during this period the magnets will be exposed to an estimated integrated radiation dose of 10^6 Gy (10^8 rad).

For each ring, the extracted and diluted beam will be directed onto an external beam dump. The external beam dump is designed for 2×10^4 beam aborts at 7 TeV with full beam intensity during an operational lifetime of 20 years. Carbon was chosen as the most suitable absorbing material for the dumps, with the highest melting (sublimation) temperature and the best thermal shock resistance of the investigated materials. The dump core is a segmented carbon cylinder of 700 mm diameter and 7700 mm length, shrink-fitted in a stainless steel jacket. The jacket incorporates welded tubes for cooling water. Each dump is surrounded by 900 tons of radiation shielding blocks constructed from decommissioned ISR dipole-yokes, partially filled with concrete. Each block is $1298 \times 1088 \times 2440$ mm^3 and weighs 24 tons. Thirty-five blocks in total are required per dump. Activation in the surrounding air, rock, and ground water, and dose-rates close to the core and in different parts of the dump, have been estimated. For general access to the dump-caverns with all the dump-shielding in position, total dose-rates from all sources will be at relatively low levels. Only 1 hour after dumping the beam, the dose-rates will be typically below 300 mSv/h. However, most of this will be due to the ^{24}Na in the concrete shielding and walls, so allowing several days for this to decay would be preferable. The dismantling of the dump to exchange the core requires strict control and remote handling.

3.2.8 Power and Energy Consumption

Total average power of LHC when it is up and running is estimated to be 180 MW including power of cryogenic system (27.5 MW) and detectors (22 MW) [129]. Assuming continuous round-the-clock running of LHC, it is expected to consume 130 GWh of energy per month. Following most recent schedule [130], the LHC after start up will run continuously for 18-24 months hence the energy consumption is estimated to be 1.6 TWh per year. For comparison, the total electric energy consumption of the city of Gainesville (Florida, US) is 5.4 TWh per year [131] which is 3 times more than LHC consumption. Based on current average electricity price (3 c/kWh) the one year of LHC running would result in 50M dollars of electric bill.

3.3 The Compact Muon Solenoid Detector

3.3.1 General Description

The Compact Muon Solenoid (CMS) experiment is one of four detectors built at crossing sites of the LHC beams, and is one of two general purpose detectors (the other is the ATLAS detector) which have been designed to exploit the physics opportunities presented by the LHC. The CMS is located at Point 5 as shown in Figure 3-1 (right).

There are the following requirements for the CMS physics program:

- Good muon identification and momentum resolution over a wide range of momenta and angles, good di-muon mass resolution ($\sim$ 1% at 100 GeV), and the ability to determine unambiguously the charge of muons with momentum less than 1 TeV;

- Good charged-particle momentum resolution and reconstruction efficiency in the inner tracker. Efficient triggering and offline tagging of b-jets, requiring pixel detectors close to the interaction region;

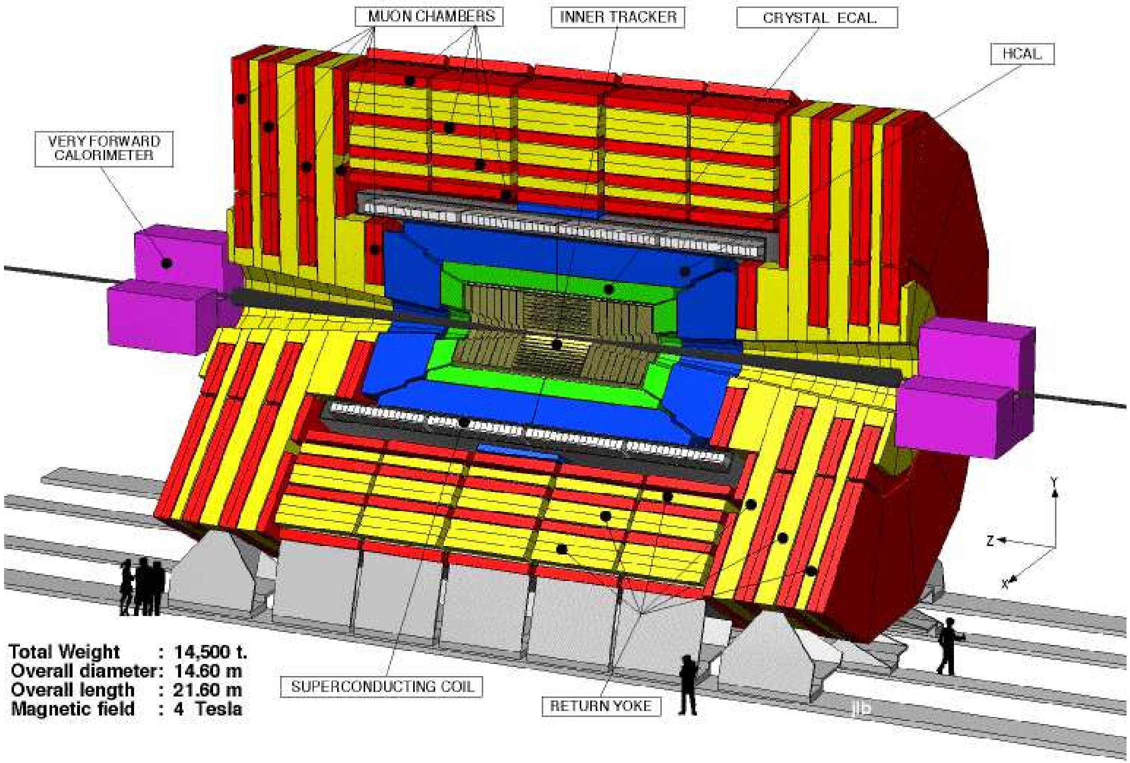

Figure 3-4. A perspective view of the CMS detector.

- Good electromagnetic energy resolution, good di-photon and di-electron mass resolution ($\sim$ 1% at 100 GeV), wide geometric coverage, π^0 rejection, and efficient photon and lepton isolation at high luminosities;
- Good missing transverse energy and di-jet mass resolution, requiring hadron calorimeters with a large hermetic geometric coverage and with fine lateral segmentation;
- Fast electronics of Trigger and Data Acquisition System in order to select and record only meaningful events from a net rate of 40 MHz due to beam spacing of 25 ns. Additionally, there are approximately 25 interactions which occur within each beam crossing.

The CMS detector is built in a traditional symmetrical barrel design with two endcaps to provide nearly 4π coverage. The modular design of the detector is shown in Fig 3-4 and it includes following systems:

- Superconducting solenoid and iron yoke
- Inner tracking system: pixel and tracker silicon detectors

- Electromagnetic calorimeter
- Hadron calorimeter (including very forward calorimeter)
- Muon detectors

Propagations of particles of different sorts are shown in Figure 3-5. All systems of the CMS detector are briefly reviewed in the following subsections. A detailed description of the CMS design can be found elsewhere [127, 128].

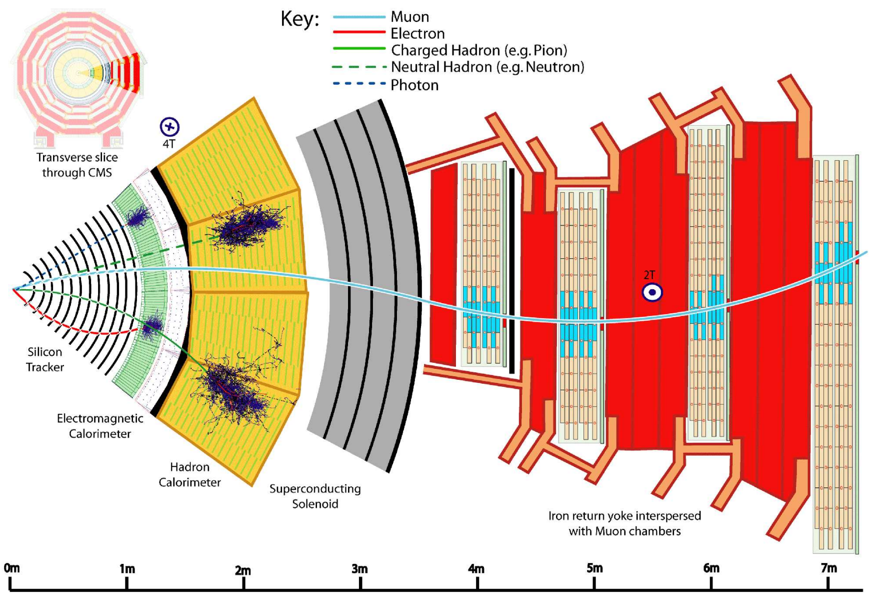

Figure 3-5. Propagation of different particles through the CMS detector.

3.3.2 Coordinate System

The CMS detector lies on the North side of the LHC ring. The x-axis ($\phi = 0°$) points toward the center of the ring (South), while the y-axis is vertical and the z-axis points West to complete the right-handed coordinate system. Therefore, the West (Jura direction) endcap is at $+z$ and $+\eta$ (rapidity), while the East (Saleve direction) endcap is at $-z$ and $-\eta$, as shown in Figure 3-6.

As viewed from the interaction point (IP), azimuthal angle ϕ increases in the conventional way, i.e. clockwise for the $+z$ endcap and counterclockwise for the $-z$ endcap.

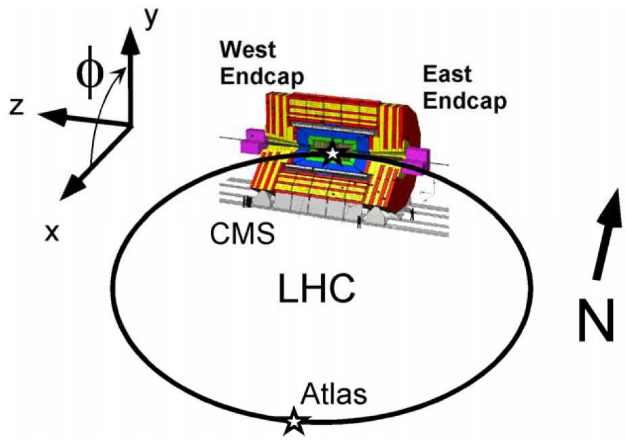

Figure 3-6. Overall CMS coordinate system.

3.3.3 Superconducting Magnet System and Iron Yoke

The superconducting magnet for the CMS detector has been designed to reach a 4 Tesla field in a free bore of 6 m diameter and 12.5 m length with a stored energy of 2.6 GJ at full current. The CMS magnet has a record breaking energy-over-mass ratio $E/M = 11.6$ kJ/kg. The NbTi superconductor is used with critical temperature $T_c = 9.25$ K at zero field and $T_c = 7.30$ K at $B = 4.6$ T (peak field). The operational temperature is 4.6 K.

The CMS solenoid, powered with a 520 kW supply covering a range of voltages from +26 V to -23 V has a nominal operating DC current of 19.143 kA. Inductance of the CMS solenoid is 14.7 H at zero current and then decreases to 13.3 H at 18 kA. The resistance of the CMS solenoid joints ranging from 0.7 nΩ to 1.6 nΩ at 19.1 kA corresponds to a maximum dissipation of 0.6 W. In case of a superconductive-to-resistive transition (quench) the fast discharge (FD) is automatically triggered with a time constant is about 200 s. The FD is performed on a 30 mΩ dump resistor (located outdoors) to keep the dump voltage lower than 600 V, and to limit the coil warm-up and subsequent cool-down time. In case of a power supply fault the slow discharge (SD) is automatically triggered but the coil stays in the superconducting state. The SD time constant is about 7000 s.

The magnetic flux is returned through a 10 kiloton iron yoke comprising 5 wheels and 2 endcaps, composed of three disks each (Fig 3-4). The CMS detector has a modular design and can be reassembled. The elements of the CMS can be moved by a strand jacking hydraulic system that ensures safe operation on the 1.23% inclined floor of the cavern. The maximum movements possible in the cavern are $\sim$ 11 m.

To easily align the yoke elements, a precise reference system of about 70 points was installed in the surface assembly hall. All the elements are pre-positioned within a $\pm$5 mm tolerance and then aligned with an accuracy of 2 mm with respect to the ideal axis of the coil.

3.3.4 Inner Tracking System

The inner tracking system (or tracker) of the CMS is designed to provide a precise and efficient measurement of the trajectories of charged particles made at the LHC collisions, as well as a precise reconstruction of secondary vertices. It surrounds the interaction point and has a length of 5.8 m and a diameter of 2.5 m. The full volume of the CMS tracker is located inside a strong homogeneous magnetic field of 4 T made by CMS solenoid. At the LHC design luminosity of 10^{34} cm^{-2}s^{-1} there will be on average $\sim$ 1000 particles traversing the tracker for each bunch crossing (every 25 ns).

The CMS tracker design is based entirely on silicon detector technology. This technology features high granularity and fast response, such that the trajectories of charged particles can be identified reliably and attributed to the correct bunch crossing. Also it allows for keeping the amount of material to a minimum in order to limit multiple scattering, bremsstrahlung, photon conversion and nuclear interactions. Finally, the CMS silicon tracker is expected to operate in a severe radiation environment due to intense particle flux for a lifetime of $\sim$ 10 years. With about 200 m^2 of active silicon area the CMS tracker is the largest silicon tracker ever built.

The CMS tracker is composed of a pixel detector with three barrel layers at radii between 4.4 cm and 10.2 cm and a silicon strip tracker with 10 barrel detection layers extending outwards to a radius of 1.1 m as shown in Figure 3-7. The pixel detector is completed by 2 disks in endcaps. The strip tracker has 3 plus 9 disks on each side of the barrel, extending the acceptance of the tracker up to a pseudorapidity [5] of $\eta < 2.5$.

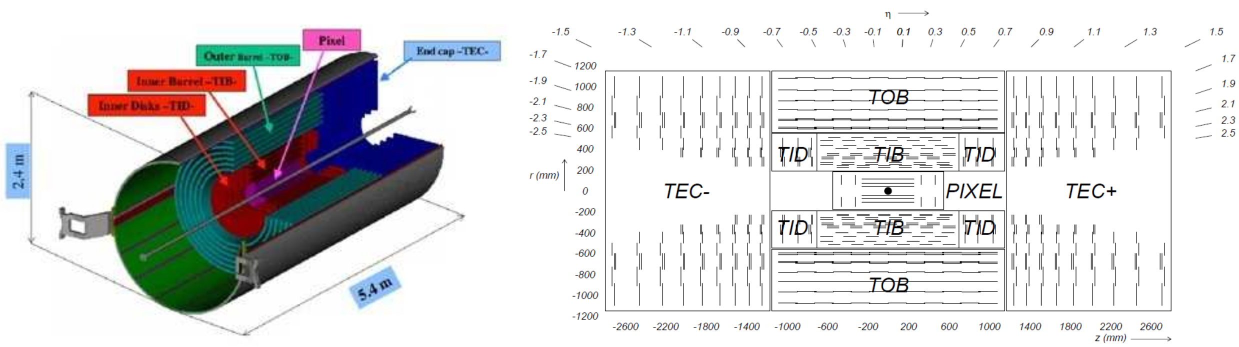

Figure 3-7. Left: perspective drawing of the CMS tracker. Right: schematic cross section through the CMS tracker. Each line represents a detector module.

The pixel detector delivers three high precision space points (hits) on each charged particle trajectory. In total the pixel detector covers an area of about 1 m^2, has 1440 modules and 66 million pixels. Technologically the pixels consist of high dose n-implants introduced into a high resistance n-substrate (double sided n-on-n concept). The sensor temperature is maintained at about $-10 \div -15°$C to reduce the effects of radiation damage; liquid phase cooling with C_6F_{14} is used with total flow rate of 1 litre/s. The particle detection inefficiency (due to read-out architecture data loss) has been measured in a high-rate pion beam. It reaches 0.8%, 1.2% and 3.8% respectively for the three layers at LHC design luminosity of 10^{34} $cm^{-2}s^{-1}$ and 100 kHz rate. The pixel system is inserted as the last sub-detector of CMS after the central section of the beam pipe has been installed and baked out.

This silicon strip tracker delivers at least nine hits in the full range of acceptance $|\eta| < 2.4$ with at least four of them being two-dimensional measurements. In total the silicon strip tracker covers an area of about 198 m^2, has 15148 modules, 24244 sensors

[5] $\eta = -\ln(\tan\theta/2)$, where θ is the polar angle of a particle relative to the beam axis

and 9.3 million strips. Technologically the sensor element on the strips consists of p-implants introduced into a high resistance n-substrate (single sided p-on-n concept). The sensor temperature is maintained at about $-10 \div -25$°C to reduce the effects of radiation damage; liquid phase cooling with C_6F_{14} is used with total flow rate of 2.4 kg/min. The measured hit finding efficiency is above 95%.

Alignment of the inner tracker system relies on three key components: the various data about assembly gathered during the integration process (average accuracy of 150 μm), the Laser Alignment System (average accuracy of 100 μm) and the alignment with tracks (average accuracy of 60 μm).

Material budget of the CMS tracker in units of radiation length[6] increases from $0.4X_0$ at η = 0 to about $1.8X_0$ at $|\eta| \approx 1.4$, beyond which it falls to about $1X_0$ at $|\eta| \approx 2.5$.

3.3.5 Electromagnetic Calorimeter System

One of the driving criteria in the Electromagnetic Calorimeter (ECAL) design was the capability to detect the decay to two photons of the postulated Higgs boson. The use of high density lead tungstate (PbWO4) crystals has allowed the design of a calorimeter which is fast, has fine granularity and is radiation resistant. Avalanche photodiodes (APD) are used as photodetectors in the barrel and vacuum phototriodes (VPT) in the endcaps.

The barrel part of the ECAL (EB) covers the pseudorapidity range $|\eta| < 1.479$. The barrel granularity is 360-fold in ϕ and (2×85)-fold in η, resulting in a total of 61200 crystals. The crystals have a tapered shape, slightly varying with position in η. They are mounted in a quasi-projective geometry to avoid cracks aligned with particle trajectories, so that their axes make a small angle (3°) with respect to the vector from the nominal interaction vertex, in both the ϕ and η projections. The lead tungstate crystal

[6] X_0 [$g \cdot cm^{-2}$], scaling variable for the probability of occurrence of bremsstrahlung (for electrons) and pair production (for photons)

cross-section corresponds to approximately 0.0174 $\times$ 0.0174 in $\eta - \phi$ or 22 $\times$ 22 mm^2 at the front face of crystal and 26 $\times$ 26 mm^2 at the rear face. The crystal length is 230 mm corresponding to 25.8X_0. The barrel crystal volume is 8.14 m^3 and the weight is 67.4 ton.

The endcap parts of the ECAL (EE) cover the pseudorapidity range 1.479 $< |\eta| <$ 3.0. The longitudinal distance between the interaction point and the endcap envelope is 315.4 cm, taking account of the estimated shift toward the interaction point by 1.6 cm when the 4 T magnetic field is switched on. The endcap consists of identically shaped lead tungstate crystals grouped in mechanical units of 5 $\times$ 5 crystals (supercrystals, or SCs). Each endcap is divided into 2 halves, or Dees. Each Dee holds 3662 crystals. These are contained in 138 standard SCs and 18 special partial supercrystals on the inner and outer circumference. The crystals and SCs are arranged in a rectangular x-y grid, with the crystals pointing at a focus 1300 mm beyond the interaction point, giving off-pointing angles ranging from 2 to 8 degrees. The crystals have a rear face cross section 30 $\times$ 30 mm^2, a front face cross section 28.62 $\times$ 28.62 mm^2 and a length of 220 mm corresponding to 24.7X_0. The endcaps crystal volume is 2.90 m^3 and the weight is 24.0 ton. The layout of the calorimeter is shown in Figure 3-8.

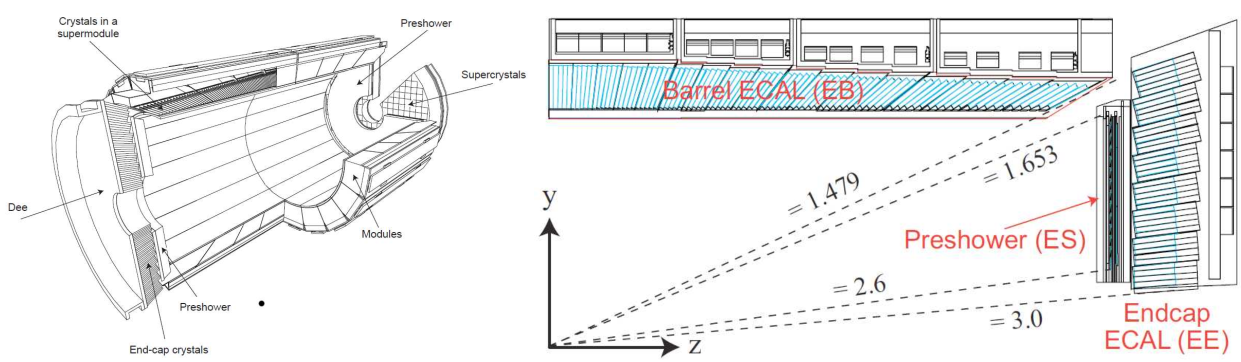

Figure 3-8. Left: perspective drawing of the CMS electromagnetic calorimeter showing the arrangement of crystal modules, supermodules and endcaps, with the preshower in front. Right: transverse section through the CMS electromagnetic calorimeter, showing geometrical configuration.

A preshower detector is placed in front of the endcap crystals. The principal aim of the preshower detector is to identify neutral pions in the endcaps within a fiducial region $1.653 < |\eta| < 2.6$. It also helps the identification of electrons against minimum ionizing particles, and improves the position determination of electrons and photons with high granularity.

The preshower detector is a sampling calorimeter with two layers: lead radiators initiate electromagnetic showers from incoming photons/electrons whilst silicon strip sensors placed after each radiator measure the deposited energy and the transverse shower profiles. The total thickness of the preshower is 20 cm.

A typical energy resolution of the ECAL from beam-test runs taken in 2006 is

$$\left(\frac{\sigma}{E}\right)^2 = \left(\frac{2.8\%}{\sqrt{E}}\right)^2 + \left(\frac{0.12}{E}\right)^2 + (0.30\%)^2 \,,$$

where E is energy of incident electrons in GeV.

3.3.6 Hadron Calorimeter System

The hadron calorimeter sits behind the tracker and the electromagnetic calorimeter as seen from the interaction point. The hadron calorimeter barrel is radially restricted between the outer extent of the electromagnetic calorimeter (R = 1.77 m) and the inner extent of the magnet coil (R = 2.95 m). This constrains the total amount of material which can be put in to absorb the hadronic shower. Therefore, an outer hadron calorimeter or tail catcher is placed outside the solenoid complementing the barrel calorimeter. Beyond $|\eta| = 3$, the forward hadron calorimeters placed at 11.2 m from the interaction point extend the pseudorapidity coverage down to $|\eta| = 5.2$ using a Cherenkov-based, radiation-hard technology. The hadron calorimeter tower segmentation in the (r; z) plane for one-fourth of the barrel (HB), endcap (HE) and outer (HO) detectors is shown in Figure 3-9 (left).

The hadron barrel detector (HB) is a sampling calorimeter covering the pseudorapidity range $|\eta| = 1.3$. The HB consists of 36 identical azimuthal wedges which form the two

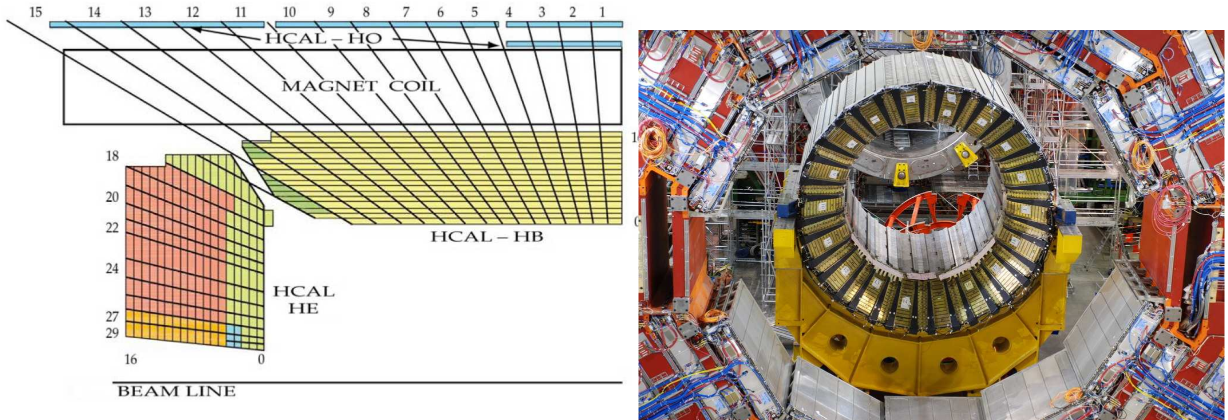

Figure 3-9. Left: the hadron calorimeter tower segmentation in the (r; z) plane for one-fourth of the barrel (HB), endcap (HE) and outer (HO) detectors. The shading represents the optical grouping of scintillator layers into different longitudinal readouts. Right: photo of assembled hadron calorimeter half-barrel.

half-barrels (HB+ and HB$-$). The wedges are constructed out of flat brass absorber plates aligned parallel to the beam axis. Each wedge is segmented into four azimuthal angle sectors. The innermost and outermost plates are made of stainless steel for structural strength. The plastic scintillator is divided into 16η sectors, resulting in a segmentation $(\delta\eta; \delta\phi) = (0.087; 0.087)$. The crack between the wedges is less than 2 mm. The absorber consists of a 40-mm-thick front steel plate, followed by eight 50.5-mm-thick brass plates, six 56.5-mm-thick brass plates, and a 75-mm-thick steel back plate. The total absorber thickness at 90° is 5.82 interaction lengths (λ_I). The HB effective thickness increases with polar angle as $1/\sin\eta$, resulting in 10.6λ_I at $|\eta| = 1.3$. The electromagnetic crystal calorimeter in front of HB adds about 1.1λ_I of material.

The hadron calorimeter endcaps (HE) cover a substantial portion of the rapidity range, $1.3 < |\eta| < 3$ (13.2% of the solid angle), a region containing about 34% of the particles produced in the final state. The 300-ton HE is attached to the muon endcap yoke. A 10-ton electromagnetic calorimeter (EE) with a 2-ton preshower detector (ES) is attached at the front face of HE. The brass plates (HE absorber) are 79-mm-thick with 9-mm gaps to accommodate the scintillators. The total length of the calorimeter, including electromagnetic crystals, is about 10λ_I. The scintillator is painted along the narrow edges and put into a frame to form a tray. The total number of tiles for both HE calorimeters is 20916 and the number of trays is 1368. The granularity of the calorimeters is $(\delta\eta;\delta\phi)$ = (0.087; 0.087) for $|\eta| < 1.6$ and $(\delta\eta;\delta\phi)$ = (0.17; 0.17) for $|\eta| \geq 1.6$.

3.3.7 Muon System

The CMS muon system is designed to have the capability of reconstructing the momentum and charge of muons over the the entire kinematic range of the LHC. CMS uses 3 types of gaseous particle detectors for muon identification. Due to the shape of the solenoid magnet, the muon system was naturally driven to have a cylindrical barrel section and 2 planar endcap regions. The muon system consists of about 25000 m^2 of detection planes.

3.3.7.1 Cathode Strip Chambers in Endcaps

The technology chosen for the Endcap Muon (EMU) system [132–134] is cathode strip chambers (CSC) [135, 136], the concept of which was first proposed by G. Charpak more than 30 years ago [137]. The CMS CSCs detect muon tracks in the pseudorapidity range $0.9 < |\eta| < 2.4$. The CMS EMU system will consist of 468 six-plane CSCs. The total sensitive area of all CSC planes is about 5 000 m^2 with about 2 000 000 wires.

The CMS cathode strip chambers are mounted on steel disks close off the CMS magnet and are set perpendicular to the beam axis (Figure 3-10). When viewed from inside of the LHC ring, the left and right Muon Endcaps of CMS are denoted by ME$-$ and ME+, respectively. There are 4 stations of chambers on each side of the detector, ME$\pm z_n$, where z_n ranges from 1 (the closest stations to the interaction point) to 4 (the outermost stations). The muon stations have 1, 2, or 3 rings of chambers, each ring being labeled as ME$\pm z_n/r_n$ (Figure 3-10 (left)). The rings themselves consist of either 18 or 36 trapezoidal chambers spanning 20° or 10° in azimuth ϕ. The chambers have labels ME$\pm z_n/r_n/\phi_n$. All CSCs, except for those forming the ME$\pm$1/3 rings, overlap to provide contiguous coverage in ϕ. A photo of the ME+2 disk is shown in Figure 3-10 (right).

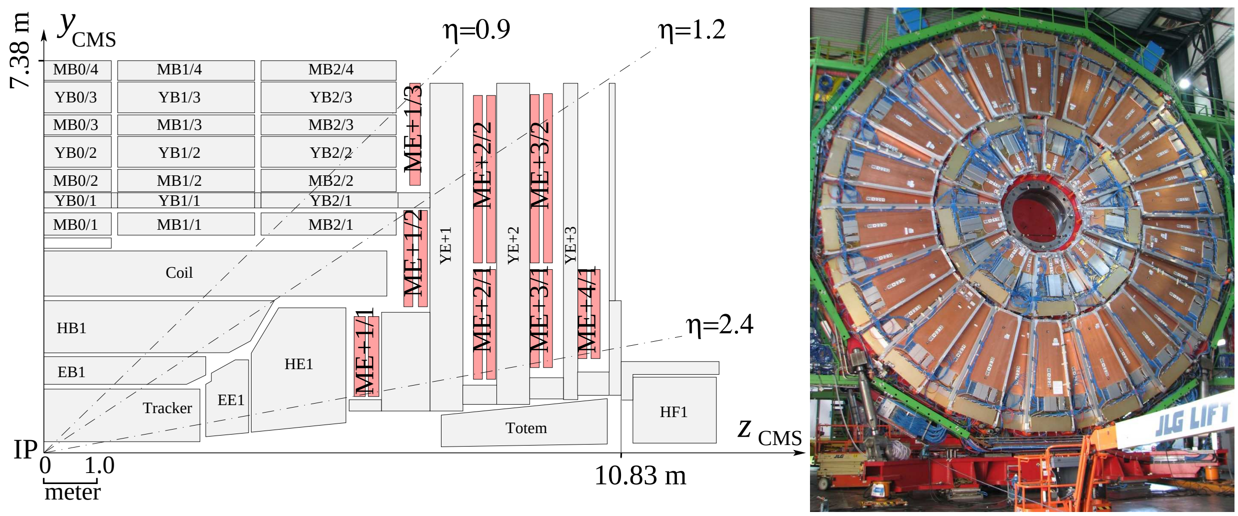

Figure 3-10. Left: A schematic quarter-view of the CMS detector (CSCs of the Endcap Muon system are highlighted; ME stands for Muon Endcap chambers). Right: A photo of the ME+2 disk and its stations of cathode strip chambers.

The CMS CSCs are comprised of 6 planes of anode wires interleaved between 7 trapezoidal cathode panels (Figure 3-11 (left)). Most of the CSCs have a gas gap between the cathode panels of about 1 cm. An electron avalanche caused by a muon traversing a gas gap produces a signal on the anode wires (Figure 3-11 (right top)) which induces a distributed charge on the cathode strips (Figure 3-11 (right bottom)) [132, 137]. By reading out signals from wires and strips, CMS CSCs measure 2 muon coordinates: the distance from the beam line r and the azimuthal angle ϕ in each of the 6 planes. As a muon goes through the CMS detector in the strong (4 T) magnetic field produced by the central solenoid, the change in its ϕ-coordinates allows its transverse momentum to be measured. Hence, the requirements on the precision of measuring ϕ-coordinates are more stringent than those for r-coordinate measurements.

Wires run azimuthally and define the y coordinate of the muon track in the chamber's local coordinate system (Figure 3-11 (left)). For readout purposes, the wires are arranged into groups. Each group consists of five to sixteen wires and spans 1.6–5 cm in width. Wire group signals are amplified and shaped to a standard pulse. The general idea of a pattern of wire group hits created by a muon is illustrated in Figure 3-12 (left).

Strips are milled on the cathode panels and run lengthwise at a constant $\Delta\phi_s$ width. The angular strip width $\Delta\phi_s$ varies for different chamber types from $\approx$ 2–5 mrad, while the spatial width varies from $\approx$ 4–16 mm, depending on the chamber type and local chamber y coordinate. By comparing signal amplitudes on nearby strips, the CSC electronics quickly measure the muon x coordinate to a precision of half a strip width [138]. This information, the so-called cathode comparator hits, is used by the muon Level-1 trigger. Strip signals are also digitized by 12-bit ADCs. By interpolating such digitized signals in all 6 planes, a muon's x-coordinate in a chamber is measured with a precision of $\approx$ 75–150 μm (cf. a typical sagitta of a muon with a transverse momentum p_T = 100 GeV as measured between IP, ME1, and ME2 stations is about 4 mm [132]). This information is available for the High-Level Trigger (HLT) and offline analyses. Figure 3-12 (right) illustrates a pattern of induced charges on strips and half-strip bits created by a muon.

Details on chamber locations and their internal geometrical parameters are given in reference [132].

3.3.7.2 Drift Tubes in Barrel

In the barrel region, where the neutron-induced background is small, the muon rate is low, and the 4-T magnetic field is uniform and mostly contained in the steel yoke, drift chambers with standard rectangular drift cells are used. The barrel drift tube (DT) chambers cover the pseudorapidity region $|\eta| < 1.2$ and are organized into 4 stations interspersed among the layers of the flux return plates. The first 3 stations each contain 8 chambers, in 2 groups of 4, which measure the muon coordinate in the $(r;\phi)$ bending plane, and 4 chambers which provide a measurement in the z direction, along the beam line. The fourth station does not contain the z-measuring planes. The 2 sets of 4

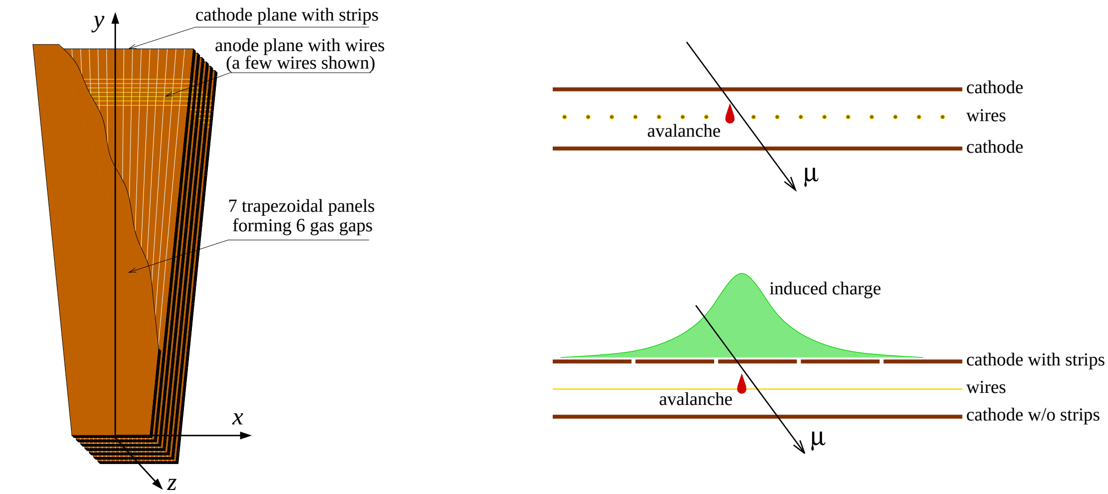

Figure 3-11. Left: Schematic view of a CMS cathode strip chamber. The cutout in the top panel allows one to see the radial fan-shaped cathode strips and anode wires running across the strips (only a few wires are shown). Right: An illustration of the CSC operation principle. An electron avalanche resulting from a muon traversing a gas gap produces a signal on the anode wires which induces a distributed charge on cathode strips.

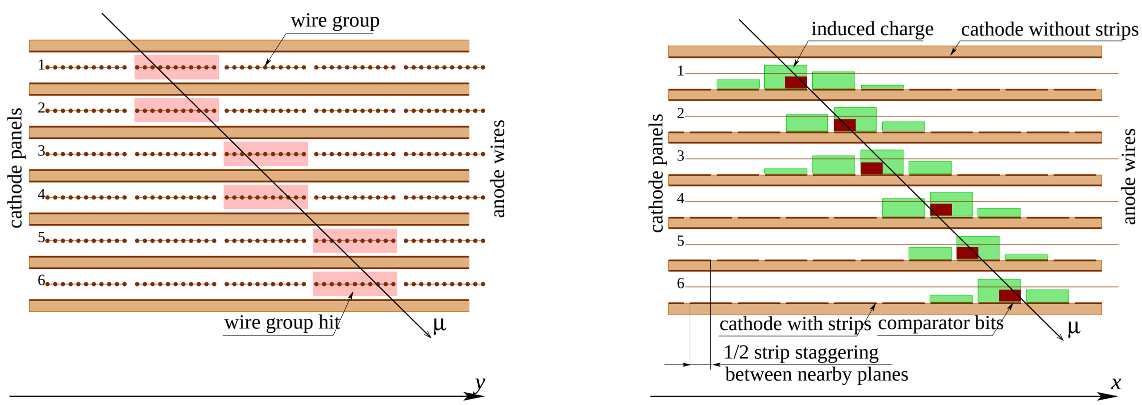

Figure 3-12. Left: A pattern of wire group hits created by a muon passing through a CSC. Right: A pattern of induced charges on strips and comparator half-strip hits created by a passing muon.

chambers in each station are separated as much as possible to achieve the best angular resolution. The drift cells of each chamber are offset by a half-cell width with respect to their neighbor to eliminate dead spots in the efficiency. This arrangement also provides a convenient way to measure the muon time with excellent time resolution, using simple meantimer circuits, for efficient, standalone bunch crossing identification. The number of chambers in each station and their orientation were chosen to provide good efficiency for linking together muon hits from different stations into a single muon track and for rejecting background hits.

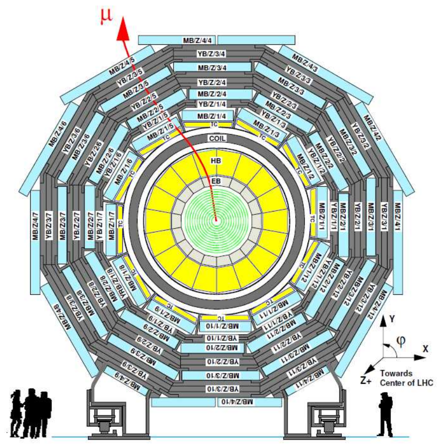

Figure 3-13. Schematic layout of the CMS muon drift tubes chambers on one of the 5 barrel wheels.

3.3.7.3 Resistive Plate Chambers

Because of the uncertainty in the eventual background rates and in the ability of the muon system to measure the correct beam-crossing time when the LHC reaches full luminosity, a complementary, dedicated trigger system consisting of resistive plate chambers (RPC) was added in both the barrel and endcap regions. The RPCs provide a fast, independent, and highly-segmented trigger with a sharp pT threshold over a large portion of the rapidity range ($|\eta| < 1.6$) of the muon system. The RPCs are double-gap chambers operated in avalanche mode to ensure good operation at high rates. They produce a fast response, with good time resolution but coarser position resolution than the DTs or CSCs. They also help to resolve ambiguities in attempting to make tracks from multiple hits in a chamber.

A total of 6 layers of RPCs are embedded in the barrel muon system, 2 in each of the first 2 stations, and 1 in each of the last 2 stations. The redundancy in the first 2 stations allows the trigger algorithm to work even for low-p_T tracks that may stop before reaching the outer 2 stations. In the endcap region, there is a plane of RPCs in each of the first 3 stations in order for the trigger to use the coincidences between stations to reduce background, to improve the time resolution for bunch crossing identification, and to achieve a good p_T resolution.

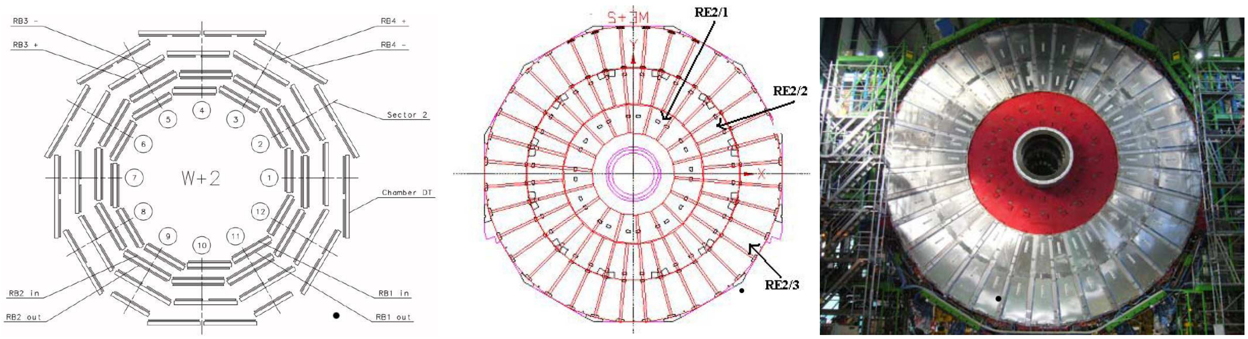

Figure 3-14. Left: Schematic layout of RPC station RB on one of the 5 barrel wheels. Center: schematic (r; ϕ) layout of RPC station RE2 on the back side of the first endcap yoke. Right: photo of RPC station RE2 on the back side of the YE-1 yoke. The inner ring has been staged and is absent here.

3.3.8 Trigger, Data Acquisition and Offline Computing Systems

The LHC provides proton-proton collisions at high interaction rates. The beam crossing interval is 25 ns, corresponding to a crossing frequency of 40 MHz. Also, depending on luminosity, several collisions occur at each crossing of the proton bunches. Since it is impossible to store and process the large amount of data associated with the resulting high number of events, a drastic rate reduction has to be achieved. This task is performed by the trigger system, which is the start of the physics event selection process. The rate is reduced in two steps called Level-1 (L1) Trigger and High-Level Trigger (HLT), respectively. The Level-1 Trigger consists of custom-designed, largely programmable electronics, whereas the HLT is a software system implemented in a filter farm of about one thousand commercial processors. The rate reduction capability is designed to be at least a factor of 10^6 for the combined L1 Trigger and HLT. The design output rate limit of the L1 Trigger is 100 kHz, which translates in practice to a calculated maximal output rate of 30 kHz, assuming an approximate safety factor of three. The L1 Trigger uses coarsely segmented data from the calorimeters and the muon system, while holding the high-resolution data in pipelined memories in the front-end electronics. The HLT has access to the complete read-out data and can therefore perform complex calculations similar to those made in the analysis off-line software if required for especially interesting events.

The architecture of the CMS Data Acquisition (DAQ) system is shown schematically in Figure 3-15. The DAQ system must sustain a maximum input rate of 100 kHz, for a data flow of $\approx$ 100 GByte/s coming from approximately 650 data sources, and must provide enough computing power for a software filter system, the HLT, to reduce the rate of stored events by a factor of 1000. In CMS all events that pass the Level-1 (L1) trigger are sent to a computer farm (Event Filter) that performs physics selections using faster versions of the offline reconstruction software, to filter events and achieve the required output rate.

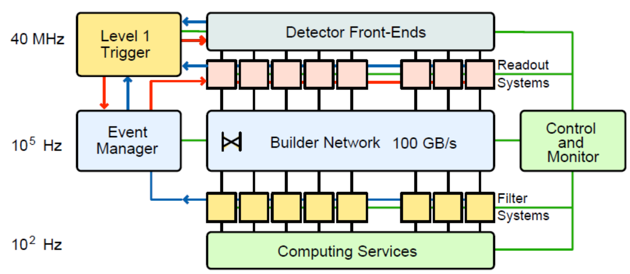

Figure 3-15. Architecture of the CMS DAQ system.

The CMS offline computing system must support the storage, transfer and manipulation of the recorded data for the lifetime of the experiment. The system accepts real-time detector information from the data acquisition system at the experimental site; performs pattern recognition, event filtering, and data reduction; supports the physics analysis activities of the collaboration. The system also supports production and distribution of simulated data, and access to conditions and calibration information and other non-event data.

3.4 First Results of the Experiment

3.4.1 The CMS Results with Cosmic Muons

Building a complex system, such as the CMS detector, required numerous tests to be done. The natural way to make such tests is to use muons from cosmic-ray interactions in the atmosphere. The CMS detector underwent a few major tests described below.

All the installation and commissioning of the CMS had been done in a surface hall before all the disks and wheels were lowered to LHC cavern at Point 5. Operation of all the sub-detectors and sub-systems of the CMS together was done in Fall 2006 during Magnet Test and Cosmic Challenge (MTCC06). The participating systems included a 60° sector of the muon system, both in the Barrel and Endcaps. The inner tracking system, electromagnetic and hadron calorimeter participate in the test at least at the 10% level. Other exercises included maneuvering large elements of the detector, operation in magnetic field, coherent running of subsystems, operational and safety procedures.

One of the results of MTCC06, the measurement of efficiency of finding muon track trigger primitives in cathode strip chambers, is part of this thesis and described in Chapter 5. Other major results and lessons learned during MTCC06 are reviewed in [139].

After the lowering of the CMS detector down to the LHC cavern at Point 5 in Fall 2008 a month-long data-taking run was performed. It was called Cosmic Run At (almost) Four Tesla (CRAFT08). The aim of the test was to run the CMS continuously as a complete experiment, 24 hours a day, to gain operational experience even without LHC beams. Data from 300 million cosmic muons (including more than 7 million tracks in the strip tracker and around 75000 tracks in the pixel tracker) were recorded with the solenoid at its operating point of 3.8 T for detailed detector studies.

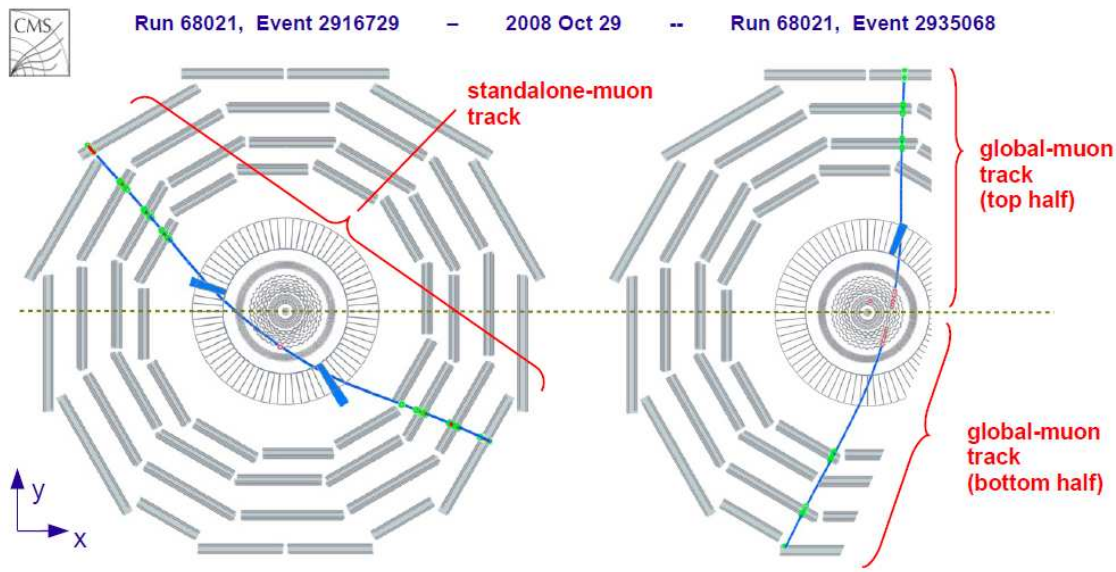

Figure 3-16. Left: standalone cosmic muon crossing the CMS detector from top to bottom, recorded in CRAFT08, leaving signals in the muon system, and calorimeters. Right: global cosmic muon crossing the CMS detector from top to bottom, recorded in CRAFT08, leaving signals in the muon system, tracking detectors and calorimeters [140].

One of the result of CRAFT08 was the measurement of the flux ratio of positive and negative cosmic muons. The excellent performance of the CMS detector allowed detection of muons in the momentum range from 3 GeV/c to 1 TeV/c. The event displays of the cosmic muons crossing the CMS detector are shown in Figure 3-16. For muon momenta below 100 GeV/c the flux ratio is measured to be a constant $1.2766 \pm 0.0032(stat) \pm 0.0032(syst)$, the most precise measurement to date. Further details on the measurement can be found elsewhere [140]. Other major results and lessons learned during CRAFT08 are reviewed in [141].

3.4.2 The LHC Timeline

The LHC timeline consists of following events:

- September 10th, 2008 — first proton beams successfully circulated full turn.
- September 19th, 2008 — quench occurred in bending dipoles in sectors 3 and 4.
- September 20th, 2009 — proton beams with 450 GeV energy per beam circulated.

- September 23rd, 2009 — first proton collisions with 450 GeV energy per beam registered in all four detectors.
- November 30th, 2009 — proton beams with 1.18 TeV energy per beam circulated.
- February 28th, 2010 — proton beams with 3.5 TeV energy per beam circulated.
- March 30th, 2010 — first proton collisions with 3.5 TeV energy per beam registered. Research program of the LHC starts.

By the end of the May 2010 all four experiments collected $\sim$ 15 nb^{-1} of integrated luminosity as shown in Figure 3-17. This luminosity is enough to look into QCD processes like J/ψ production. It also allows to see first W and Z boson events.

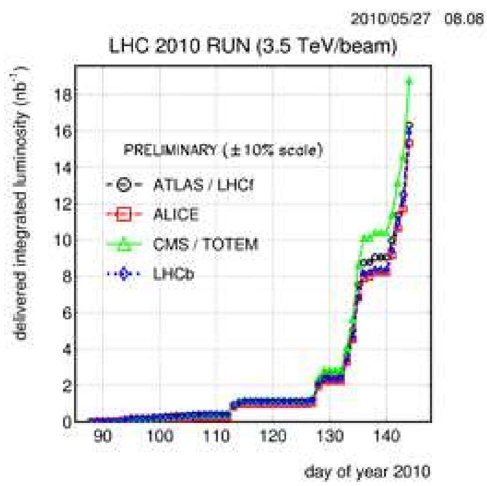

Figure 3-17. The luminosity integrated by the four LHC experiments.

3.4.3 The CMS Results with *pp* Collisions at $\sqrt{s}$ = 0.9 TeV and $\sqrt{s}$ = 2.36 TeV

Various QCD measurements were performed in proton-proton collisions at $\sqrt{s}$ = 0.9 TeV and $\sqrt{s}$ = 2.36 TeV, using data collected by the CMS experiment at the LHC. The underlying event activity in scattering processes with p_T scale in the GeV region was studied [142]. Also Bose-Einstein correlations have been measured [143]. The signal was observed in the form of an enhancement of pairs of same-sign charged particles with small relative four-momentum. And finally, inclusive charged-hadron transverse-momentum and pseudorapidity distributions were studied [144].

3.4.4 The CMS Results with *pp* Collisions at $\sqrt{s}$ = 7 TeV

Clearly visible spikes (Figure 3-18) in invariant mass distributions corresponding to $J/\psi \rightarrow \mu\mu$ and $J/\psi \rightarrow ee$ have been observed [145]. In di-electron channel low p_T electrons were selected. Same sign and opposite sign combinations were separately plotted. Binned likelihood fit of a gaussian and constant value in the mass range 1.5–4.5 GeV was performed. Claimed signal is the integral of the gaussian; background quoted in $\pm 2.5\sigma$ around the mean value.

In the di-muon channel, low p_T muons were selected. Extended maximum likelihood fits were performed with an exponential for the background and a Crystal Ball function[7] for the signal in order to account for radiative tails. Claimed number of signal events is 1230 ± 47.

The *W* and *Z* inclusive production at $\sqrt{s}$ = 7 TeV with the CMS experiment at the LHC have been observed [146]. The events with an isolated muon of good quality with $p_T > 25$ GeV accompanied by acoplanar track-corrected missing transverse energy were selected as $W \rightarrow \mu\nu$ candidates. Events with two or more muons were rejected. An event display of a selected $W \rightarrow \mu\nu$ candidate is shown in Figure 3-19 (left). Distribution of transverse mass of selected $W \rightarrow \mu\nu$ events is shown in Figure 3-19 (right). The cross sections in Monte Carlo on this plot are normalized to MCFM NLO predictions using MSTW08 NLO PDFs and to the estimated CMS luminosity of 16 nb^{-1} for the good runs and luminosity sections considered in data. Signal shape is NLO (POWHEG). Backgrounds include: $Z \rightarrow \mu\mu$ (NLO, POWHEG), $W \rightarrow \tau\nu$ (PYTHIA), $Z \rightarrow \tau\tau$ (PYTHIA), and $t\bar{t}$ (PYTHIA). The QCD background is PYTHIA leading order processes.

The events with isolated electrons of good quality with electromagnetic cluster $E_T > 10$ GeV accompanied by missing transverse energy, with an additional cut on

[7] The Crystal Ball function consists of a Gaussian core and a power-law low-end tail.

$\sum E_T$ to make sample purer, were selected as $W \to e\nu$ candidates. An event display of a selected $W \to e\nu$ candidate is shown in Figure 3-20 (left). Distribution of transverse mass of selected $W \to e\nu$ events is shown in Figure 3-20 (right). Background processes were generated with PYTHIA in leading order. The signal was rescaled to the NLO cross section and normalized to integrated luminosity.

The events with two isolated muons with $p_T > 20$ GeV were selected as $Z \to \mu\mu$ candidates. The number of selected events is 5 for 16 nb^{-1} of integrated luminosity. An event display of a selected $Z \to \mu\mu$ candidate is shown in Figure 3-21 (left). Distribution of the invariant mass of selected $Z \to \mu\mu$ events is shown in Figure 3-21 (right). The cross sections in Monte Carlo on this plot are normalized to MCFM NLO predictions using MSTW08 NLO PDFs and to the estimated CMS luminosity of 16 nb^{-1} for the good runs and luminosity sections considered in data. Backgrounds include: $W \to \mu\nu$, and $t\bar{t}$. The QCD background is PYTHIA leading order processes.

The events with two isolated electrons of loose identification qualities with electromagnetic cluster $E_T > 10$ GeV were selected as $Z \to ee$ candidates. Number of selected events is 5 for 16.6 nb^{-1} of integrated luminosity. An event display of a selected $Z \to ee$ candidate is shown in Figure 3-22 (left). The distribution of invariant mass of selected $Z \to ee$ events is shown in Figure 3-22 (right). Background processes were generated with PYTHIA in leading order. The signal was rescaled to the NLO (POWHEG) cross section and normalized to integrated luminosity.

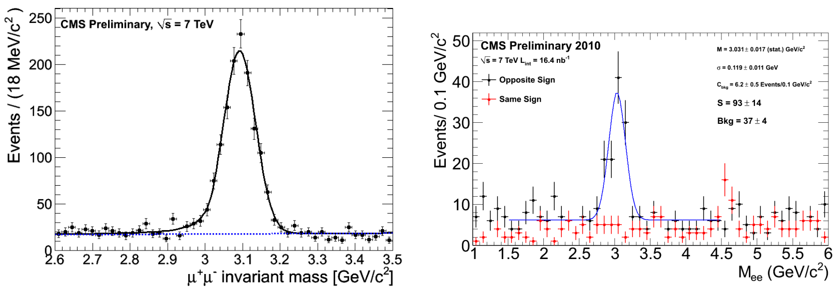

Figure 3-18. Left: Invariant mass distribution of the $J/\psi \to \mu\mu$ events. Right: Invariant mass distribution of the $J/\psi \to ee$ events.

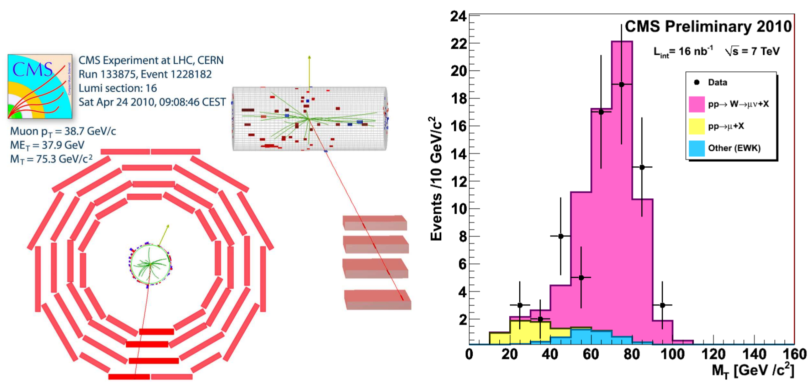

Figure 3-19. Left: Event display of the $W \to \mu\nu$ candidate. Right: Transverse mass distribution of the $W \to \mu\nu$ events.

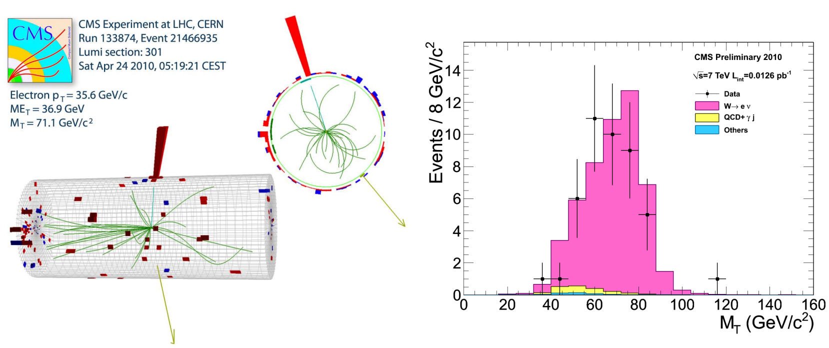

Figure 3-20. Left: Event display of the $W \to e\nu$ candidate. Right: Transverse mass distribution of the $W \to e\nu$ events.

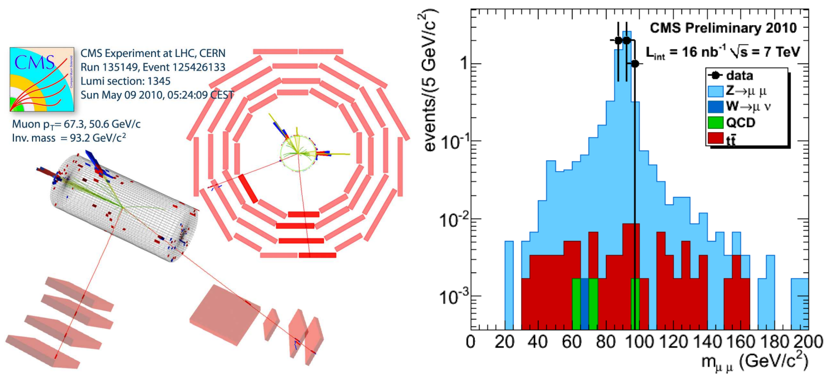

Figure 3-21. Left: Event display of the $Z \to \mu\mu$ candidate. Right: Invariant mass distribution of the $Z \to \mu\mu$ events.

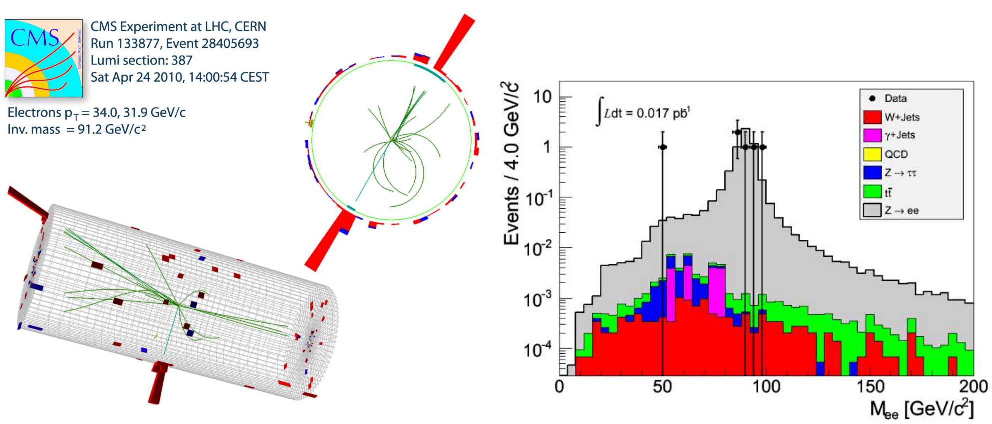

Figure 3-22. Left: Event display of the $Z \to ee$ candidate. Right: Invariant mass distribution of the $Z \to ee$ events.

CHAPTER 4
CMS DISCOVERY POTENTIAL FOR SUSY IN SAME-CHARGE DI-LEPTON EVENTS IN *PP* COLLISIONS WITH $\sqrt{S}$ = 7 TEV AND $\sqrt{S}$ = 10 TEV

4.1 Introduction

Same-charge di-lepton events provide a very clean experimental signature for a Supersymmetry (SUSY) search. As it is shown below, in this channel the Standard Model (SM) background can be suppressed almost to zero using reasonable cuts. The same-charge di-muon signature for SUSY has already been the subject of several studies [102–104] in CMS. This work extends those earlier studies to LHC energies $\sqrt{s}$ = 7 TeV and $\sqrt{s}$ = 10 TeV. Optimization of cuts is done in the assumption of initial low-luminosity running and projected exclusion limits together with 5σ discovery contours are reported for 100 pb^{-1} of integrated luminosity. Next-to-leading order cross sections were used for all SM backgrounds and SUSY samples. More complete treatment of SM backgrounds including data driven techniques has been done. In addition, both di-electron and electron-muon sigantures are included leading to an increase in sensitivity.

In parallel with this work the same channel has been studied in [147–149]. Similar sensitivities are reported.

Even though we perform our study within the context of mSUGRA, which is a popular 4-parameter model of supersymmetry, our method is not specific to the mSUGRA framework and applies equally well in other contexts. Indeed, our signature is quite generic in supersymmetry: the missing transverse energy is a necessary consequence of *R*-parity, the jets result from the decays of colored superpartners (squarks and gluinos) which are expected to be predominantly produced at the LHC, and prompt leptons can result from the decays of charginos, neutralinos or sleptons which may appear in the later stages of the squark and gluino decay chains (Figure 4-1). The requirement that the leptons have the same charge allows for an efficient suppression of the SM backgrounds, and at the same time retains much of the signal, as same-charge leptons can result from several signal processes. For example, the gluino, being a Majorana particle, has equal probability of yielding either a positively or a negatively charged lepton in its decay chain. Squark production is another important source of same-charge di-leptons, since the squark charge tends to be determined by the valence quarks in the proton-proton collision.

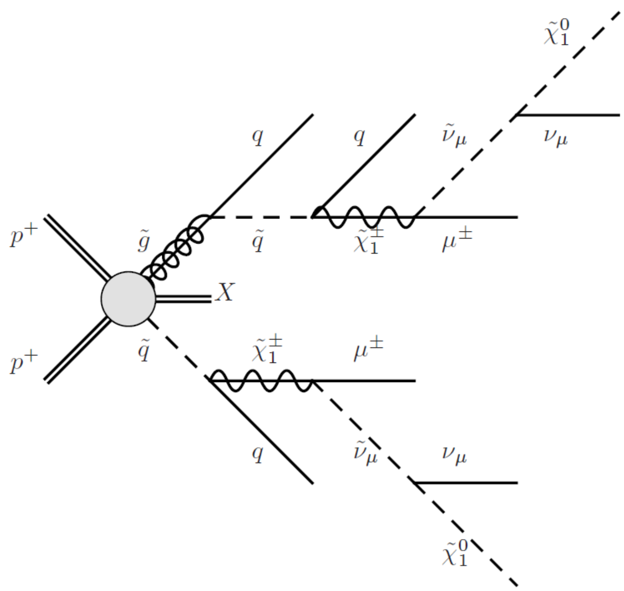

Figure 4-1. An example of diagram showing a squark-gluino production event following cascade decays, resulting in two same-charge muons.

Current exclusion limits on mSUGRA from LEP (combined result for all detectors) and Tevatron (CDF detector) experiments are shown in Figure 4-2. There are also limitations on the mSUGRA from non-collider experiments (dark matter density, $b \rightarrow s\gamma$, $g_\mu - 2$) that are not shown and can be found elsewhere.

A detailed description of the Compact Muon Solenoid (CMS) experiment can be found elsewhere [128].

4.2 Monte Carlo generation and detector simulation of data samples

4.2.1 Analysis Flow

This work uses the official fully simulated (FullSim) CMS Summer and Fall 2008 datasets ($\sqrt{s}$ = 10 TeV). SUSY signal and SM backgrounds data samples

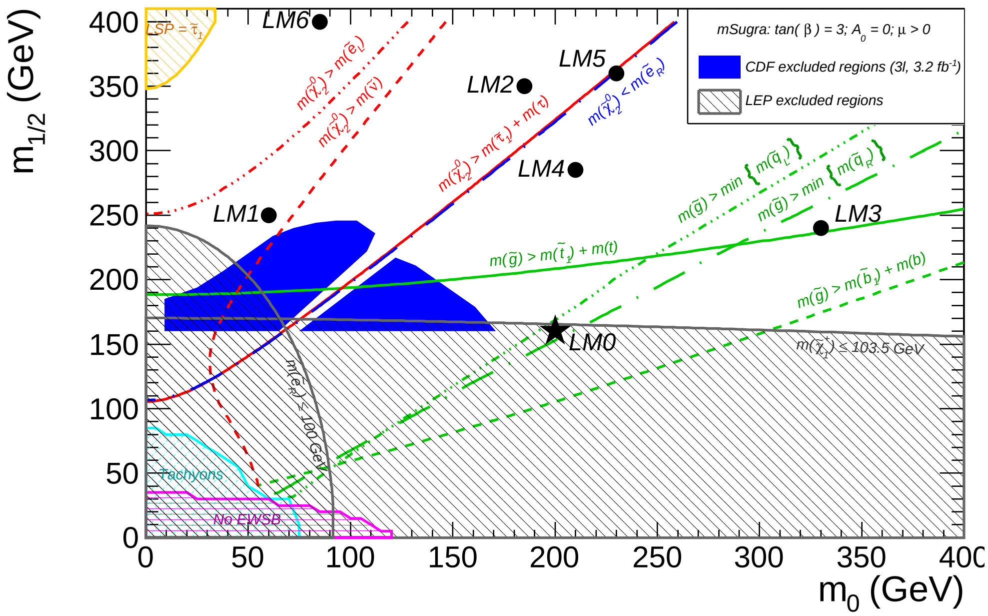

Figure 4-2. The LM0 mSUGRA sample used for optimization is shown as star ($\star$) in the m_0-$m_{1/2}$ parameters plane. Other official CMS mSUGRA benchmark points are shown as solid circles ($\bullet$). Other mSUGRA parameters (tanβ, signμ, and A_0) are fixed for each point as shown in Table 4-1. Excluded regions for mSUGRA with tanβ = 3, $\mu > 0$, and A_0 = 0 by particle experiments (LEP masses of chargino and sleptons — shaded area, CDF direct search for superpartners with trilepton signature — solid blue area) are also shown. Reference lines of equal masses for different superparticles are plotted.

were produced with various Monte Carlo (MC) generation softwares (see details in subsections 4.2.2 and 4.2.3). CMS Software (CMSSW) was used to generate stable particles, to simulate the passage of particles through the CMS detector and its response, to digitize all simulated hits and to reconstruct the digitized information. CMSSW 2.2.1 was used for all SM backgrounds samples and CMSSW 2.2.3 was used for all SUSY signal samples. All reconstructed datasets were processed with CMS Physics Analysis Tools (PAT) integrated into CMSSW 2.2.9. PAT objects were used in the analysis to select SUSY signal events.

4.2.2 Supersymmetry Signals

This work uses the official CMS Low Mass (LM) mSUGRA datasets made on Summer and Fall 2008 ($\sqrt{s}$ = 10 TeV). The spectra of supersymmetric particles were calculated by a program SOFTSUSY 2.0.17 [150] in the framework of the Minimal Supersymmetric Standard Model (MSSM), including higher order corrections. Decay widths and branching ratios of supersymmetric particles were calculated by a program SDECAY 1.2 [151]. These programs were interfaced together by a package SUSY-HIT [152]. Leading order cross sections then derived by PYTHIA 6 [153]. The same program wrapped into CMSSW was used to generate the mSUGRA signal datasets and the CTEQ6L1 [154] library was used for the parton distribution functions.

Table 4-1 displays the different parameters for all fully simulated and reconstructed mSUGRA points used in this analysis. There are ratio of the vacuum expectation values of the two Higgs fields (tan β); sign of the unmixed higgsino mass ($\mathtt{sign}\mu$); higgs-squark-squark trilinear coupling constant (A_0); universal scalar (m_0) and gaugino ($m_{1/2}$) masses. Masses of corresponding squarks and gluino for every benchmark points are also reported. See Figure 4-2 for relative location of the benchmark points in the m_0-$m_{1/2}$ parameters plane.

Table 4-1. Input parameters of fully simulated and reconstructed CMS mSUGRA benchmark points.

SUSY sample	tan β	A_0	$\mathtt{sign}\mu$	m_0 (GeV/c^2)	$m_{1/2}$ (GeV/c^2)	$m_{\tilde{u}_L}$ (GeV/c^2)	$m_{\tilde{g}}$ (GeV/c^2)
LM0	10	-400	+	200	160	415	409
LM1	10	0	+	60	250	552	603
LM2	35	0	+	185	350	770	827
LM3	20	0	+	330	240	619	597
LM4	10	0	+	210	285	653	687
LM5	10	0	+	230	360	800	851
LM6	10	0	+	85	400	850	932

Considering LHC center of mass energy $\sqrt{s}$ = 10 TeV the following parameters for the benchmark CMS mSUGRA points are summarized in Table 4-2: number of generated MC events and equivalent integrated luminosity; expected number of events and event weight for 100 pb^{-1} of integrated luminosity.

Table 4-2. Number of generated MC events of fully simulated and reconstructed CMS mSUGRA benchmark points.

$\sqrt{s}$ = 10 TeV				
SUSY sample	# events MC	equivalent $\int L$ (pb^{-1})	$\int L = 100\ pb^{-1}$	
			# events	event weight
LM0	202,686	1.2E+03	16,601	0.082
LM1	104,800	4.7E+03	2,246	0.021
LM2	130,400	3.9E+04	335	0.0026
LM3	153,000	9.0E+03	1,705	0.011
LM4	110,400	1.2E+04	940	0.0085
LM5	171,600	6.4E+04	268	0.0016
LM6	134,400	7.7E+04	174	0.0013

Fast generation and simulation (FastSim) was performed for both LHC center of mass energies ($\sqrt{s}$ = 7 TeV and $\sqrt{s}$ = 10 TeV) in order to scan the plane of universal scalar (m_0) and gaugino ($m_{1/2}$) masses (Figure 4-2) for fixed mSUGRA parameters: $\tan\beta = 3$, $\mu > 0$ and $A_0 = 0$. Datacards supplied by the SUSY/BSM group were used to generate additional mSUGRA datasets. The software package used to generate signal samples was PYTHIA 6. The mSUGRA spectrum of SUSY masses and mixing was calculated by SOFTSUSY. CTEQ6L1 was used for the parton distribution functions. The output files were processed by using CMSSW for fast detector simulation, reconstruction, and the production of PAT samples for analysis.

Points were generated on a coarse grid with Δm_0 = 10 GeV/c^2 and $\Delta m_{1/2}$ = 10 GeV/c^2, starting from the point m_0 = 0 GeV/c^2, $m_{1/2}$ = 150 GeV/c^2. For validation purposes, sample of the LM0 mSUGRA benchmark point at $\sqrt{s}$ = 10 TeV was also produced with fast simulation, and compared with the fully simulated data. It is shown in Appendix D that FullSim and FastSim samples are in very good coincidence.

Next-to-leading order cross sections were calculated for each FastSim SUSY sample using PROSPINO software [155]. The calculated k-factors and NLO cross sections for LHC center of mass energy $\sqrt{s}$ = 7 TeV in m_0-$m_{1/2}$ plane of SUSY parameters are shown in Figure 4-3. Cross sections in leading σ_{LO} and next-to-leading order σ_{NLO}, accompanied by k-factors and scale factors, for CMS mSUGRA benchmark points are shown in Table 4-3.

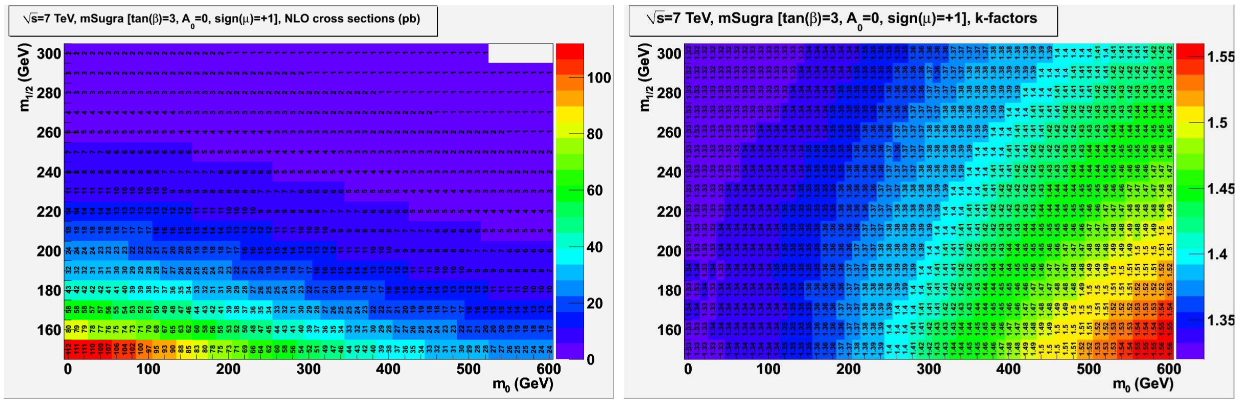

Figure 4-3. Next-to-leading order cross sections (left) and k-factors (right) for LHC center of mass energy $\sqrt{s}$ = 7 TeV in $m_0 - m_{1/2}$ plane of SUSY parameters. The other mSUGRA parameters are fixed to $\tan\beta = 3$, $\mu > 0$ and $A_0 = 0$.

Table 4-3. Cross sections of CMS mSUGRA benchmark points.

SUSY sample	$\sqrt{s}$ = 10 TeV σ_{LO} (pb)	k	σ_{NLO} (pb)	$\sqrt{s}$ = 7 TeV σ_{LO} (pb)	k	σ_{NLO} (pb)	scale $\frac{\sigma_{NLO}(10\,TeV)}{\sigma_{NLO}(7\,TeV)}$
LM0	110	1.51	166	38.9	1.48	57.7	2.88
LM1	16.1	1.40	22.5	4.89	1.39	6.79	3.31
LM2	2.42	1.38	3.35	0.603	1.36	0.819	4.09
LM3	11.8	1.45	17.1	3.44	1.42	4.89	3.49
LM4	6.70	1.40	9.40	1.88	1.36	2.56	3.67
LM5	1.94	1.38	2.68	0.473	1.33	0.631	4.24
LM6	1.28	1.36	1.74	0.31	1.31	0.405	4.30

4.2.3 Standard Model Backgrounds

4.2.3.1 Production of QCD

While QCD multi-jet events do not intrinsically involve Feynman diagrams producing final states similar to the topological signature required by this analysis, owing to its enormous cross section (see Table 4-4), QCD can produce final state configurations which are experimentally similar. In addition to multiple jets, significant missing E_T can be faked by mis-measurement of jet energies and muons can be produced in heavy flavor events or faked in several ways such as punch-through.

Table 4-4. Cross sections of QCD ($b\bar{b}$) background samples in different H_T ranges.

QCD ($b\bar{b}$) sample	$\sqrt{s}$ = 10 TeV σ_{LO} (pb)	$\sqrt{s}$ = 7 TeV σ_{LO} (pb)	scale $\frac{\sigma_{LO}(10\,TeV)}{\sigma_{LO}(7\,TeV)}$
$100 < H_T(GeV) < 250$	450000	210000	2.1
$250 < H_T(GeV) < 500$	15000	6413	2.3
$500 < H_T(GeV) < 1000$	700	260	2.7
$1000 < H_T(GeV) < \infty$	13	2.9	4.5

Due to a rapidly falling differential cross section, QCD multi-jets were generated roughly flat in different, non-overlapping bins of H_T using Madgraph software [156]. The number of fully simulated and reconstructed QCD events used in this work may be found in Table 4-5. Indeed, it is hopeless to generate enough QCD multi-jet events corresponding to low H_T ranges. This implies that generated events with $H_T \lesssim 500$ GeV/c are luminosity weighted higher (sometimes much higher) than unity in this analysis. In order to overcome the lack of MC generated events the data driven approach was developed to estimate QCD contribution into the SUSY search with same-charge di-leptons (see details in 4.5.1.1).

Table 4-5. Number of generated MC events of fully simulated and reconstructed QCD ($b\bar{b}$) background samples in different H_T ranges.

$\sqrt{s}$ = 10 TeV				
QCD ($b\bar{b}$) sample	# events MC	equivalent $\int L$ (pb^{-1})	$\int L$ = 100 pb^{-1} # events	event weight
$100 < H_T(GeV) < 250$	2,764,756	6.1E+00	45,000,000	16.3
$250 < H_T(GeV) < 500$	1,052,158	7.0E+01	1,500,000	1.43
$500 < H_T(GeV) < 1000$	1,030,233	1.5E+03	70,000	0.068
$1000 < H_T(GeV) < \infty$	357,618	2.8E+04	1,300	0.0036

4.2.3.2 Production of Top Quark Pairs

Another particularly important source of background is $t\bar{t}$ production. It has a fairly large cross-section (see Table 4-6), and produces multi-jet events with high MET, a significant number of which include leptons. A total of approximately 1 million inclusive $t\bar{t}$ events were simulated with Madgraph and used in this analysis, as shown in Table 4-7.

Table 4-6. Cross sections of SM (no QCD) background samples.

SM sample	$\sqrt{s}$ = 10 TeV			$\sqrt{s}$ = 7 TeV			scale
	σ_{LO} (pb)	k	σ_{NLO} (pb)	σ_{LO} (pb)	k	σ_{NLO} (pb)	$\frac{\sigma_{NLO}(10\,TeV)}{\sigma_{NLO}(7\,TeV)}$
$t\bar{t}$+Jets	317	1.31	415	95	1.74	165	2.52
W+Jets	40000	1.07	42761	24170	1.20	29040	1.47
Z+Jets	3700	1.14	4202	2400	1.17	2810	1.50
WW+Jets	44.8	1.59	71.4	28	1.53	42.9	1.67
WZ+Jets	17.40	1.80	31.4	10.5	1.74	18.3	1.72
ZZ+Jets	7.1	1.39	9.9	4.3	1.37	5.9	1.68

Table 4-7. Number of generated MC events of fully simulated and reconstructed SM (no QCD) background samples.

$\sqrt{s}$ = 10 TeV				
SM sample	# events MC	equivalent $\int L$ (pb^{-1})	$\int L$ = 100 pb^{-1}	
			# events	event weight
$t\bar{t}$+Jets	946,644	3.0E+03	41,500	0.044
W+Jets	9,338,174	2.3E+02	4,276,120	0.458
Z+Jets	1,262,816	3.4E+02	420,200	0.3327
WW+Jets	204,722	4.6E+03	7,140	0.035
WZ+Jets	246,550	1.4E+04	3,140	0.0127
ZZ+Jets	199,810	2.8E+04	990	0.0050

4.2.3.3 Production of Electro-Weak Single Bosons

The production of single W and Z bosons is expected to be plentiful at the LHC due to their high cross sections (see Table 4-6). A total of approximately 9.3 million inclusive W and 1.3 million inclusive Z events were simulated with Madgraph software and used in this analysis, as shown in Table 4-7.

The primary contribution of W+jets as a background process to this study is due to leptonic decays of the W into an isolated muon and a neutrino together with a non-isolated (possibly fake) muon produced in the recoiling jet(s). The primary contribution of Z+jets is due to di-lepton decays of the Z, together with a non-isolated (possibly fake) lepton produced in the recoiling jet(s).

4.2.3.4 Production of Electro-Weak Double Bosons

Di-boson production, such as WW+jets, WZ+jets, and ZZ+jets, also contribute as a source of background to this study, due to the existence of several final states involving muons, jets and large missing E_T. Because of the additional weak vertex, the cross sections are much less than for single boson production (see Table 4-6). The number of fully simulated and reconstructed electro-weak di-boson events used in this work may be found in Table 4-7.

4.3 Event Reconstruction

Event selection is performed at three levels: on-line selection at the trigger level, offline pre-selection at the skim level and offline selection at the analysis level. The algorithms to reconstruct the physical objects (muons, electrons, jets, etc) as well as their identification at the on-line and offline levels are described in Ref. [134].

4.3.1 Trigger

The trigger is composed of a hardware-based Level-1 (L1) Trigger system [157] and a software-based High-Level Trigger (HLT) system [158]. For *pp* collisions at $\sqrt{s}$ = 10 TeV and expected luminosity 10^{31} cm-2s^{-1} the event rate is reduced at Level-1 to 12 kHz, whilst the HLT uses the reconstructed object information to further reduce the bandwidth to 150 Hz written to mass storage. This work uses event samples selected by two unprescaled HLT triggers [159]. The di-muon trigger (`HLT_DoubleMu3`) with expected rate 0.79 Hz is used to select events with a same-charge di-muon signature. The di-electron trigger (`HLT_DoubleEle10_LW_OnlyPixelM_L1R`) with expected rate 19.96 Hz is used to select events with same-charge di-electron signature.

HLT trigger for $e\mu$ cross channel was not present in generated signal and background Monte-Carlo samples. This trigger (`HLT_L2Mu5_Photon9`) was recently studied and introduced into new HLT Table [160]. Its performance will be studied in full details with next version of Monte-Carlo samples.

4.3.2 Physics Objects Reconstruction and Identification

In general, the reconstruction and identification of leptons, jets and missing transverse energy used in the analysis is based on the algorithms recommended by corresponding CMS physics objects groups (POG).

4.3.2.1 Muons Reconstruction and Identification

The muon reconstruction and identification begins with finding position of hits in Muon System. These hits are used for muon outer track reconstruction. To benefit from the full CMS resolution, the outer track is then combined with matching inner track reconstructed in tracker system and refit is performed to produce global muon. In the analysis we used `pat::Muon` objects which are derived from global muons. Details on global muons reconstruction and identification can be found in [161] and [162].

In addition, for muons preselection we applied a few kinematic and identification cuts (see Table 4-8) following commonly used V+jets group baseline recommendations [163]. Muons are required to have $p_T \geq 5$ GeV. The specific pseudorapidity range $|\eta| \leq 2.4$ is motivated by the acceptance of muon system. To reduce the contamination from semi-leptonic heavy flavor decays we require the impact parameter with respect to offline beamspot of the tracker fit of the muon to be less than 0.02 cm.

To enhance the purity of global muons complementary quality cuts are applied. Muons used in the analysis have to satisfy the requirement of at least 11 valid hits in tracker fit. The normalized χ^2 of the global fit of the muon is required to be less than 10 (equal to that used to identify muons with `GlobalMuonPromptTight` identification requirement).

The energy deposit in the electromagnetic calorimeter (ECAL) within veto cone of $R = 0.07$ around the muon track is limited to 4 GeV to ensure the muon is consistent with a minimal ionizing particle. Also, the energy deposit in hadronic calorimeter (HCAL) within veto cone of $R = 0.1$ around the muon track is limited to 6 GeV.

4.3.2.2 Electrons Reconstruction and Identification

The electron reconstruction and identification begins with finding superclusters in electromagnetic calorimeter (ECAL). These superclusters are used as starting seeds to build electron tracks in pixel detector. The Bethe-Heitler model of electron energy

Table 4-8. Muon preselection cuts.

Reconstruction Algorithm	=	`GlobalMuon`
p_T	$\geq$	5 GeV
$\|\eta\|$	$\leq$	2.4
ID Type	=	`GlobalMuonPromptTight`
$\|d_0\|$ from tracker fit, beam corrected	$\leq$	0.02 cm
$\chi^2/n.d.o.f.$ of global fit	$<$	10
number of valid hits in tracker fit	$\geq$	11
ECAL Veto Cone Energy	$<$	4
HCAL Veto Cone Energy	$<$	6

loss is used. Details on electrons reconstruction and identification can be found in [164] and [165].

Kinematic cuts used for electrons identification and preselection are summarized in Table 4-9 following commonly used V+jets group baseline recommendations [163].

Table 4-9. Electron preselection cuts.

Reconstruction Algorithm	=	`PixelMatchGsfElectron`
p_T	$\geq$	10 GeV
$\|\eta\|$	$\leq$	2.5 and not in ECAL gap ($1.47 < \|\eta\| < 1.567$)
ID Type	=	`robustLoose`

4.3.2.3 Jets Reconstruction

Jets are reconstructed using the SisCone algorithm applied to calorimeter towers in which the energy from ECAL and HCAL are added together. A cone of size $R = 0.5$ in η, ϕ space around an input tower seed of at least 0.5 GeV is used to define a "proto-jet". Correction algorithm was applied to reconstructed jets. Preselection cuts for jets are summarized in Table 4-10 following commonly used V+jets baseline cuts.

Table 4-10. Jet preselection cuts.

Reconstruction Algorithm	=	`sisCone5CaloJets`
E_T	$\geq$	30 GeV
$\|\eta\|$	$\leq$	2.5
Hadronic Energy Fraction	$\geq$	0.1

4.3.2.4 Missing Transverse Energy

The Missing Transverse Energy (MET, $\not{E}_T$) of each event is constructed by taking the negative of the vector sum over all calorimeter towers projected in the plane transverse to the beam axis and is a measure of the momentum imbalance of the event from long-lived particles escaping detection in the calorimeters, such as neutrinos, muons, or the lightest supersymmetric particle (LSP). Indeed, the missing transverse energy of the event is one of the most powerful discriminators for R-parity conserving SUSY models. This work uses one of the standard missing transverse energy objects known as “caloMET” corrected for muons if any present in the event.

4.4 Discriminating Observables

Signal and background can be disentangled using a series of cuts on observables that carry some discrimination power. These observables include the three leading jet transverse energies and pseudo-rapidities, the isolation of leading and next-to-leading lepton in the same-charge pair and the missing transverse energy. All plots in this section compare discriminating variables of the SUSY LM0 and $t\bar{t}$ samples, which is the main background as will be shown below.

4.4.1 Two Same-charge Isolated Leptons

Prompt leptons from SUSY processes have different distributions depending on the input SUSY parameters used for sample simulation. We don’t know which phase space (if any) in SUSY parameters is chosen by Nature. Therefore one of a broad approach is to use as low as possible cuts on the lepton transverse momentum. The CMS detector has good reconstruction ability for muons with p_T as low as 5 GeV and electrons with p_T as low as 10 GeV. The transverse momentum distributions for leading muons and electrons in SUSY LM0 and $t\bar{t}$ samples are shown in Figure 4-4. Due to the somewhat soft SUSY lepton spectrum, the lepton transverse momentum is seen to behave rather similarly to the background (though the leading lepton p_T is perhaps mildly harder than the backgrounds).

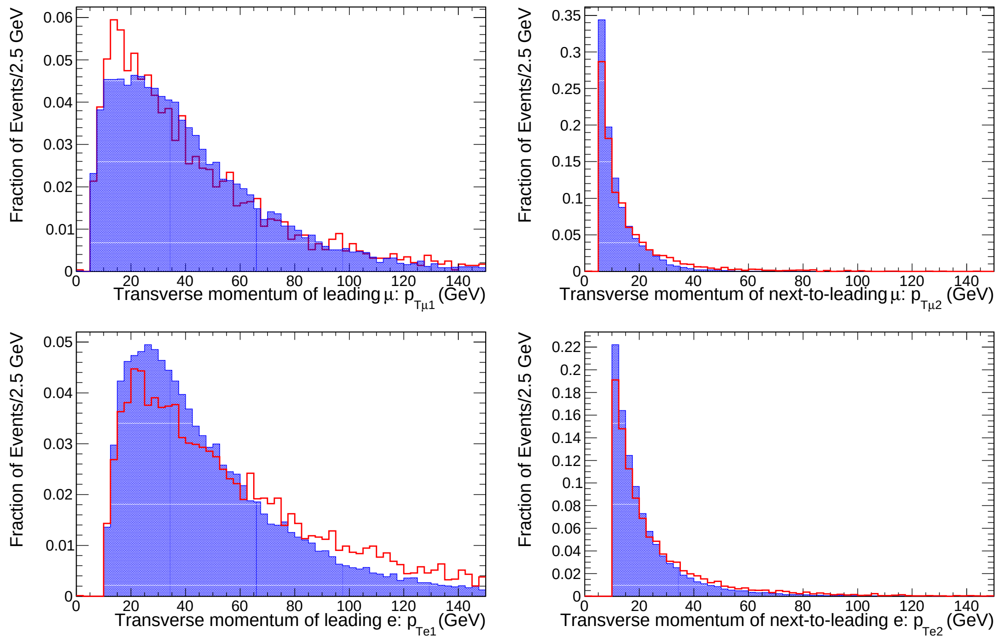

Figure 4-4. Transverse momentum of reconstructed leading (top left) and next-to-leading (top right) muons in same-charge di-muon channel and transverse momentum of reconstructed leading (bottom left) and next-to-leading (bottom right) electrons in same-charge di-electron channel for SUSY LM0 (empty red histogram) and $t\bar{t}$ (shaded blue histogram) samples.

As part of the reconstruction process for leptons, a very important variable, isolation, is calculated. The tracker isolation quantity ($IsoTk_{\mu,0<R\leq 0.3}$) for muons defined by forming the sum of the transverse momenta of all tracks found within a cone of size R = 0.3 around the muon direction, excluding the track of the muon. Calorimeter isolation variables ($IsoEcal_{\mu,0.07<R\leq 0.3}$ and $isoHcal_{\mu,0.07<R\leq 0.3}$) for muons are defined by summing the energies of all calotowers within a cone of size R = 0.3 around the muon direction. The energy deposited in the veto cone of size R = 0.07 around the muon track is excluded. Using these isolation variables a combined relative isolation for muons with respect to the transverse momentum $p_T\mu$ is defined as following

$$RelIso_{\mu} = \frac{IsoTk_{\mu,0<R\leq 0.3} + IsoEcal_{\mu,0.07<R\leq 0.3} + isoHcal_{\mu,0.07<R\leq 0.3}}{p_{T\mu}}.$$

The similar variable is constructed for electrons. The tracker isolation quantity ($IsoTk_{e,0.015<R\leq0.3}$) for electrons is defined by forming the sum of the transverse momenta of all tracks found within a cone of size R = 0.3 around the electron direction, excluding the track of the electron. Also a veto cone of size R = 0.015 is used for the electron's footprint removal. The isolation variable in the electromagnetic calorimeter ($IsoEcal_{e,Jurassic,R\leq0.4}$) is defined by summing the RecHits within a cone of $R = 0.4$ centered on the electron supercluster in the electromagnetic calorimeter with footprint removal region consisting of a strip of specified η width ($\Delta\eta$ = 0.04) and an additional circular region, inner veto cone with R = 0.045 in barrel and R = 0.07 in endcap. This footprint removal technique is called "Jurassic".The isolation variable in the hadron calorimeter ($IsoHcal_{e,R\leq0.4}$) is defined by summing calotowers in a cone of size R = 0.4 centered on the electron supercluster in the electromagnetic calorimeter. No inner veto cone is applied. Using these isolation variables a combined relative isolation for electrons with respect to the transverse momentum $p_T e$ is defined as following

$$RelIso_e = \frac{IsoTk_{e,0.015<R\leq0.3} + IsoEcal_{e,Jurassic,R\leq0.4} + isoHcal_{e,R\leq0.4}}{p_{Te}}.$$

Both prompt leptons in same-charge pairs in SUSY processes are expected to be isolated. On the other hand, because leptons from hadron decays are expected to arise from inside jets, they are expected to be non-isolated. The distributions of relative isolations for most isolated lepton and least isolated lepton in same-charge pairs for SUSY LM0 and $t\bar{t}$ samples are shown in Figure 4-5.

Note, both leptons in same-charge pairs for SUSY sample are isolated. On the contrary, the least isolated lepton in same-charge pairs for $t\bar{t}$ production is expected to come from b-jet and is not isolated. This is clearly seen in Figure 4-5 (right).

4.4.2 High E_T Jets and Their Multiplicity

Due to cascade decades of SUSY particles (dominantly squarks and gluinos), a large number of jets per event is expected. It is shown in Figure 4-6 (top left) that jet

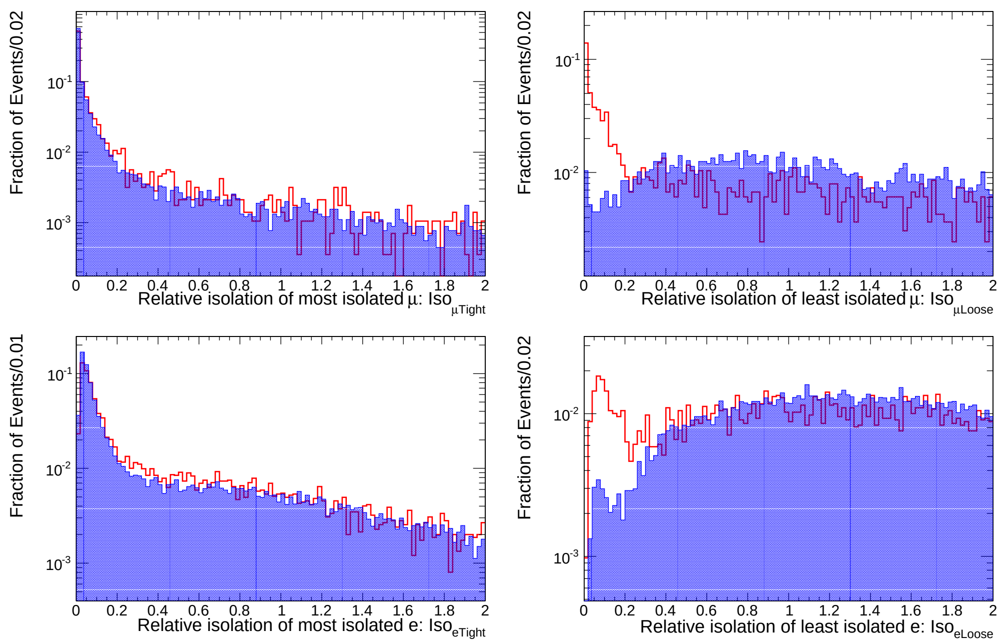

Figure 4-5. Relative isolation of reconstructed most isolated (left top) and least isolated (right top) muons in same-charge di-muon channel and relative isolation of reconstructed most isolated (left top) and least isolated (right top) electrons in same-charge di-electron channel for SUSY LM0 (empty red histogram) and $t\bar{t}$ (shaded blue histogram) samples.

multiplicity for SUSY LM0 sample is higher than for $t\bar{t}$ sample. Depending on the phase space (if any) in SUSY parameters the transverse energy of jets can vary although quite a large area of SUSY parameters yields high E_T jets. For example, the SUSY LM0 benchmark point used for optimization in the analysis has moderately high E_T jets in comparison to jets from $t\bar{t}$ sample as shown in Figure 4-6.

4.4.3 Missing Transverse Energy

Due to the LSP escaping detection, there is a large missing E_T excess for signal events compared with background; indeed, the missing E_T is one of the most powerful discriminators of R-parity conserving SUSY. The MET distribution in SUSY LM0 and $t\bar{t}$ samples are shown in Figure 4-7.

4.4.4 Optimization Procedure

The strategy of optimization is to find a set of selection cuts that maximize the significance with which the null hypothesis (only standard model backgrounds) can be

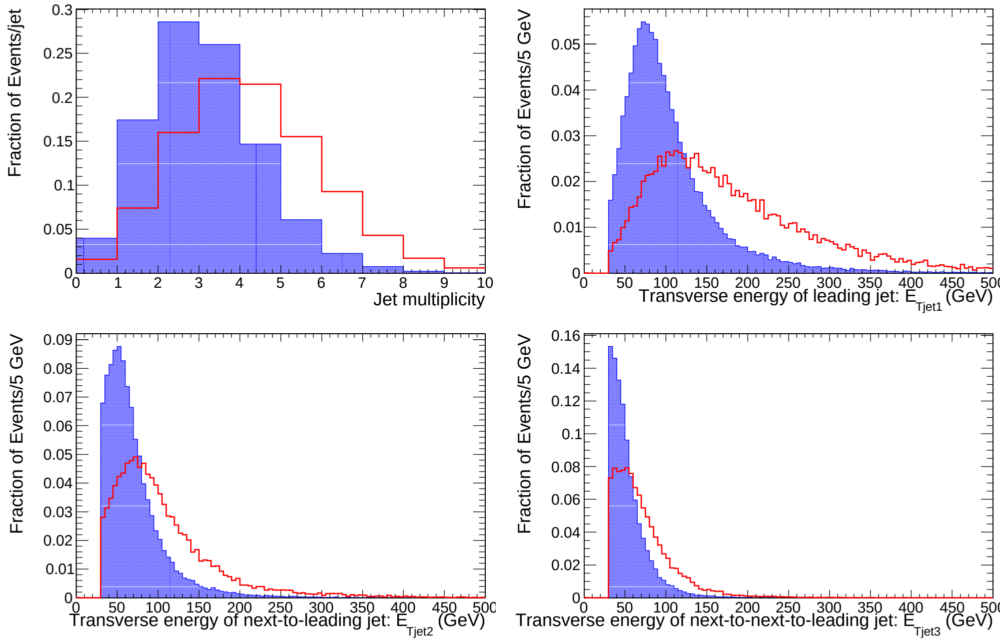

Figure 4-6. Number of jets (top left) and E_T of leading (top right), next-to-leading (bottom left) and next-to-next-to-leading (bottom right) jets for SUSY LM0 (empty red histogram) and $t\bar{t}$ (shaded blue histogram) samples.

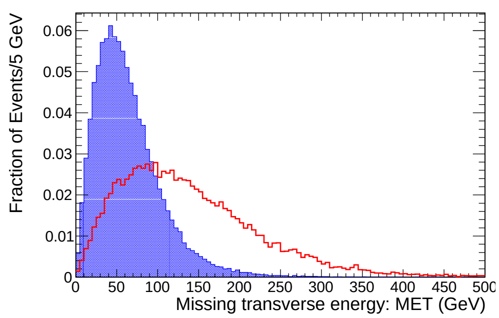

Figure 4-7. Missing transverse energy for SUSY LM0 (empty red histogram) and $t\bar{t}$ (shaded blue histogram) samples.

excluded when signal is present. Different signatures ($\mu\mu$, *ee* and *e*μ) were optimized separately.

A genetic algorithm tool, GARCON [166], is used to search a multi-dimensional space of cuts, with the aim of maximizing the significance of a potential discovery. The optimization is performed using the robust statistical estimate of the significance *S* described in Sec. A.

Table 4-11. Optimized selection cuts for all same-charge di-lepton channels.

Same-charge $\mu\mu$ channel			
Missing transverse energy:	$\not{E}_T$	$\geq$	100 GeV
Transverse energy of leading (1^{st}) jet:	E_{Tjet1}	$\geq$	60 GeV
Transverse energy of next-to-leading (2^{nd}) jet:	E_{Tjet2}	$\geq$	60 GeV
Transverse energy of next-to-next-to-leading (3^{rd}) jet:	E_{Tjet3}	$\geq$	35 GeV
Relative isolation of most isolated μ:	$Iso_{\mu Tight}$	$\leq$	0.175
Relative isolation of least isolated μ:	$Iso_{\mu Loose}$	$\leq$	0.175
Same-charge $e\mu$ channel			
Missing transverse energy:	$\not{E}_T$	$\geq$	110 GeV
Transverse energy of leading (1^{st}) jet:	E_{Tjet1}	$\geq$	85 GeV
Transverse energy of next-to-leading (2^{nd}) jet:	E_{Tjet2}	$\geq$	65 GeV
Transverse energy of next-to-next-to-leading (3^{rd}) jet:	E_{Tjet3}	$\geq$	35 GeV
Relative isolation of μ:	Iso_{μ}	$\leq$	0.08
Relative isolation of e:	Iso_{e}	$\leq$	0.17
Same-charge ee channel			
Missing transverse energy:	$\not{E}_T$	$\geq$	85 GeV
Transverse energy of leading (1^{st}) jet:	E_{Tjet1}	$\geq$	75 GeV
Transverse energy of next-to-leading (2^{nd}) jet:	E_{Tjet2}	$\geq$	75 GeV
Transverse energy of next-to-next-to-leading (3^{rd}) jet:	E_{Tjet3}	$\geq$	35 GeV
Relative isolation of most isolated e:	Iso_{eTight}	$\leq$	0.24
Relative isolation of least isolated e:	Iso_{eLoose}	$\leq$	0.24

4.4.5 Stability of sensitivity

Cut on transverse energy of next-to-next-to-leading (3rd) jet is close to threshold, so we studied dependence of 3rd jet requirement w.r.t. threshold of the jet transverse energy $E_T jet3$. It is shown in Figure 4-8 that significance of cuts are stable for broad region of cuts on the jet transverse energy.

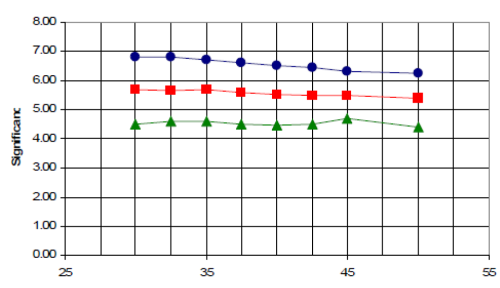

Figure 4-8. Significance vs. cut on E_T of 3rd jet.

Table 4-12. Number of events (at LHC energy $\sqrt{s}$ = 10 TeV and normalized to an integrated luminosity of 100 pb^{-1}) for all SM backgrounds and SUSY LM0 sample after sequentially applying the final set of cuts for all same-charge di-lepton channels.

	QCD ($b\bar{b}$)	Single *W*	Single *Z*	*WW*	*WZ*	*ZZ*	$t\bar{t}$	Total Bkgd.	SUSY LM0
No cuts	$46{\cdot}10^6$	$4.3{\cdot}10^6$	$0.4{\cdot}10^6$	7140	3140	990	41500	$51{\cdot}10^6$	16601
$\mu\mu$ channel									
Same-charge $\mu\mu$	24235	470	197	3.2	11	2.8	418	25337	244
MET	10	15	1.0	0.17	0.66	0.074	66	93	140
1^{st} jet E_T	10	13	1.0	0.17	0.24	0.045	60	85	137
2^{nd} jet E_T	7	6.4	0	0.10	0.10	0	33	47	115
3^{rd} jet E_T	6.4	4.6	0	0.035	0.064	0	26	37	104
Iso_{Tight} μ	0.072	4.6	0	0.035	0.051	0	21	26	76
Iso_{Loose} μ	0	0	0	0	0.025	0	0.48	0.51	20
Di-μ HLT	0	0	0	0	0.025	0	0.39	0.42	19
Skim	0	0	0	0	0.025	0	0.39	0.42	19
$e\mu$ channel									
Same-charge $e\mu$	90435	3828	1325	35	30	8.6	1408	97070	791
MET	27	130	7.7	2.5	1.5	0.15	173	342	446
1^{st} jet E_T	18	50	4.0	0.91	0.78	0.059	121	195	401
2^{nd} jet E_T	7.7	17	0.67	0.42	0.23	0.020	70	96	309
3^{rd} jet E_T	4.3	10	0	0.17	0.09	0.010	53	67	269
Iso μ	0.068	5.5	0	0.10	0.064	0.005	21	27	105
Iso e	0	0	0	0	0.013	0	0.26	0.28	22
Skim	0	0	0	0	0.013	0	0.26	0.28	22
***ee* channel**									
Same-charge *ee*	64648	2759	3154	36	24	8.0	1137	71767	668
MET	206	261	7.7	5.5	2.4	0.35	268	750	482
1^{st} jet E_T	92	86	3.3	2.4	1.04	0.12	188	373	432
2^{nd} jet E_T	28	19	1.3	0.31	0.22	0.045	75	124	271
3^{rd} jet E_T	17	11	0.67	0.21	0.10	0.035	54	84	230
Iso_{Tight} *e*	0.28	8.2	0.67	0.17	0.089	0.010	33	42	110
Iso_{Loose} *e*	0.0036	0	0	0	0.013	0.010	0.48	0.51	15
Di-*e* HLT	0	0	0	0	0.013	0.010	0.44	0.46	14
Skim	0	0	0	0	0.013	0.010	0.44	0.46	14

4.5 Data Driven Methods and Systematic uncertainties

4.5.1 Same-charge Di-muon Channel

4.5.1.1 Data Driven Method to Estimate the QCD Background

The QCD background contribution to the same-charge di-lepton signature is expected to be reduced to zero by imposing both a tight isolation requirement on the leptons and a high cut on the MET, as well as requiring the existence of a third high E_T jet in the event. Nonetheless, due to the large QCD multi-jet cross-section and the inherent uncertainty we have to its true value, a data-driven method has been developed to extract an upper bound on the QCD background contribution directly from data [167, 168].

The method relies on the expected factorization of the isolation cuts from the hadronic cuts at the analysis level (i.e., the cuts are uncorrelated). In order for the method to work, the isolation and hadronic cuts have to be designed such that QCD is expected to dominate the event yields before and after each one of them is applied irrespective of the other. If the this is true, then the resulting cut efficiencies derived in the data can be taken to be the QCD cut efficiencies. The product of these efficiencies should provide an upper bound on the total QCD yield after all cuts are applied. Only an upper bound can be obtained due to the small, but non-negligible, contributions from other SM backgrounds (e.g. $t\bar{t}$) or signal.

This method has been tested in Monte Carlo for the case with signal (LM0) and without signal. The results indicate that an upper bound on the QCD contribution can be placed at 0.12 ± 0.01 events for the case without signal, assuming a 100 pb^{-1} scenario.

The complete description of this method can be found elsewhere [167, 168] and has so far been demonstrated to be feasible only for the di-muon final state. Similar studies for the electron-muon and di-electron final state will be completed in the near future.

4.5.1.2 Data Driven Method to Estimate Top ($t\bar{t}$) and Single Boson (W/Z+jets) Backgrounds

In $t\bar{t}$ or W/Z+jets samples, events that have two same-charge leptons are expected to contain only one isolated lepton. Second lepton is originated from hadron decays (mostly b-jets) and expected to be non-isolated. In contrast, both leptons of same-charge in SUSY events are expected to be isolated and they give rise to number of events counted in the lowest bin of lepton isolation cut distribution. This feature is proposed to be used for data driven estimation of $t\bar{t}$ and W/Z+jets contribution into signal region of isolated leptons.

Due to the relatively low cross section of $t\bar{t}$ production at LHC, it is proposed to use an isolation template for muons obtained using QCD events with *b*-jet and muon in opposite hemispheres. The isolation template is shown in Figure 4-9. For comparison the muon isolation from $t\bar{t}$ is also shown and they are in reasonable agreement.

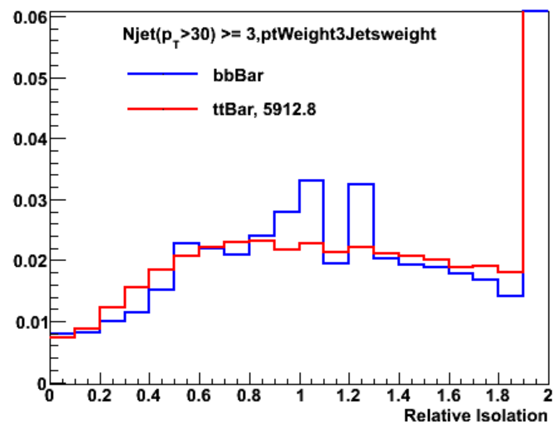

Figure 4-9. The isolation template for muons from QCD (blue line). The isolation distribution for muons from $t\bar{t}$ is shown for comparison (red line).

The complete description of this method can be found elsewhere [169, 170] and has so far been demonstrated to be feasible only for the di-muon final state.

4.5.2 Same-charge Di-electron and Electron-Muon Channels

The major background for Di-electron and Electron-Muon channels is due to misidentification of the charge of an electron. There is a data driven method focuses on estimating the charge mis-id probability for electrons as a function of p_T and η. Di-electrons coming in Z-decay kinematic region are separated into same-sign and opposite sign groups (and also into barrel and endcap region groups). All events with same-sign di-electrons in such events are expected to have one electron with mis-measured charge. Details of the method can be found in the following report [171].

4.5.3 Systematic uncertainties

Table 4-13 lists systematic uncertainties for signal. Rough estimates of the levels of the uncertainties were taken from [104]. For completeness uncertainty on missing transverse energy was added to the list. Conservatively we are using the same estimation of systematic uncertainties for background. Total systematic uncertainties of the analysis are $\approx$ 30% and for now assumed that they are the same for all channels.

Table 4-13. Summary of systematic uncertainties for SUSY signal included in the analysis.

$\delta\sigma/\sigma_{LM0}$	15%
$\delta L/L$	10%
$\delta\epsilon/\epsilon_{RECO}$	2%
$\delta\epsilon/\epsilon_{pTcut}$	negligible
$\delta\epsilon/\epsilon_{isolation(isol)}$	negligible
$\delta\epsilon/\epsilon_{isolation(non-isol)}$	negligible
$\delta\epsilon/\epsilon_{scalejets}$	15%
$\delta\epsilon/\epsilon_{resolutionjets}$	10%
$\delta\epsilon/\epsilon_{MET}$	10%
total	27.5%

In the next update of the analysis the systematic uncertainties will be better evaluated. To reduce impact of systematic uncertainties on the final results the data driven methods to estimate backgrounds will be used as described in Sec. 4.5.1.2 and Sec. 4.5.1.1.

4.6 Results for $\sqrt{s}$ = 10 TeV

Fast simulated SUSY samples at $\sqrt{s}$ = 10 TeV were used to find reach contours and exclusion limits in mSUGRA parameter space. The total number of expected SM background events at this energy is 1.16 (see Table 4-14).

Figure 4-10 (top) shows the $5\,\sigma$ reach contours of all signatures of this analysis (with and without 30% systematic uncertainties) in the mSUGRA $m_0 - m_{1/2}$ plane, assuming L =100 pb^{-1} for $\sqrt{s}$ = 10 TeV.

Figure 4-10 (bottom) shows the CL=95% exclusion limits of all signatures of this analysis (with and without 30% systematic uncertainties) in the mSUGRA $m_0 - m_{1/2}$ plane, assuming L =100 pb^{-1} for $\sqrt{s}$ = 10 TeV.

4.7 Results for $\sqrt{s}$ = 7 TeV

Fast simulated SUSY samples at $\sqrt{s}$ = 7 TeV were used to find reach contours and exclusion limits in mSUGRA parameter space. The total number of expected SM

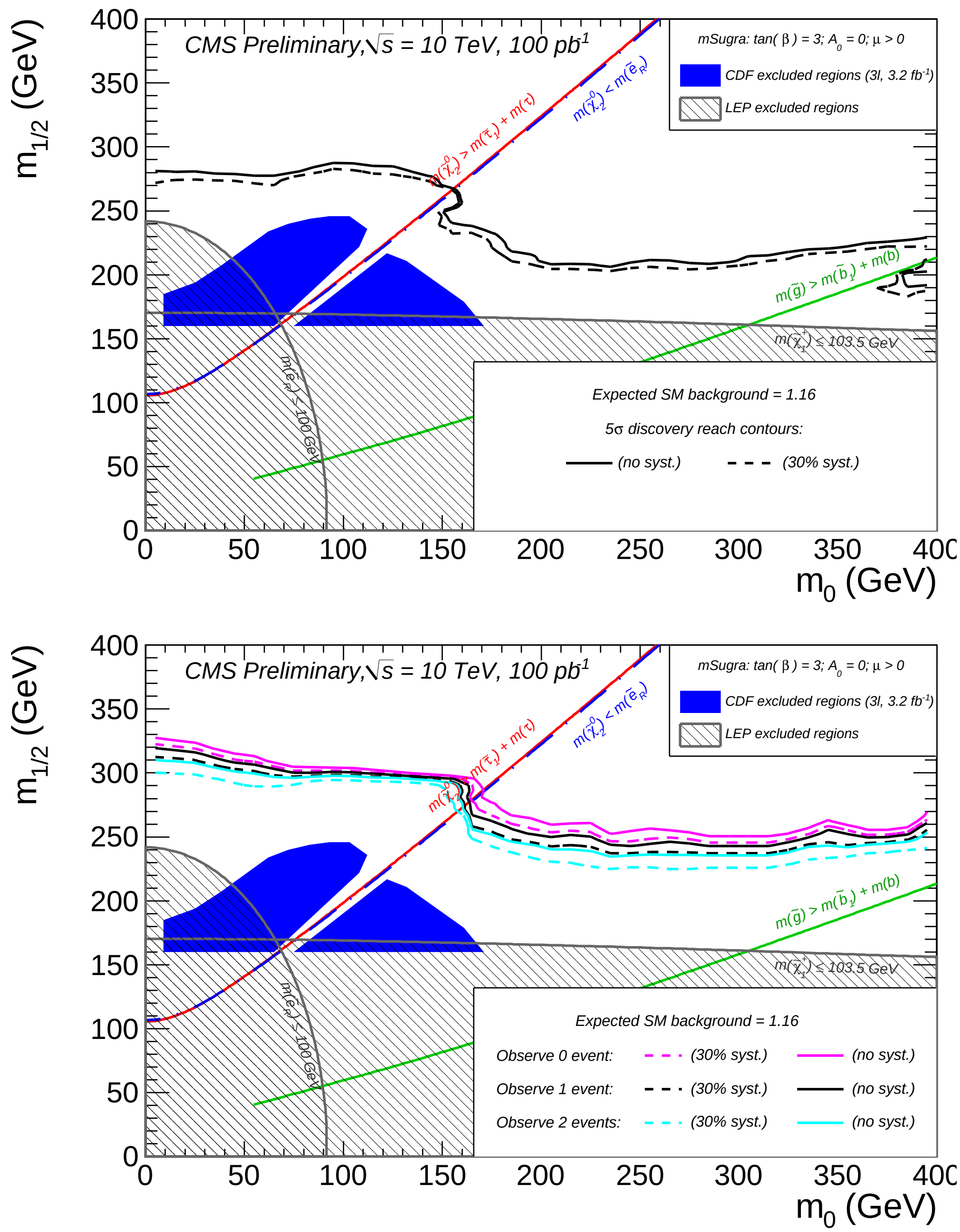

Figure 4-10. Top: the CMS 5σ reach contours at $\sqrt{s}$ = 10 TeV in the $m_0 - m_{1/2}$ plane for SUSY processes involving prompt same-charge di-leptons ($\mu\mu$, $e\mu$ and ee) for L =100 pb^{-1} with 30% systematic uncertainties (dashed line) and without them (solid line). Bottom: the CMS 95%CL exclusion limits at $\sqrt{s}$ = 10 TeV in the $m_0 - m_{1/2}$ plane for SUSY processes involving prompt same-charge di-leptons ($\mu\mu$, $e\mu$ and ee) for L =100 pb^{-1} with 30% systematic uncertainties (dashed lines) and without them (solid lines). The other mSUGRA parameters are fixed to tan β=3, μ>0 and A_0=0.

background events at this energy is 0.41. It is obtained applying scale factor to known (see Table 4-14) number of events at $\sqrt{s}$ = 10 TeV after all cuts applied.

Table 4-14. Number of events (at LHC energy $\sqrt{s}$ = 7 TeV and normalized to an integrated luminosity of 100 pb^{-1}) for all SM backgrounds and SUSY LM0 sample after applying the final set of cuts for all same-charge di-lepton channels.

All Cuts	QCD ($b\bar{b}$)	Single W	Single Z	WW	WZ	ZZ	$t\bar{t}$	Total Bkgd.	SUSY LM0
$\mu\mu$ **channel**	0	0	0	0	0.015	0	0.16	0.17	6.6
$e\mu$ **channel**	0	0	0	0	0.007	0	0.09	0.09	7.6
ee **channel**	0	0	0	0	0.007	0.006	0.14	0.15	4.9

Figure 4-11 (top) shows the 5 σ reach contours of all signatures of this analysis (with and without systematic uncertainties) in the mSUGRA $m_0 - m_{1/2}$ plane, assuming L =100 pb^{-1} for $\sqrt{s}$ = 7 TeV.

Figure 4-11 (bottom) shows the CL=95% exclusion limits of all signatures of this analysis (with and without systematic uncertainties) in the mSUGRA $m_0 - m_{1/2}$ plane, assuming L =100 pb^{-1} for $\sqrt{s}$ = 7 TeV.

The obtained exclusion limits are in good agreement with [172] taking into account the difference in applied cuts and usage of k-factors for SUSY samples in the analysis.

4.8 Conclusion

This work shows that, using reasonable cuts, SM backgrounds to same-sign di-lepton channels can be suppressed almost to zero at LHC energies

This work shows that, using reasonable cuts, SM backgrounds to same-charge di-lepton channels can be suppressed almost to zero at LHC center of mass energies $\sqrt{s}$ = 7 TeV and $\sqrt{s}$ = 10 TeV. Next-to-leading order cross sections were used for all SM backgrounds and SUSY samples. And the treatment of SM backgrounds includes data driven techniques. In addition di-electron and electron-muon signatures were included which allows to increase sensitivity.

Cuts optimization is done in the assumption of initial low-luminosity running. The optimized cuts are used to scan across (m_0, $m_{1/2}$) plane of mSUGRA. Projected

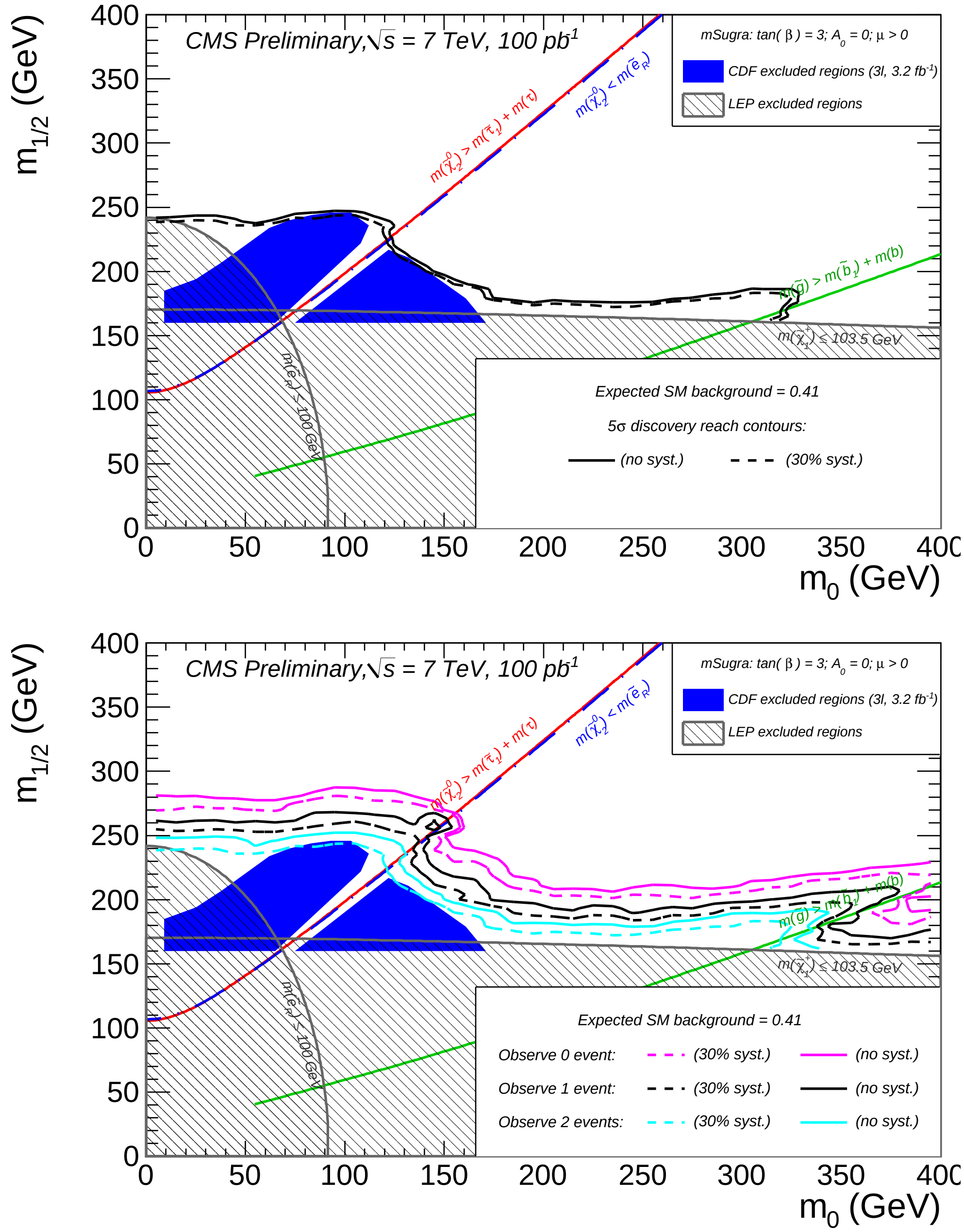

Figure 4-11. Top: the CMS 5σ reach contours at $\sqrt{s}$ = 7 TeV in the $m_0 - m_{1/2}$ plane for SUSY processes involving prompt same-charge di-leptons ($\mu\mu$, $e\mu$ and ee) for L =100 pb^{-1} with 30% systematic uncertainties (dashed line) and without them (solid line). Bottom: the CMS 95%CL exclusion limits at $\sqrt{s}$ = 7 TeV in the $m_0 - m_{1/2}$ plane for SUSY processes involving prompt same-charge di-leptons ($\mu\mu$, $e\mu$ and ee) for L =100 pb^{-1} with 30% systematic uncertainties (dashed lines) and without them (solid lines). The other mSUGRA parameters are fixed to tan $\beta = 3$, $\mu > 0$ and $A_0 = 0$.

exclusion limits together with 5σ discovery contours are reported for 100 pb^{-1} of integrated luminosity at LHC energies $\sqrt{s}$ = 7 TeV and $\sqrt{s}$ = 10 TeV. The results indicate that the low mass region of mSUGRA can be probed at $\sqrt{s}$ = 7 TeV with integrated luminosity 100 pb^{-1} exceeding current Tevatron sensitivity.

CHAPTER 5
EFFICIENCY OF FINDING MUON TRACK TRIGGER PRIMITIVES IN CMS CATHODE STRIP CHAMBERS

5.1 Introduction

In the CMS Experiment, muon detection in the forward direction is accomplished by cathode strip chambers (CSC). These detectors identify muons, provide a fast muon trigger, and give a precise measurement of the muon trajectory. There are 468 six-plane CSCs in the system. The efficiency of finding muon trigger primitives (muon track segments) was studied using 36 CMS CSCs and cosmic ray muons during the Magnet Test and Cosmic Challenge (MTCC) exercise conducted by the CMS experiment in 2006. In contrast to earlier studies that used muon beams to illuminate a very small chamber area (< 0.01 m^2), results presented in this chapter were obtained by many installed CSCs operating in situ over an area of $\approx$ 23 m^2 as a part of the CMS experiment. The efficiency of finding 2-dimensional trigger primitives within 6-layer chambers was found to be 99.93 $\pm$ 0.03%. These segments, found by the CSC electronics within 800 ns after the passing of a muon through the chambers, are the input information for the Level-1 muon trigger and, also, are a necessary condition for chambers to be read out by the Data Acquisition System. The results of this work have been published in [173].

In later CMS studies [174] with cosmic ray muons using all CSCs during the Cosmic Run at Four Tesla (CRAFT) in 2008 the results of this work were used as a benchmark.

5.2 Local Charged Tracks

The CSC electronics is capable of very fast (800 ns) identification of patterns of hits in 6 chamber layers compatible with a high p_{T} muon originating from the interaction point. The fast pattern recognition is performed by Field Programmable Gate Array (FPGA) chips. The found patterns, known as Local Charged Tracks (LCT), are primitives for the Level-1 muon trigger [157]. They are also a necessary condition for reading out CSC data, i.e., CSC data are present in the Data Acquisition System (DAQ) stream for High-Level trigger or offline analyses only when LCTs have been found in that chamber.

Anode Local Charged Track patterns (ALCT) are formed from wire group hits. At every bunch crossing (25 ns), the FPGA firmware checks if anode hits in 6 planes of a chamber form patterns consistent with muon tracks originating from the interaction point. The set of wire group hits among the 6 layers from which ALCTs can be created form a bow-tie-shaped envelope (Figure 5-1). Desired ALCT patterns can be programmed individually within the boundary of this envelope. We used the default patterns fully spanning the envelope, which provides the widest acceptance. The third CSC layer is called the key-layer: for each wire group in the key-layer, the firmware seeks anode hits that lie within ALCT patterns keyed to that wire group. For a pattern to be valid, hits from at least 4 planes are required to be present in the pattern including the key-layer. Out of all ALCTs that may be present in a chamber, the electronics reports only the 2 best-quality ones per each bunch crossing, ALCT0 and ALCT1. This is adequate for the expected chamber track occupancy at the nominal LHC luminosity. The pattern quality depends on the number of planes present in a pattern and its *y* coordinate. The reported patterns have tags identifying the key wire groups they are associated with (marked as "$\times$" in Figure 5-1).

Similarly, Cathode Local Charged Track patterns (CLCT) are searched for among comparator half-strip hits. Unlike the case of ALCTs, there are 7 CLCT patterns. These patterns are shown in Figure 5-2: the straight-through pattern corresponds to high p_T muons ($p_T > 30$ GeV), while more inclined patterns would detect softer muons. For a pattern to be valid, hits from at least 4 planes are required to be present in the pattern. In addition, 4 adjacent half-strip comparator bits are combined to form 1 di-strip bit. The electronics also checks for presence of patterns made of di-strips, which allows one to choose and trigger on highly inclined, i.e., low p_T, muons. The CLCT-searching firmware reports the 2 best-quality CLCTs per bunch crossing, CLCT0 and CLCT1. The pattern quality depends on the number of planes present, whether the pattern is based on half-strips or di-strips, and the inclination of the pattern. The reported patterns have tags identifying the key half-strip number with which they are associated. In the future, the number of half-strip patterns will be increased to cover the full angular range, and di-strip-based patterns will no longer be used.

ALCTs and CLCTs are paired to form 2-dimensional LCTs. Out of all possible pairs considered, the two highest-quality LCTs in each CSC are transmitted further downstream. These LCTs are used as input primitives for searching for and forming full muon tracks by the Level-1 muon trigger.

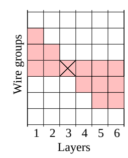

Figure 5-1. Wire groups bit pattern used for constructing ALCTs. The key wire group is marked with a cross.

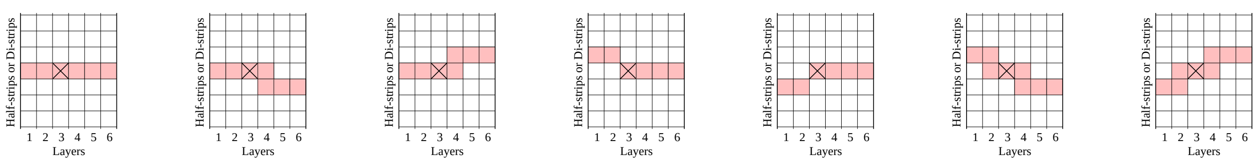

Figure 5-2. Comparator bit patterns used for constructing CLCTs. The key half/di-strip is marked with a cross. The straight-through pattern (left) corresponds to high p_T muons, while more inclined patterns would detect softer muons.

5.3 Magnet Test and Cosmic Challenge Setup

In the second half of 2006, during the Magnet Test and Cosmic Challenge (MTCC) [139] exercise, a substantial part of the CMS detector operated as one system. The MTCC exercise took place above ground (i.e. not in the experimental hall cavern). The Endcap Muon System was represented by a 60° sector of the ME+ endcap. Figure 5-3 shows the layout of chambers that were present in the MTCC in the global CMS coordinate system. A total of 36 chambers were operational during these tests. The data used in this analysis were taken with the magnetic field turned off.

To perform an unbiased measurement of the CSC efficiency for finding muon trigger primitives, we ran the CMS detector Data Acquisition with a Level-1 trigger based on the ME+1 and ME+3 chambers. The ME+2 chambers were not used in the trigger, but were present in the readout whenever an LCT in these chambers was found in coincidence with the Level-1 trigger. It is these ME+2 chambers that we used to measure the efficiency.

The overall area available for studying the LCT-finding efficiency was about 23 m^2. This is an area far larger than what was available in the earlier beam tests studies [157, 175], which, by necessity, were always limited to very small chamber areas, typically of the order of or less than 10 $\times$ 10 cm^2.

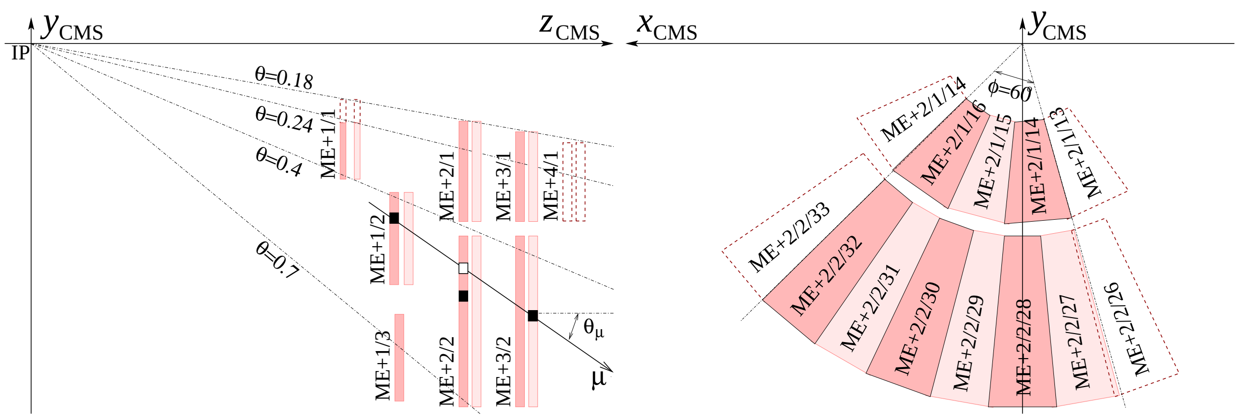

Figure 5-3. CSCs that took data during the MTCC. Highlighted chambers were operational during the MTCC. Left: Side view. The solid boxes schematically show the locations of ALCTs that were actually found for a muon in 3 chambers. The open box indicates the predicted ALCT position in the ME+2 station for this muon based on the measurements in ME+1 and ME+3. Right: Transverse view of the ME+2 station.

An example of typical event considered in the analysis is shown in Figure 5-4. Visualization of this event was performed by the Interactive Graphics for User Analysis (IGUANA) system [176]. Wire and strip hits in 3 chambers (ME+1/2/30, ME+2/2/30, and ME+3/2/30) are represented.

5.4 Offline Event Selection

To eliminate ambiguities in predicting the muon track position in the middle ME+2 chamber, we required one and only one Track Segment (TS) among all ME+1 chambers and one and only one track segment among all ME+3 chambers. Track segments were identified using the simple algorithm described in Appendix. It allowed us, using information only from the ME+1 and ME+3 chambers, to predict muon track positions in the ME+2 chambers with a few millimeter precision in both the x and y directions. The prediction accuracy was mostly driven by the multiple scattering of cosmic ray muons in the EMU steel disks (see Figure 3-10). Since we used runs taken with the magnetic field turned off, the muon track was assumed to be a straight line going through the 2 space-points assigned to the ME+1 and ME+3 track segments.

The ALCT- and CLCT-finding electronics are designed to have high efficiency for muons originating from the Interaction Point (IP). We selected events where the predicted track direction would resemble “IP-like” muons. This was achieved by selecting events in which the local polar angle of the track θ_μ (see Figure 5-3) predicted from track segments in the ME+1 and ME+3 stations was within 0–1 rad. In addition, the ϕ_n-number of the chambers with track segments in the ME+1 and ME+3 stations had to be the same (e.g., ME+1/3/27 and ME+3/2/27). Note that the quotes in “IP-like” are essential: we did not actually require selected muons to point back exactly to the IP; if we had, we would have had a very small event sample to work with.

Events in which the predicted tracks would miss the geometrical area of the ME+2 chambers (limited in the r-ϕ plane by upper and lower distances from the beam line as well as minimum and maximum azimuthal angles) were excluded from the analysis.

After these cuts, we ended up with 759 tracks going through ME+2/1 chambers and 14 100 tracks going through ME+2/2 chambers. There are fewer tracks through the ME+2/1 chambers because they are smaller in size and, more importantly, require more horizontal muons, which are sparse in cosmic rays. The predicted track positions in the key-layer of the ME+2/1 and ME+2/2 chambers are shown in Figure 5-5.

The chamber wire planes are not contiguous from the narrow end to the wide end. There are 2 or 4 breaks of 25 mm width at approximately every 60 cm, which create 3 or 5 independent high voltage segments per plane. These break points are also used to introduce panel supports, without which the panels would bulge or cave in and stable chamber operation would not be possible. These break points, indicated by dashed lines in Figure 5-5, result in dead zones. These dead zones line up horizontally and mostly effect tracks with smaller θ_μ-angle.

5.5 Efficiency Measurement

For an event to be counted as efficient, we required at least one ALCT and at least one CLCT (i.e., at least one 2d-LCT) to be reported by the ME+2 chamber through which the predicted muon should have gone.

Although we do expect some loss of efficiency near chamber edges and between high voltage segments, we first obtained the chamber LCT-finding efficiencies without any fiducial cuts. The corresponding results (the number of events with predicted tracks going through ME+2 chambers, the number of events for which a 2d-LCT was not reported by the ME+2 chambers, and the corresponding efficiencies) are given in Table 5-1. The average efficiency, without any fiducial cuts, was around 97%–98%.

Figure 5-6 shows only those predicted track positions in the ME+2/1 and ME+2/2 chambers when no 2d-LCT were reported. One can clearly see the clustering occurring around the chamber geometrical dead zones.

The efficiency depends on the local polar angle θ_μ of a muon's track as shown in Figure 5-7 (left). One can see that the efficiency decreases for smaller angle tracks. To loose an LCT, one needs to loose hits in 3 or more planes. A straightforward geometric analysis of how track with different θ_μ-angles cross the dead areas between high voltage segments results in the curve also shown in the figure. Although the curve

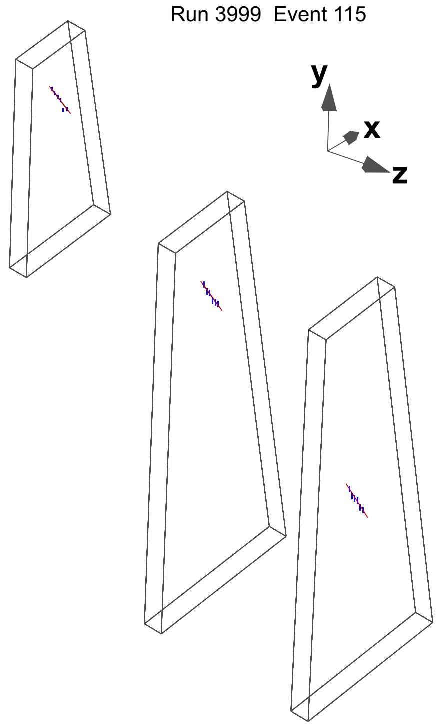

Figure 5-4. Screen shot of the interactive IGUANA-based event display, showing CSCs with strip and wire hits from a cosmic muon that passed through 3 stations of the EMU system.

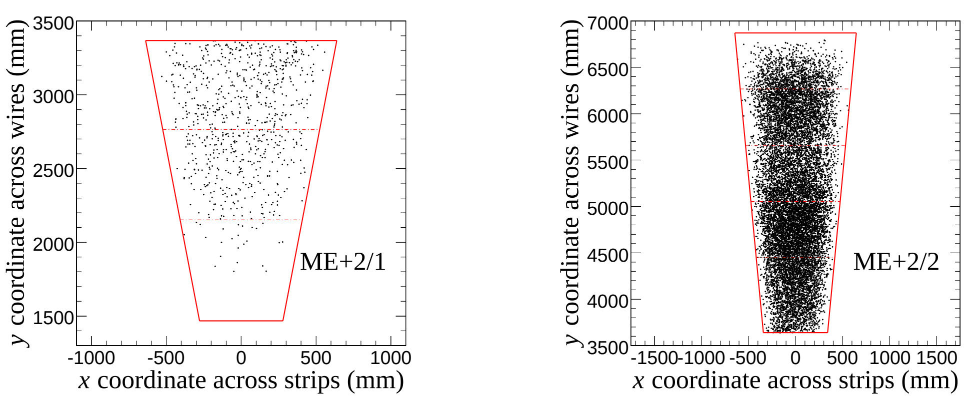

Figure 5-5. Predicted positions of muon hits in ME+2/1 (left) and ME+2/2 (right) chambers.

is somewhat simplistic as it includes neither the single plane detecting inefficiency nor errors in the θ_μ-angle predictions, the data and the curve are in good agreement.

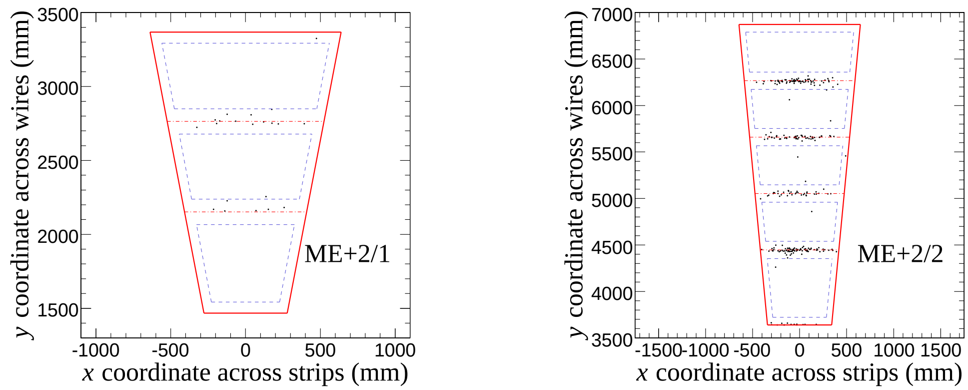

Figure 5-6. Predicted positions of muon hits in ME+2/1 (left) and ME+2/2 (right) chambers when LCTs in ME+2 are lost.

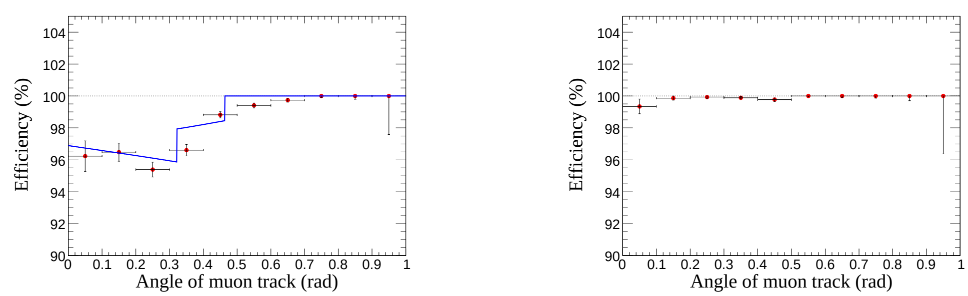

Figure 5-7. Efficiency to report a muon LCT as a function of track angle θ_μ without fiducial cuts (left) and after excluding "semi-dead" zones (right) in ME+2 chambers. The predicted efficiency curve based on geometric analysis is shown as the solid line.

To measure the true CSC efficiency, i.e., excluding geometrical dead zones, we applied fiducial cuts on the predicted tracks to eliminate those that would cross dead zones. The chamber areas with full acceptance are shown in Figure 5-6 as dashed polygons. The borders for these areas were defined so that tracks with our selection of allowed directions would never miss 3 or more planes due to dead zones or chamber edges. These areas were reduced further by 1–1.5 cm to account for the finite precisions, σ_{dx} and σ_{dy}, with which we could predict muon track positions in the ME+2 chambers. These corrections corresponded to $3\sigma_{dx}$ and $3\sigma_{dy}$ (see Appendix for details). After applying such fiducial acceptance cuts on the predicted tracks, only one 2d-LCTs in ME+2/1 and seven 2d-LCTs in ME+2/2 chambers were lost. Upon further examination it was found that the 7 missing muons in ME+2/2 chambers did not appear to be concentrating together in one particular chamber. In 1 of these 8 events, the 2d-LCT was actually in the neighboring chamber, 5 events had neither ALCTs nor CLCTs, and in 2 events an ALCT was reported with no matching CLCT. The CSC efficiency averaged over all chambers used in this study was found to be 99.93 $\pm$ 0.03%. Details are given in Table 5-2. The efficiency dependence of a track angle after applying the fiducial cuts is shown in Figure 5-7 (right). It is greater than 99% for all angles.

To confirm that what we measured is the efficiency to find muon-associated 2d-LCTs (rather than just noise), we plotted the differences between the predicted muon track x and y positions and the actual 2d-LCT0s reported by the ME+2 chambers (Figure 5-8). The positions of the 2d-LCT0s in the ME+2-chambers were defined by the centers of the ALCT0 key wire groups and CLCT0 key half-strips.

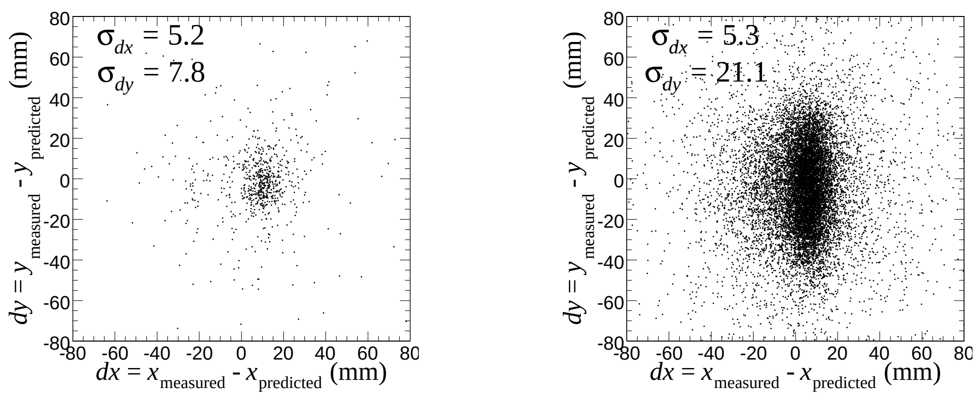

Figure 5-8. Muon hits residuals in ME+2/1 (left) and ME+2/2 (right) chambers.

The LCTs found in the ME+2 chambers are within $\approx$0.5–2 cm around the predicted positions, which is consistent with the expected multiple scattering of cosmic ray muons and the widths of the strips and wire groups. For further discussion, see Appendix. Note that the ME+2/2 chambers are distinguished by a large $\sigma_{dy} \approx$ 2.1 cm. This is because these chambers have much wider wire groups: w = 51 mm vs. 19 mm for

ME2/1. Note that the residuals' sigmas σ_{dy} are about 1.4 larger than one might naively expect, $w/\sqrt{12}$. As shown in the Appendix, the error in predicting a muon position in the ME+2 station from measurements in the ME+1 and ME+3 stations is about 3.5 mm, which cannot account for the observed difference. Thefore, the factor 1.4 reflects the performance of the ALCT pattern finding logic currently implemented in the ALCT board firmware.

5.6 Conclusions

The efficiency of the CMS cathode strip chambers to report muon trigger primitives was measured with cosmic ray muons over an area of $\approx$23 m^2 of installed chambers. The obtained efficiency was 99.93 $\pm$ 0.03%, which exceeds the design specification of 99%.

Table 5-1. Efficiencies to detect muon 2d-LCTs by ME+2 chambers without fiducial cuts. The errors are statistical.

	Number of selected events	Number of events with no 2d-LCT reported	Efficiency to report 2d-LCT
ME+2/1	759	22	97.1 $\pm$ 0.6%
ME+2/2	14100	267	98.1 $\pm$ 0.1%

Table 5-2. Efficiencies to detect muon LCT in ME+2 chambers after excluding "semi-dead" zones.

	Number of triggered events	Number of events with undetected muons	Efficiency to report LCT
ME+2/1	532	1	$99.8^{+0.12}_{-0.33}$%
ME+2/2	9990	7	$99.93^{+0.028}_{-0.033}$%

During the Cosmic Run at Four Tesla (CRAFT) in 2008 the results of this work were used as a benchmark to measure efficiency of all CMS CSCs [174].

APPENDIX A
ESTIMATOR USED FOR SIGNIFICANCE CALCULATION

The systematic uncertainties are incorporated into significance estimator in the following way. The Poisson probability to observe N events, assuming a hypothesis of number of Standard Model background events N_b is,

$$p(N|N_\mathrm{b}) = \frac{N_\mathrm{b}^N}{N!}\exp[-N_\mathrm{b}]. \tag{A–1}$$

The number of predicted background events N_b may be factor k different from the unknown “true” background n_b, due to some systematic uncertainty. Because the prediction for N_b is often close to zero, the number of “true” background events n_b is assumed to have a log-normal distribution about the prediction N_b:

$$f(n_\mathrm{b}|N_\mathrm{b}) = \frac{1}{\sqrt{2\pi}\,\ln k}\exp\left[-\frac{1}{2}\left(\frac{\ln n_\mathrm{b} - \ln N_\mathrm{b}}{\ln k}\right)^2\right]. \tag{A–2}$$

Hence, for a total number of background events N_b, predicted with a systematic uncertainty included as in Eq. A–2, the probability density to observe N events is

$$\phi(N|N_\mathrm{b}) = \int_0^\infty p(N|n_\mathrm{b})f(n_\mathrm{b}|N_\mathrm{b})dn_\mathrm{b}. \tag{A–3}$$

The incompatibility of the signal plus background ($N_\mathrm{s} + N_\mathrm{b}$) with the background-only hypothesis (N_b) is then estimated by converting the one-sided probability tail:

$$P(N_\mathrm{s}, N_\mathrm{b}) = \int_{N_\mathrm{s}+N_\mathrm{b}}^\infty \phi(N|N_\mathrm{b})dN, \tag{A–4}$$

to a Gaussian-equivalent significance S, by solving the equation:

$$\frac{1}{2} - \int_0^S \frac{1}{\sqrt{2\pi}}e^{-\frac{x^2}{2}}dx = P(N_\mathrm{s}, N_\mathrm{b}). \tag{A–5}$$

Because the probability $P(N_\mathrm{s}, N_\mathrm{b})$ is calculated via numerical integration before being converted to a significance, the estimation for S is limited by the numerical precision of the computation. As a result, estimates for S are found to be numerically robust for values up to 37σ.

APPENDIX B
ESTIMATOR USED FOR EXCLUSION LIMITS CALCULATION

Bayes theorem gives a posterior probability on signal strength in terms of ratio r and in assumption of flat prior $\pi(r) = const$:

$$L(r|n_0) = \frac{p(n_0|b_0 + rs_0)\pi(r)}{\int_0^{+\infty} p(n_0|b_0 + rs_0)\pi(r)dr} == \frac{p(n_0|b_0 + rs_0)}{\int_0^{+\infty} p(n_0|b_0 + rs_0)dr},$$

where

$$p(n_0|b_0 + rs_0) = \frac{(b_0 + rs_0)^{n_0}}{n_0!} e^{-(b_0+rs_0)},$$

and b_0 – is expected background, s_0 - expected signal, n_0 – is number of observed events.

Assumption of log-normal probability distribution function of systematic uncertainty k and 100% correlation between signal and background leads to modified formula from above

$$L(r|n_0) = \frac{\left[\int p(n_0|b_0 k^x + rs_0 k^x)g(x)dx\right]\pi(r)}{\int_0^{+\infty}\left[\int p(n_0|b_0 k^x + rs_0 k^x)g(x)dx\right]\pi(r)dr} = \frac{\left[\int p(n_0|b_0 k^x + rs_0 k^x)g(x)dx\right]}{\int_0^{+\infty}\left[\int p(n_0|b_0 k^x + rs_0 k^x)g(x)dx\right]dr},$$

where $g(x)$ is the normal probability distribution function.

Exclusion limit is then observed from equation on r:

$$\int_r^{+\infty} L(r)dr = \alpha,$$

where, for example, $\alpha = 0.05$ for 95% confidence level.

APPENDIX C
THE LM0 MSUGRA BENCHMARK SAMPLE

The mass spectrum of the LM0 mSUGRA benchmark sample is shown in Figure C-1.

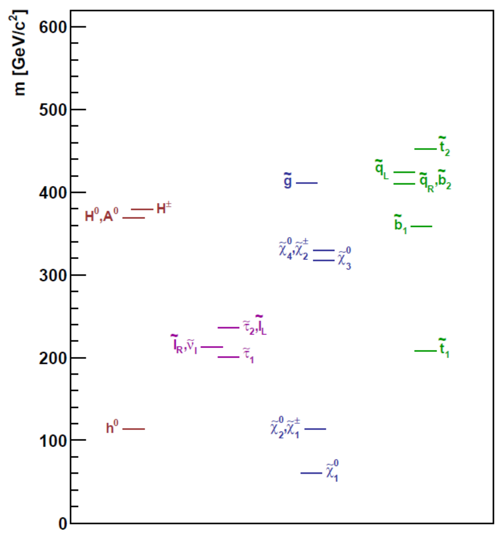

Figure C-1. Mass spectrum of SUSY LM0 benchmark sample [177].

Input file for the LM0 mSUGRA benchmark sample in Les Houches format is shown below.

```
#
#                              =======================
#                              | THE SUSYHIT OUTPUT |
#                              =======================
#
#
#              -----------------------------------------------------
#              |     This is the output of the SUSY-HIT package    |
#              |  created by A.Djouadi, M.Muehlleitner and M.Spira. |
#              |  In case of problems with SUSY-HIT email to       |
#              |           margarete.muehlleitner@cern.ch          |
#              |           michael.spira@psi.ch                    |
#              |           abdelhak.djouadi@cern.ch                |
#              -----------------------------------------------------
#
#
#              -----------------------------------------------------
#              |  SUSY Les Houches Accord - MSSM Spectrum + Decays |
#              |              based on the decay programs          |
#              |                                                   |
#              |                     SDECAY 1.2                    |
```

```
#              |                                                      |
#              |  Authors: M.Muhlleitner, A.Djouadi and Y.Mambrini  |
#              |  Ref.:    Comput.Phys.Commun.168(2005)46           |
#              |           [hep-ph/0311167]                         |
#              |                                                      |
#              |                   HDECAY 3.302                      |
#              |                                                      |
#              |  By: A.Djouadi,J.Kalinowski,M.Muhlleitner,M.Spira  |
#              |  Ref.:    Comput.Phys.Commun.108(1998)56           |
#              |           [hep-ph/9704448]                         |
#              |                                                      |
#              |                                                      |
#              |  If not stated otherwise all DRbar couplings and    |
#              |  soft SUSY breaking masses are given at the scale  |
#              |  Q=  0.29052880E+03
#              |                                                      |
#              ------------------------------------------------------
#
#
BLOCK DCINFO  # Decay Program information
     1   SDECAY/HDECAY # decay calculator
     2   1.2   /3.302  # version number
#
BLOCK SPINFO  # Spectrum calculator information
     1   SOFTSUSY    # spectrum calculator
     2   2.0.17         # version number
#
BLOCK MODSEL  # Model selection
     1     1   #  sugra
#
BLOCK SMINPUTS  # Standard Model inputs
         1     1.27908953E+02   # alpha_em^-1(M_Z)^MSbar
         2     1.16639000E-05   # G_F [GeV^-2]
         3     1.17200000E-01   # alpha_S(M_Z)^MSbar
         4     9.11876000E+01   # M_Z pole mass
         5     4.20000000E+00   # mb(mb)^MSbar
         6     1.72500000E+02   # mt pole mass
         7     1.77700000E+00   # mtau pole mass
#
BLOCK MINPAR  # Input parameters - minimal models
         1     2.00000000E+02   # m0
         2     1.60000000E+02   # m12
         3     1.00000000E+01   # tanb
         4     1.00000000E+00   # sign(mu)
         5    -4.00000000E+02   # A0
#
BLOCK MASS  # Mass Spectrum
# PDG code           mass       particle
        24     8.04138255E+01   # W+
        25     1.09678376E+02   # h
        35     3.67818772E+02   # H
        36     3.68477914E+02   # A
        37     3.77172980E+02   # H+
         5     4.82427405E+00   # b-quark pole mass calculated from mb(mb)_Msbar
```

```
   1000001     4.22408741E+02   # ~d_L
   2000001     4.08440991E+02   # ~d_R
   1000002     4.14923367E+02   # ~u_L
   2000002     4.09350558E+02   # ~u_R
   1000003     4.22408741E+02   # ~s_L
   2000003     4.08440991E+02   # ~s_R
   1000004     4.14923367E+02   # ~c_L
   2000004     4.09350558E+02   # ~c_R
   1000005     3.56477562E+02   # ~b_1
   2000005     4.05691190E+02   # ~b_2
   1000006     2.06866084E+02   # ~t_1
   2000006     4.50242989E+02   # ~t_2
   1000011     2.31416110E+02   # ~e_L
   2000011     2.13226284E+02   # ~e_R
   1000012     2.17393007E+02   # ~nu_eL
   1000013     2.31416110E+02   # ~mu_L
   2000013     2.13226284E+02   # ~mu_R
   1000014     2.17393007E+02   # ~nu_muL
   1000015     2.00492664E+02   # ~tau_1
   2000015     2.35911586E+02   # ~tau_2
   1000016     2.14978264E+02   # ~nu_tauL
   1000021     4.08752622E+02   # ~g
   1000022     6.04649022E+01   # ~chi_10
   1000023     1.13166598E+02   # ~chi_20
   1000025    -3.15651716E+02   # ~chi_30
   1000035     3.28274339E+02   # ~chi_40
   1000024     1.13805260E+02   # ~chi_1+
   1000037     3.27346096E+02   # ~chi_2+
#
BLOCK NMIX  # Neutralino Mixing Matrix
  1  1     9.79183656E-01   # N_11
  1  2    -8.70017948E-02   # N_12
  1  3     1.75813037E-01   # N_13
  1  4    -5.21520034E-02   # N_14
  2  1     1.39174513E-01   # N_21
  2  2     9.44472080E-01   # N_22
  2  3    -2.71658234E-01   # N_23
  2  4     1.21674770E-01   # N_24
  3  1    -7.50233573E-02   # N_31
  3  2     1.16844446E-01   # N_32
  3  3     6.87186106E-01   # N_33
  3  4     7.13087741E-01   # N_34
  4  1    -1.27284400E-01   # N_41
  4  2     2.94534470E-01   # N_42
  4  3     6.50435881E-01   # N_43
  4  4    -6.88462993E-01   # N_44
#
BLOCK UMIX  # Chargino Mixing Matrix U
  1  1     9.15480281E-01   # U_11
  1  2    -4.02362840E-01   # U_12
  2  1     4.02362840E-01   # U_21
  2  2     9.15480281E-01   # U_22
#
BLOCK VMIX  # Chargino Mixing Matrix V
```

```
  1  1     9.82636204E-01   # V_11
  1  2    -1.85542692E-01   # V_12
  2  1     1.85542692E-01   # V_21
  2  2     9.82636204E-01   # V_22
#
BLOCK STOPMIX  # Stop Mixing Matrix
  1  1     5.78881371E-01   # cos(theta_t)
  1  2     8.15411772E-01   # sin(theta_t)
  2  1    -8.15411772E-01   # -sin(theta_t)
  2  2     5.78881371E-01   # cos(theta_t)
#
BLOCK SBOTMIX  # Sbottom Mixing Matrix
  1  1     9.66726392E-01   # cos(theta_b)
  1  2     2.55812594E-01   # sin(theta_b)
  2  1    -2.55812594E-01   # -sin(theta_b)
  2  2     9.66726392E-01   # cos(theta_b)
#
BLOCK STAUMIX  # Stau Mixing Matrix
  1  1     4.51419848E-01   # cos(theta_tau)
  1  2     8.92311672E-01   # sin(theta_tau)
  2  1    -8.92311672E-01   # -sin(theta_tau)
  2  2     4.51419848E-01   # cos(theta_tau)
#
BLOCK ALPHA  # Higgs mixing
          -1.13676047E-01   # Mixing angle in the neutral Higgs boson sector
#
BLOCK HMIX Q=  2.90528802E+02  # DRbar Higgs Parameters
         1     3.05599351E+02   # mu(Q)MSSM
         2     9.82088559E+00   # tan
         3     2.45715311E+02   # higgs
         4     1.42679732E+05   # mA^2(Q)MSSM
#
BLOCK GAUGE Q=  2.90528802E+02  # The gauge couplings
     1     3.59577459E-01   # gprime(Q) DRbar
     2     6.47595300E-01   # g(Q) DRbar
     3     1.12149476E+00   # g3(Q) DRbar
#
BLOCK AU Q=  2.90528802E+02  # The trilinear couplings
  1  1     0.00000000E+00   # A_u(Q) DRbar
  2  2     0.00000000E+00   # A_c(Q) DRbar
  3  3    -4.46245994E+02   # A_t(Q) DRbar
#
BLOCK AD Q=  2.90528802E+02  # The trilinear couplings
  1  1     0.00000000E+00   # A_d(Q) DRbar
  2  2     0.00000000E+00   # A_s(Q) DRbar
  3  3    -8.28806503E+02   # A_b(Q) DRbar
#
BLOCK AE Q=  2.90528802E+02  # The trilinear couplings
  1  1     0.00000000E+00   # A_e(Q) DRbar
  2  2     0.00000000E+00   # A_mu(Q) DRbar
  3  3    -4.92306701E+02   # A_tau(Q) DRbar
#
BLOCK Yu Q=  2.90528802E+02  # The Yukawa couplings
  1  1     0.00000000E+00   # y_u(Q) DRbar
```

```
  2  2     0.00000000E+00   # y_c(Q) DRbar
  3  3     8.94108717E-01   # y_t(Q) DRbar
#
BLOCK Yd Q=  2.90528802E+02  # The Yukawa couplings
  1  1     0.00000000E+00   # y_d(Q) DRbar
  2  2     0.00000000E+00   # y_s(Q) DRbar
  3  3     1.40041975E-01   # y_b(Q) DRbar
#
BLOCK Ye Q=  2.90528802E+02  # The Yukawa couplings
  1  1     0.00000000E+00   # y_e(Q) DRbar
  2  2     0.00000000E+00   # y_mu(Q) DRbar
  3  3     1.01082232E-01   # y_tau(Q) DRbar
#
BLOCK MSOFT Q=  2.90528802E+02  # The soft SUSY breaking masses at the scale Q
         1     6.39136864E+01   # M_1(Q)
         2     1.22006983E+02   # M_2(Q)
         3     3.90619532E+02   # M_3(Q)
        21     4.42860395E+04   # mH1^2(Q)
        22    -9.76585434E+04   # mH2^2(Q)
        31     2.26648170E+02   # meL(Q)
        32     2.26648170E+02   # mmuL(Q)
        33     2.24355944E+02   # mtauL(Q)
        34     2.08394096E+02   # meR(Q)
        35     2.08394096E+02   # mmuR(Q)
        36     2.03337218E+02   # mtauR(Q)
        41     4.08594291E+02   # mqL1(Q)
        42     4.08594291E+02   # mqL2(Q)
        43     3.46134575E+02   # mqL3(Q)
        44     3.98943379E+02   # muR(Q)
        45     3.98943379E+02   # mcR(Q)
        46     2.58021672E+02   # mtR(Q)
        47     3.95211849E+02   # mdR(Q)
        48     3.95211849E+02   # msR(Q)
        49     3.90320031E+02   # mbR(Q)
#
#
#
#                             =================
#                             |The decay table|
#                             =================
#
# - The QCD corrections to the decays gluino -> squark  + quark
#                                     squark -> gaugino + quark_prime
#                                     squark -> squark_prime + Higgs
#                                     squark -> gluino  + quark
#   are included.
#
# - The multi-body decays for the inos, stops and sbottoms are included.
#
# - The loop induced decays for the gluino, neutralinos and stops
#   are included.
#
# - The SUSY decays of the top quark are included.
#
```

```
#
#         PDG            Width
DECAY         6     1.45512044E+00   # top decays
#          BR         NDA      ID1       ID2
     1.00000000E+00    2           5        24   # BR(t ->  b    W+)
#
#         PDG            Width
DECAY   1000021     9.06988410E-01   # gluino decays
#          BR         NDA      ID1       ID2
     1.28013590E-05    2     2000001        -1   # BR(~g -> ~d_R  db)
     1.28013590E-05    2    -2000001         1   # BR(~g -> ~d_R* d )
     1.28013590E-05    2     2000003        -3   # BR(~g -> ~s_R  sb)
     1.28013590E-05    2    -2000003         3   # BR(~g -> ~s_R* s )
     2.71501429E-01    2     1000005        -5   # BR(~g -> ~b_1  bb)
     2.71501429E-01    2    -1000005         5   # BR(~g -> ~b_1* b )
     2.28472968E-01    2     1000006        -6   # BR(~g -> ~t_1  tb)
     2.28472968E-01    2    -1000006         6   # BR(~g -> ~t_1* t )
#
#         PDG            Width
DECAY   1000006     5.15894598E-01   # stop1 decays
#          BR         NDA      ID1       ID2
     1.00000000E+00    2     1000024         5   # BR(~t_1 -> ~chi_1+ b )
#
#         PDG            Width
DECAY   2000006     5.70929282E+00   # stop2 decays
#          BR         NDA      ID1       ID2
     2.77875138E-02    2     1000022         6   # BR(~t_2 -> ~chi_10 t )
     8.27687601E-02    2     1000023         6   # BR(~t_2 -> ~chi_20 t )
     0.00000000E+00    2     1000025         6   # BR(~t_2 -> ~chi_30 t )
     2.43546028E-01    2     1000024         5   # BR(~t_2 -> ~chi_1+ b )
     1.26509812E-01    2     1000037         5   # BR(~t_2 -> ~chi_2+ b )
     6.06695063E-02    2     1000006        25   # BR(~t_2 -> ~t_1    h )
     4.17191613E-01    2     1000006        23   # BR(~t_2 -> ~t_1    Z )
     4.15267667E-02    2     1000005        24   # BR(~t_2 -> ~b_1    W+)
#
#         PDG            Width
DECAY   1000005     3.34221921E+00   # sbottom1 decays
#          BR         NDA      ID1       ID2
     3.89294437E-02    2     1000022         5   # BR(~b_1 -> ~chi_10 b )
     2.92276323E-01    2     1000023         5   # BR(~b_1 -> ~chi_20 b )
     8.30227912E-04    2     1000025         5   # BR(~b_1 -> ~chi_30 b )
     1.17241176E-03    2     1000035         5   # BR(~b_1 -> ~chi_40 b )
     2.38092065E-01    2    -1000024         6   # BR(~b_1 -> ~chi_1- t )
     4.28699528E-01    2     1000006       -24   # BR(~b_1 -> ~t_1    W-)
#
#         PDG            Width
DECAY   2000005     5.26208813E-01   # sbottom2 decays
#          BR         NDA      ID1       ID2
     3.34784961E-01    2     1000022         5   # BR(~b_2 -> ~chi_10 b )
     7.61292555E-02    2     1000023         5   # BR(~b_2 -> ~chi_20 b )
     2.93022353E-02    2     1000025         5   # BR(~b_2 -> ~chi_30 b )
     3.23453025E-02    2     1000035         5   # BR(~b_2 -> ~chi_40 b )
     6.86994071E-02    2    -1000024         6   # BR(~b_2 -> ~chi_1- t )
     4.58738838E-01    2     1000006       -24   # BR(~b_2 -> ~t_1    W-)
```

```
#
#         PDG            Width
DECAY   1000002     4.22659094E+00   # sup_L decays
#          BR         NDA      ID1       ID2
     3.33296601E-03    2     1000022         2   # BR(~u_L -> ~chi_10 u)
     3.20754377E-01    2     1000023         2   # BR(~u_L -> ~chi_20 u)
     8.68224929E-04    2     1000025         2   # BR(~u_L -> ~chi_30 u)
     4.87273338E-03    2     1000035         2   # BR(~u_L -> ~chi_40 u)
     6.56954600E-01    2     1000024         1   # BR(~u_L -> ~chi_1+ d)
     4.64546048E-03    2     1000037         1   # BR(~u_L -> ~chi_2+ d)
     8.57163752E-03    2     1000021         2   # BR(~u_L -> ~g      u)
#
#         PDG            Width
DECAY   2000002     8.43549822E-01   # sup_R decays
#          BR         NDA      ID1       ID2
     9.77849677E-01    2     1000022         2   # BR(~u_R -> ~chi_10 u)
     1.78770897E-02    2     1000023         2   # BR(~u_R -> ~chi_20 u)
     1.16990619E-03    2     1000025         2   # BR(~u_R -> ~chi_30 u)
     2.68904297E-03    2     1000035         2   # BR(~u_R -> ~chi_40 u)
     4.14284181E-04    2     1000021         2   # BR(~u_R -> ~g      u)
#
#         PDG            Width
DECAY   1000001     4.12869025E+00   # sdown_L decays
#          BR         NDA      ID1       ID2
     2.80998260E-02    2     1000022         1   # BR(~d_L -> ~chi_10 d)
     3.00386578E-01    2     1000023         1   # BR(~d_L -> ~chi_20 d)
     1.58346850E-03    2     1000025         1   # BR(~d_L -> ~chi_30 d)
     7.72613060E-03    2     1000035         1   # BR(~d_L -> ~chi_40 d)
     5.95627042E-01    2    -1000024         2   # BR(~d_L -> ~chi_1- u)
     2.51021857E-02    2    -1000037         2   # BR(~d_L -> ~chi_2- u)
     4.14747685E-02    2     1000021         1   # BR(~d_L -> ~g      d)
#
#         PDG            Width
DECAY   2000001     2.10535799E-01   # sdown_R decays
#          BR         NDA      ID1       ID2
     9.78314713E-01    2     1000022         1   # BR(~d_R -> ~chi_10 d)
     1.78763148E-02    2     1000023         1   # BR(~d_R -> ~chi_20 d)
     1.15681554E-03    2     1000025         1   # BR(~d_R -> ~chi_30 d)
     2.65215688E-03    2     1000035         1   # BR(~d_R -> ~chi_40 d)
#
#         PDG            Width
DECAY   1000004     4.22659094E+00   # scharm_L decays
#          BR         NDA      ID1       ID2
     3.33296601E-03    2     1000022         4   # BR(~c_L -> ~chi_10 c)
     3.20754377E-01    2     1000023         4   # BR(~c_L -> ~chi_20 c)
     8.68224929E-04    2     1000025         4   # BR(~c_L -> ~chi_30 c)
     4.87273338E-03    2     1000035         4   # BR(~c_L -> ~chi_40 c)
     6.56954600E-01    2     1000024         3   # BR(~c_L -> ~chi_1+ s)
     4.64546048E-03    2     1000037         3   # BR(~c_L -> ~chi_2+ s)
     8.57163752E-03    2     1000021         4   # BR(~c_L -> ~g      c)
#
#         PDG            Width
DECAY   2000004     8.43549822E-01   # scharm_R decays
#          BR         NDA      ID1       ID2
```

```
     9.77849677E-01    2     1000022         4   # BR(~c_R -> ~chi_10 c)
     1.78770897E-02    2     1000023         4   # BR(~c_R -> ~chi_20 c)
     1.16990619E-03    2     1000025         4   # BR(~c_R -> ~chi_30 c)
     2.68904297E-03    2     1000035         4   # BR(~c_R -> ~chi_40 c)
     4.14284181E-04    2     1000021         4   # BR(~c_R -> ~g      c)
#
#         PDG            Width
DECAY   1000003     4.12869025E+00   # sstrange_L decays
#          BR         NDA      ID1       ID2
     2.80998260E-02    2     1000022         3   # BR(~s_L -> ~chi_10 s)
     3.00386578E-01    2     1000023         3   # BR(~s_L -> ~chi_20 s)
     1.58346850E-03    2     1000025         3   # BR(~s_L -> ~chi_30 s)
     7.72613060E-03    2     1000035         3   # BR(~s_L -> ~chi_40 s)
     5.95627042E-01    2    -1000024         4   # BR(~s_L -> ~chi_1- c)
     2.51021857E-02    2    -1000037         4   # BR(~s_L -> ~chi_2- c)
     4.14747685E-02    2     1000021         3   # BR(~s_L -> ~g      s)
#
#         PDG            Width
DECAY   2000003     2.10535799E-01   # sstrange_R decays
#          BR         NDA      ID1       ID2
     9.78314713E-01    2     1000022         3   # BR(~s_R -> ~chi_10 s)
     1.78763148E-02    2     1000023         3   # BR(~s_R -> ~chi_20 s)
     1.15681554E-03    2     1000025         3   # BR(~s_R -> ~chi_30 s)
     2.65215688E-03    2     1000035         3   # BR(~s_R -> ~chi_40 s)
#
#         PDG            Width
DECAY   1000011     1.68837245E+00   # selectron_L decays
#          BR         NDA      ID1       ID2
     1.03528016E-01    2     1000022        11   # BR(~e_L -> ~chi_10 e-)
     3.45567122E-01    2     1000023        11   # BR(~e_L -> ~chi_20 e-)
     5.50904862E-01    2    -1000024        12   # BR(~e_L -> ~chi_1- nu_e)
#
#         PDG            Width
DECAY   2000011     9.00369070E-01   # selectron_R decays
#          BR         NDA      ID1       ID2
     9.87823532E-01    2     1000022        11   # BR(~e_R -> ~chi_10 e-)
     1.21764678E-02    2     1000023        11   # BR(~e_R -> ~chi_20 e-)
#
#         PDG            Width
DECAY   1000013     1.68837245E+00   # smuon_L decays
#          BR         NDA      ID1       ID2
     1.03528016E-01    2     1000022        13   # BR(~mu_L -> ~chi_10 mu-)
     3.45567122E-01    2     1000023        13   # BR(~mu_L -> ~chi_20 mu-)
     5.50904862E-01    2    -1000024        14   # BR(~mu_L -> ~chi_1- nu_mu)
#
#         PDG            Width
DECAY   2000013     9.00369070E-01   # smuon_R decays
#          BR         NDA      ID1       ID2
     9.87823532E-01    2     1000022        13   # BR(~mu_R -> ~chi_10 mu-)
     1.21764678E-02    2     1000023        13   # BR(~mu_R -> ~chi_20 mu-)
#
#         PDG            Width
DECAY   1000015     9.73528945E-01   # stau_1 decays
#          BR         NDA      ID1       ID2
```

```
     7.14912605E-01    2     1000022        15   # BR(~tau_1 -> ~chi_10  tau-)
     1.11226405E-01    2     1000023        15   # BR(~tau_1 -> ~chi_20  tau-)
     1.73860990E-01    2    -1000024        16   # BR(~tau_1 -> ~chi_1-  nu_tau)
#
#         PDG            Width
DECAY   2000015     1.51721597E+00   # stau_2 decays
#          BR         NDA      ID1       ID2
     2.19213747E-01    2     1000022        15   # BR(~tau_2 -> ~chi_10  tau-)
     3.05886304E-01    2     1000023        15   # BR(~tau_2 -> ~chi_20  tau-)
     4.74899949E-01    2    -1000024        16   # BR(~tau_2 -> ~chi_1-  nu_tau)
#
#         PDG            Width
DECAY   1000012     1.59249440E+00   # snu_eL decays
#          BR         NDA      ID1       ID2
     1.92831055E-01    2     1000022        12   # BR(~nu_eL -> ~chi_10 nu_e)
     2.27605074E-01    2     1000023        12   # BR(~nu_eL -> ~chi_20 nu_e)
     5.79563872E-01    2     1000024        11   # BR(~nu_eL -> ~chi_1+ e-)
#
#         PDG            Width
DECAY   1000014     1.59249440E+00   # snu_muL decays
#          BR         NDA      ID1       ID2
     1.92831055E-01    2     1000022        14   # BR(~nu_muL -> ~chi_10 nu_mu)
     2.27605074E-01    2     1000023        14   # BR(~nu_muL -> ~chi_20 nu_mu)
     5.79563872E-01    2     1000024        13   # BR(~nu_muL -> ~chi_1+ mu-)
#
#         PDG            Width
DECAY   1000016     1.55419332E+00   # snu_tauL decays
#          BR         NDA      ID1       ID2
     1.94648925E-01    2     1000022        16   # BR(~nu_tauL -> ~chi_10 nu_tau)
     2.26766587E-01    2     1000023        16   # BR(~nu_tauL -> ~chi_20 nu_tau)
     5.78584488E-01    2     1000024        15   # BR(~nu_tauL -> ~chi_1+ tau-)
#
#         PDG            Width
DECAY   1000024     2.02592183E-05   # chargino1+ decays
#           BR         NDA    ID1    ID2    ID3
     3.25108945E-01    3   1000022     2     -1   # BR(~chi_1+ -> ~chi_10 u    db)
     8.14298534E-09    3   1000023     2     -1   # BR(~chi_1+ -> ~chi_20 u    db)
     3.25108945E-01    3   1000022     4     -3   # BR(~chi_1+ -> ~chi_10 c    sb)
     8.14298534E-09    3   1000023     4     -3   # BR(~chi_1+ -> ~chi_20 c    sb)
     1.15395979E-01    3   1000022   -11     12   # BR(~chi_1+ -> ~chi_10 e+   nu_e)
     3.06009766E-09    3   1000023   -11     12   # BR(~chi_1+ -> ~chi_20 e+   nu_e)
     1.15395979E-01    3   1000022   -13     14   # BR(~chi_1+ -> ~chi_10 mu+  nu_mu)
     3.06009766E-09    3   1000023   -13     14   # BR(~chi_1+ -> ~chi_20 mu+  nu_mu)
     1.18990129E-01    3   1000022   -15     16   # BR(~chi_1+ -> ~chi_10 tau+ nu_tau)
#
#         PDG            Width
DECAY   1000037     3.84095144E+00   # chargino2+ decays
#          BR         NDA      ID1       ID2
     4.84630150E-01    2     1000006        -5   # BR(~chi_2+ -> ~t_1     bb)
     3.82407931E-03    2     1000012       -11   # BR(~chi_2+ -> ~nu_eL   e+  )
     3.82407931E-03    2     1000014       -13   # BR(~chi_2+ -> ~nu_muL  mu+ )
     6.18962954E-03    2     1000016       -15   # BR(~chi_2+ -> ~nu_tau1 tau+)
     1.44027609E-02    2    -1000011        12   # BR(~chi_2+ -> ~e_L+    nu_e)
     1.44027609E-02    2    -1000013        14   # BR(~chi_2+ -> ~mu_L+   nu_mu)
```

```
     4.06704239E-04    2    -1000015        16   # BR(~chi_2+ -> ~tau_1+  nu_tau)
     1.47322432E-02    2    -2000015        16   # BR(~chi_2+ -> ~tau_2+  nu_tau)
     1.41583019E-01    2     1000024        23   # BR(~chi_2+ -> ~chi_1+  Z )
     3.35640651E-02    2     1000022        24   # BR(~chi_2+ -> ~chi_10  W+)
     1.75210113E-01    2     1000023        24   # BR(~chi_2+ -> ~chi_20  W+)
     1.07230396E-01    2     1000024        25   # BR(~chi_2+ -> ~chi_1+  h )
#
#         PDG            Width
DECAY   1000022     0.00000000E+00   # neutralino1 decays
#
#         PDG            Width
DECAY   1000023     1.76326880E-06   # neutralino2 decays
#          BR         NDA    ID1    ID2
     4.63309293E-05    2   1000022     22   # BR(~chi_20 -> ~chi_10 gam)
#           BR         NDA   ID1    ID2    ID3
     1.13426857E-01    3  1000022     -2      2   # BR(~chi_20 -> ~chi_10 ub      u)
     1.71052155E-01    3  1000022     -1      1   # BR(~chi_20 -> ~chi_10 db      d)
     1.13426857E-01    3  1000022     -4      4   # BR(~chi_20 -> ~chi_10 cb      c)
     1.71052155E-01    3  1000022     -3      3   # BR(~chi_20 -> ~chi_10 sb      s)
     1.84168930E-01    3  1000022     -5      5   # BR(~chi_20 -> ~chi_10 bb      b)
     3.27836119E-02    3  1000022     -11     11   # BR(~chi_20 -> ~chi_10 e+      e-)
     3.27836119E-02    3  1000022     -13     13   # BR(~chi_20 -> ~chi_10 mu+     mu-)
     7.94402020E-02    3  1000022     -15     15   # BR(~chi_20 -> ~chi_10 tau+    tau-)
     3.25750309E-02    3  1000022     -12     12   # BR(~chi_20 -> ~chi_10 nu_eb   nu_e)
     3.25750309E-02    3  1000022     -14     14   # BR(~chi_20 -> ~chi_10 nu_mub  nu_mu)
     3.66692266E-02    3  1000022     -16     16   # BR(~chi_20 -> ~chi_10 nu_taub nu_tau)
#
#         PDG            Width
DECAY   1000025     1.91296878E+00   # neutralino3 decays
#          BR         NDA      ID1       ID2
     1.06362845E-01    2     1000022        23   # BR(~chi_30 -> ~chi_10   Z )
     2.02496323E-01    2     1000023        23   # BR(~chi_30 -> ~chi_20   Z )
     3.07164105E-01    2     1000024       -24   # BR(~chi_30 -> ~chi_1+   W-)
     3.07164105E-01    2    -1000024        24   # BR(~chi_30 -> ~chi_1-   W+)
     2.55300984E-02    2     1000022        25   # BR(~chi_30 -> ~chi_10   h )
     2.30942864E-02    2     1000023        25   # BR(~chi_30 -> ~chi_20   h )
     4.16210109E-04    2     1000011       -11   # BR(~chi_30 -> ~e_L-     e+)
     4.16210109E-04    2    -1000011        11   # BR(~chi_30 -> ~e_L+     e-)
     7.06158706E-04    2     2000011       -11   # BR(~chi_30 -> ~e_R-     e+)
     7.06158706E-04    2    -2000011        11   # BR(~chi_30 -> ~e_R+     e-)
     4.16210109E-04    2     1000013       -13   # BR(~chi_30 -> ~mu_L-    mu+)
     4.16210109E-04    2    -1000013        13   # BR(~chi_30 -> ~mu_L+    mu-)
     7.06158706E-04    2     2000013       -13   # BR(~chi_30 -> ~mu_R-    mu+)
     7.06158706E-04    2    -2000013        13   # BR(~chi_30 -> ~mu_R+    mu-)
     1.26662445E-03    2     1000015       -15   # BR(~chi_30 -> ~tau_1-   tau+)
     1.26662445E-03    2    -1000015        15   # BR(~chi_30 -> ~tau_1+   tau-)
     3.31850113E-03    2     2000015       -15   # BR(~chi_30 -> ~tau_2-   tau+)
     3.31850113E-03    2    -2000015        15   # BR(~chi_30 -> ~tau_2+   tau-)
     2.38934912E-03    2     1000012       -12   # BR(~chi_30 -> ~nu_eL    nu_eb)
     2.38934912E-03    2    -1000012        12   # BR(~chi_30 -> ~nu_eL*   nu_e )
     2.38934912E-03    2     1000014       -14   # BR(~chi_30 -> ~nu_muL   nu_mub)
     2.38934912E-03    2    -1000014        14   # BR(~chi_30 -> ~nu_muL*  nu_mu )
     2.48555682E-03    2     1000016       -16   # BR(~chi_30 -> ~nu_tau1  nu_taub)
     2.48555682E-03    2    -1000016        16   # BR(~chi_30 -> ~nu_tau1* nu_tau )
```

```
#
#         PDG            Width
DECAY   1000035     2.14754220E+00   # neutralino4 decays
#          BR         NDA      ID1       ID2
     3.19185540E-02    2     1000022        23   # BR(~chi_40 -> ~chi_10   Z )
     3.68354144E-02    2     1000023        23   # BR(~chi_40 -> ~chi_20   Z )
     2.96827219E-01    2     1000024       -24   # BR(~chi_40 -> ~chi_1+   W-)
     2.96827219E-01    2    -1000024        24   # BR(~chi_40 -> ~chi_1-   W+)
     7.10045983E-02    2     1000022        25   # BR(~chi_40 -> ~chi_10   h )
     1.43832002E-01    2     1000023        25   # BR(~chi_40 -> ~chi_20   h )
     4.04339321E-03    2     1000011       -11   # BR(~chi_40 -> ~e_L-     e+)
     4.04339321E-03    2    -1000011        11   # BR(~chi_40 -> ~e_L+     e-)
     2.12896927E-03    2     2000011       -11   # BR(~chi_40 -> ~e_R-     e+)
     2.12896927E-03    2    -2000011        11   # BR(~chi_40 -> ~e_R+     e-)
     4.04339321E-03    2     1000013       -13   # BR(~chi_40 -> ~mu_L-    mu+)
     4.04339321E-03    2    -1000013        13   # BR(~chi_40 -> ~mu_L+    mu-)
     2.12896927E-03    2     2000013       -13   # BR(~chi_40 -> ~mu_R-    mu+)
     2.12896927E-03    2    -2000013        13   # BR(~chi_40 -> ~mu_R+    mu-)
     5.55778220E-04    2     1000015       -15   # BR(~chi_40 -> ~tau_1-   tau+)
     5.55778220E-04    2    -1000015        15   # BR(~chi_40 -> ~tau_1+   tau-)
     7.79402438E-03    2     2000015       -15   # BR(~chi_40 -> ~tau_2-   tau+)
     7.79402438E-03    2    -2000015        15   # BR(~chi_40 -> ~tau_2+   tau-)
     1.34054425E-02    2     1000012       -12   # BR(~chi_40 -> ~nu_eL    nu_eb)
     1.34054425E-02    2    -1000012        12   # BR(~chi_40 -> ~nu_eL*   nu_e )
     1.34054425E-02    2     1000014       -14   # BR(~chi_40 -> ~nu_muL   nu_mub)
     1.34054425E-02    2    -1000014        14   # BR(~chi_40 -> ~nu_muL*  nu_mu )
     1.38720842E-02    2     1000016       -16   # BR(~chi_40 -> ~nu_tau1  nu_taub)
     1.38720842E-02    2    -1000016        16   # BR(~chi_40 -> ~nu_tau1* nu_tau )
#
#         PDG            Width
DECAY        25     4.00529014E-03   # h decays
#          BR         NDA      ID1       ID2
     8.24690783E-01    2           5        -5   # BR(h -> b       bb     )
     7.10466803E-02    2         -15        15   # BR(h -> tau+    tau-   )
     2.51570008E-04    2         -13        13   # BR(h -> mu+     mu-    )
     5.46231030E-04    2           3        -3   # BR(h -> s       sb     )
     1.89770714E-02    2           4        -4   # BR(h -> c       cb     )
     4.88775680E-02    2          21        21   # BR(h -> g       g      )
     1.41066784E-03    2          22        22   # BR(h -> gam     gam    )
     2.63283022E-04    2          22        23   # BR(h -> Z       gam    )
     3.10766585E-02    2          24       -24   # BR(h -> W+      W-     )
     2.85948659E-03    2          23        23   # BR(h -> Z       Z      )
#
#         PDG            Width
DECAY        35     8.96646571E-01   # H decays
#          BR         NDA      ID1       ID2
     6.13975163E-01    2           5        -5   # BR(H -> b       bb     )
     8.17715620E-02    2         -15        15   # BR(H -> tau+    tau-   )
     2.89131903E-04    2         -13        13   # BR(H -> mu+     mu-    )
     4.88180143E-04    2           3        -3   # BR(H -> s       sb     )
     2.94977206E-06    2           4        -4   # BR(H -> c       cb     )
     2.20017152E-02    2           6        -6   # BR(H -> t       tb     )
     2.29380057E-03    2          21        21   # BR(H -> g       g      )
     1.48567409E-05    2          22        22   # BR(H -> gam     gam    )
```

```
     3.82401119E-07    2          23        22   # BR(H -> Z       gam    )
     2.03918830E-03    2          24       -24   # BR(H -> W+      W-     )
     9.41276585E-04    2          23        23   # BR(H -> Z       Z      )
     9.82321398E-03    2          25        25   # BR(H -> h       h      )
     2.35526927E-01    2     1000024  -1000024   # BR(H -> ~chi_1+ ~chi_1-)
     2.96812053E-02    2     1000022   1000022   # BR(H -> ~chi_10 ~chi_10)
     7.04661026E-06    2     1000023   1000023   # BR(H -> ~chi_20 ~chi_20)
     1.14340079E-03    2     1000022   1000023   # BR(H -> ~chi_10 ~chi_20)
#
#         PDG            Width
DECAY        36     1.19000793E+00   # A decays
#          BR         NDA      ID1       ID2
     4.60406389E-01    2           5        -5   # BR(A -> b       bb     )
     6.18922814E-02    2         -15        15   # BR(A -> tau+    tau-   )
     2.18821371E-04    2         -13        13   # BR(A -> mu+     mu-    )
     3.69615832E-04    2           3        -3   # BR(A -> s       sb     )
     1.79124445E-06    2           4        -4   # BR(A -> c       cb     )
     9.70878072E-02    2           6        -6   # BR(A -> t       tb     )
     4.83541115E-04    2          21        21   # BR(A -> g       g      )
     1.81838696E-06    2          22        22   # BR(A -> gam     gam    )
     3.22195738E-07    2          23        22   # BR(A -> Z       gam    )
     1.20574160E-03    2          23        25   # BR(A -> Z       h      )
     3.48378875E-01    2     1000024  -1000024   # BR(A -> ~chi_1+ ~chi_1-)
     2.86432211E-02    2     1000022   1000022   # BR(A -> ~chi_10 ~chi_10)
     1.04335620E-05    2     1000023   1000023   # BR(A -> ~chi_20 ~chi_20)
     1.29934039E-03    2     1000022   1000023   # BR(A -> ~chi_10 ~chi_20)
#
#         PDG            Width
DECAY        37     8.30198418E-01   # H+ decays
#          BR         NDA      ID1       ID2
     9.90848751E-04    2           4        -5   # BR(H+ -> c       bb     )
     9.08101674E-02    2         -15        16   # BR(H+ -> tau+    nu_tau )
     3.21060444E-04    2         -13        14   # BR(H+ -> mu+     nu_mu  )
     6.34103482E-06    2           2        -5   # BR(H+ -> u       bb     )
     2.56196481E-05    2           2        -3   # BR(H+ -> u       sb     )
     5.29423212E-04    2           4        -3   # BR(H+ -> c       sb     )
     6.65559207E-01    2           6        -5   # BR(H+ -> t       bb     )
     2.01620485E-03    2          24        25   # BR(H+ -> W+      h      )
     7.66171168E-08    2          24        36   # BR(H+ -> W+      A      )
     2.38277408E-01    2     1000024   1000022   # BR(H+ -> ~chi_1+ ~chi_10)
     1.46364297E-03    2     1000024   1000023   # BR(H+ -> ~chi_1+ ~chi_20)
```

APPENDIX D
VALIDATION OF FAST SIMULATION OF MSUGRA SAMPLES

Table D-1. Number of events (normalized to an integrated luminosity of 100 pb^{-1}) for SUSY LM0 FullSim and FastSim samples after sequentially applying the final set of cuts for all same-charge di-lepton channels.

	i	10 TeV FullSim			10 TeV FastSim					
		LM0 ($A_0 = -400$)			LM0 ($A_0 = -400$)			LM0 ($A_0 = 0$)		
		n_i	n_i/n_0 (%)	n_i/n_{i-1} (%)	n_i	n_i/n_0 (%)	n_i/n_{i-1} (%)	n_i	n_i/n_0 (%)	n_i/n_{i-1} (%)
No cuts	0	16601	100		16577	100		14550	100	
$\mu\mu$ channel										
Same-sign $\mu\mu$	1	244	1.5	1.5	243	1.5	1.5	110	0.76	0.8
MET	2	140	0.84	57	140	0.85	58	77	0.53	69
1^{st} jet E_T	3	137	0.83	98	137	0.83	98	75	0.52	98
2^{nd} jet E_T	4	115	0.69	84	114	0.69	83	63	0.43	83
3^{rd} jet E_T	5	104	0.63	90	101	0.61	89	54	0.37	87
Iso_{Tight} μ	6	76	0.46	73	75	0.45	75	37	0.26	69
Iso_{Loose} μ	7	20	0.12	27	19	0.11	25	7	0.049	19
Di-μ HLT	8	19	0.11	95	18	0.11	95	7	0.047	96
Skim	9	19	0.11	100	18	0.11	100	7	0.047	100
$e\mu$ channel										
Same-sign $e\mu$	1	791	4.8	4.8	657	4.0	4.0	355	2.4	2.4
MET	2	446	2.7	56	373	2.3	57	234	1.6	66
1^{st} jet E_T	3	401	2.4	90	334	2.0	89	210	1.4	90
2^{nd} jet E_T	4	309	1.9	77	252	1.5	75	154	1.1	73
3^{rd} jet E_T	5	269	1.6	87	212	1.3	84	128	0.88	83
Iso μ	6	105	0.63	39	81	0.49	38	43	0.30	34
Iso e	7	22	0.13	21	21	0.13	26	10	0.068	23
Skim	8	22	0.13	100	21	0.13	100	10	0.068	100
ee channel										
Same-sign ee	1	668	4.0	4.0	445	2.7	2.7	262	1.8	1.8
MET	2	482	2.9	72	319	1.9	72	209	1.4	80
1^{st} jet E_T	3	432	2.6	90	282	1.7	88	183	1.3	88
2^{nd} jet E_T	4	271	1.6	63	177	1.1	63	110	0.76	60
3^{rd} jet E_T	5	230	1.4	85	145	0.88	82	88	0.61	80
Iso_{Tight} e	6	110	0.66	48	85	0.51	59	45	0.31	50
Iso_{Loose} e	7	15	0.088	13	15	0.089	17	6	0.042	14
Di-e HLT	8	14	0.086	98	15	0.088	99	6	0.041	98
Skim	9	14	0.086	100	15	0.088	100	6	0.041	100

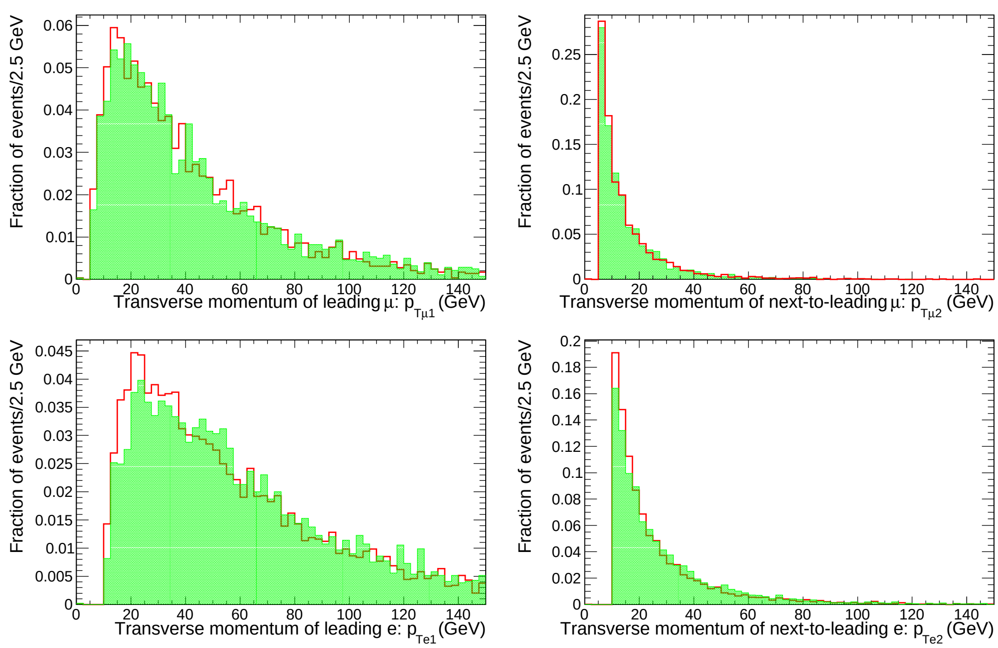

Figure D-1. Transverse momentum of reconstructed leading (top left) and next-to-leading (top right) muons in same-charge di-muon channel and transverse momentum of reconstructed leading (bottom left) and next-to-leading (bottom right) electrons in same-charge di-electron channel for SUSY LM0 FullSim (empty red histogram) and SUSY LM0 FastSim (shaded green histogram) samples.

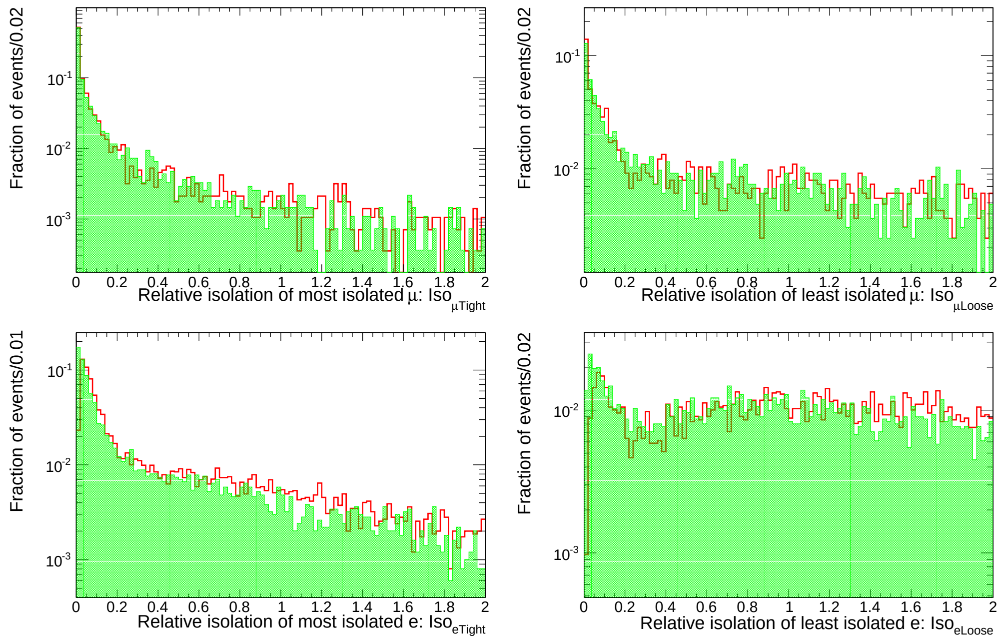

Figure D-2. Relative isolation of reconstructed most isolated (left top) and least isolated (right top) muons in same-charge di-muon channel and relative isolation of reconstructed most isolated (left top) and least isolated (right top) electrons in same-charge di-electron channel for SUSY LM0 (empty red histogram) and $t\bar{t}$ (shaded green histogram) samples.

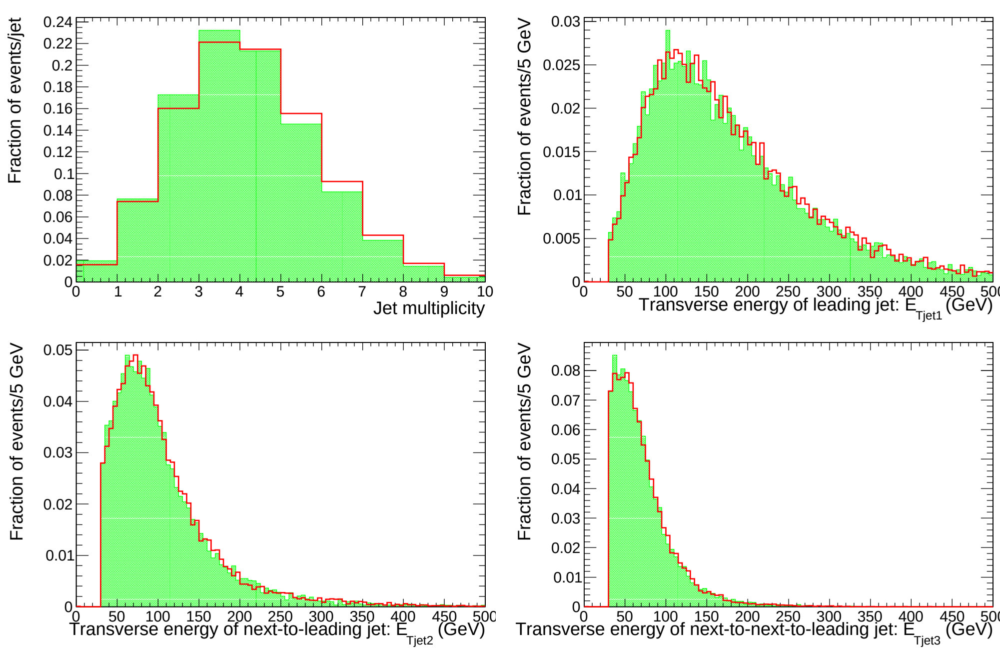

Figure D-3. Number of jets (top left) and E_T of leading (top right), next-to-leading (bottom left) and next-to-next-to-leading (bottom right) jets for SUSY LM0 (empty red histogram) and $t\bar{t}$ (shaded green histogram) samples.

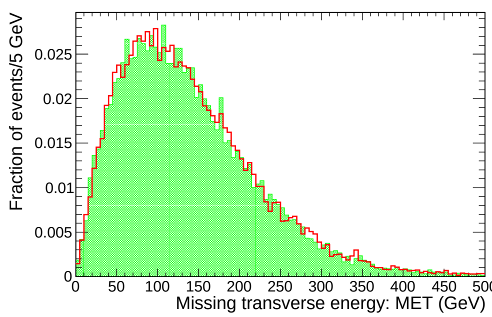

Figure D-4. Missing transverse energy for SUSY LM0 (empty red histogram) and $t\bar{t}$ (shaded green histogram) samples.

APPENDIX E
TRACK SEGMENTS RECONSTRUCTED OFFLINE

To improve our ability to predict track coordinates in the ME+2 chambers based on measurements in ME+1 and ME+3 chambers, we used a very simple track segment reconstruction algorithm based on anode hits and cathode comparator bits. Using this algorithm, we could localize segments to within a few millimeters in both the x and y directions. As a result, the precision with which we could predict muon track coordinates in the ME+2 chambers was mostly driven by the multiple scattering of cosmic ray muons in the Endcap steel disks. Here we describe the algorithm and evaluate its performance using MTCC data.

Anode Segments (AS) were searched for among anode hits using the same pattern as shown in Figure 5-1. Since muons with larger θ-angles are preferred [1] , the pattern was moved along a chamber starting from its wide side inward, one key wire group per step. If 6 layers with anode hits were present in the pattern at some step, then an anode segment was reported and all hits inside this pattern were deleted. Upon reaching the narrow end of the chamber, the procedure was repeated again with a requirement of 5 and, then, 4 layers with hits in the pattern. Anode segments were numbered sequentially, AS0, AS1, etc. The found anode segments were assigned (y_{AS}, z_{AS})-coordinates by taking the center of gravity (COG) of hits associated with them. If there was more than 1 hit per plane in a pattern, the hit weights were reduced so that the total weight per plane was always 1. In addition, a linear fit was used to evaluate the segment slope dy/dz. For a wire group width w, the expected error (RMS) on the y_{AS} coordinate would be $w/\sqrt{12}/\sqrt{6} \approx 0.12\,w$, or 2–6 mm, depending on the chamber type.

Cathode Segments (CS) were similarly searched for using half-strip comparator bits and the 9 patterns shown in Figure E-1 (they were obtained from the most recent

[1] In CMS, track segments at larger θ-angles are less likely to be due to backgrounds

CLCT-finding firmware). Sequentially, all 9 patterns were moved across the strips from one side of a chamber to the other. In the first pass, we looked for 6 layers with hits present in a pattern; then, for 5 layers, and, finally, for 4 layers with hits in a pattern. Cathode segments were numbered sequentially, CS0, CS1, etc. Similarly to anode segments, (ϕ_{CS}, z_{CS})-coordinates and track slopes $d\phi/dz$ were assigned to patterns. Using this technique, one would expect to achieve about 0.5–2 mm precision along the x coordinate, depending on the chamber type and muon hit location along the strips.

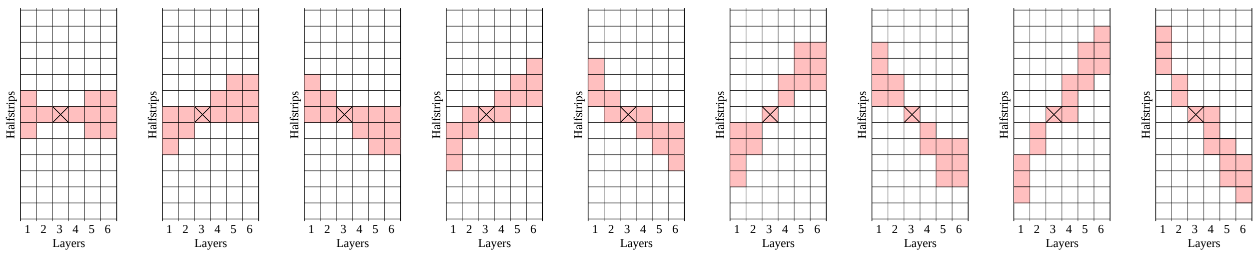

Figure E-1. Comparator bit patterns used for constructing cathode segments. The key half-strip is marked with a cross.

Anode and cathode segments were then combined to make a complete 2-dimensional Track Segment (TS). Whenever multiple ASs and/or CSs were found, we used all possible combinatorial pairings to make full 2d-TSs. If z_{CS} and z_{AS} were different, the track segment z coordinate z_{TS} was taken as $z_{TS} = 0.5 \times (z_{CS} + z_{AS})$ and (ϕ_{TS}, y_{TS})-coordinates were recalculated for the new z_{TS}-location using the $d\phi/dz$ and dy/dz slopes.

To evaluate the performance of the algorithm, we applied it to all the chambers in all 3 stations.

First, we found that the algorithm did find at least one track segment in all chambers with 2d-LCTs reported by hardware (total of 10 522 events). Therefore, the efficiency of finding track segments can be estimated to be $> 99.97\%$ at the 95% CL for chambers with hardware-found LCTs. Note that chambers in which hardware did not find an LCT would not be available for further analysis (High-Level trigger or offline).

Second, using track segments found in ME+1 and ME+3 (in the same way as described in the main body of the note), we predicted track positions in the ME+2 chambers and compared them to the track segments found by those chambers. The residuals are shown in Figure E-2 (ME+2/1 chambers) and Figure E-3 (ME+2/2 chambers). For these plots, if there were multiple TSs reconstructed in these chambers, we used the best track segment, TS0, even if it was not the closest to the predicted track position. One can see that the *dx* and *dy* distributions for ME+2/1 and the *dx* distribution for ME+2/2 have core widths $\sigma \approx$ 3.5 mm. The *dy* distribution for ME+2/2 has a core width $\sigma \approx$ 6 mm. Also, one can clearly see that residuals are not centered around zero; this is due to the Endcap disks' misalignment during the MTCC, which was confirmed by geodesic survey.

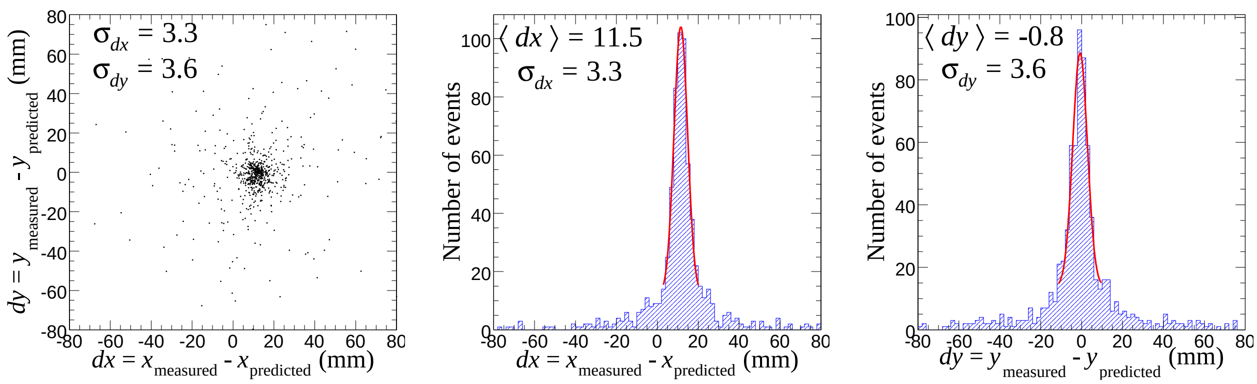

Figure E-2. Muon hit residuals in ME+2/1 chambers after an algorithm search for track segments and applying the "*COG*" technique to find the muon track segment coordinates.

To show that the obtained residuals are consistent with multiple scattering of muons, we performed the following calculations. A muon with an average inclination of 0.4 rad with respect to the horizon would lose approximately 9 GeV on its way through the whole CMS detector before hitting the Endcap Muon system (see orientation of the CSC chambers used in the MTCC, Figure 5-3). A muon that hits the ME+1/1 chambers has to have an energy of at least 2 GeV to pass through 2 steel disks to reach the ME+3 station. The approximate cosmic ray muon spectrum $dN/dE_\mu \sim E_\mu^{-2.7}$ [178] is shown in

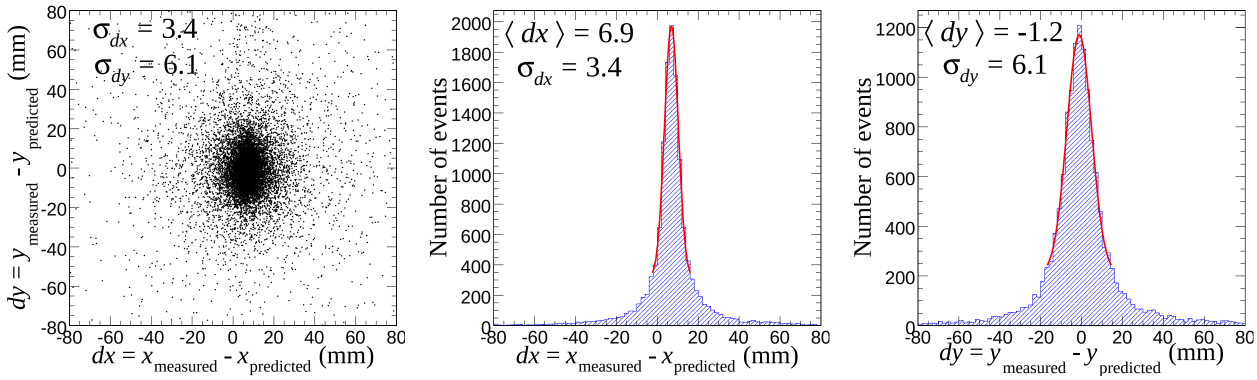

Figure E-3. Muon hit residuals in ME+2/2 chambers after an algorithm search for track segments and applying the "*COG*" technique to find the muon track segment coordinates.

Figure E-4 (left). The additional axis on this plot shows by how much the muon energy spectrum shifts after passing through CMS, just before hitting the ME+1 chambers. The filled area shows only the portion of the spectrum corresponding to muons that can reach the ME+3 chambers. Then, for a muon of a given energy, we calculated the expected, multiple scattering induced, $dN/dx(E_\mu)$-spread between the muon coordinate measured in the ME+2/2 chambers and the coordinate predicted from measurements in the first and third stations. After that, the 2 distributions, $dN/dx(E_\mu)$ and dN/dE_μ, were convoluted. The result for ME+2/2 is shown in Figure E-4 (right). It is clear that the observed residuals are consistent with our simple model. The same level of agreement was observed for other chambers and projections. From these plots, we can conclude that multiple scattering is the dominant contribution to the residuals of the cathode segment measurements. The anode segment measurement precision in ME+2/1 chambers is also dominated by multiple scattering. The large ME+2/2 chambers have wide wire groups, which limits the accuracy of coordinate measurements to 6 mm.

Next, we looked at the number and quality of the found segments (the algorithm allows us to find as many segments as there are in a chamber). Distributions of the numbers of found anode, cathode, and combined 2-dimensional track segments (AS, CS, and TS) in ME+2 chambers are shown in Figure E-5. The seemingly irregular

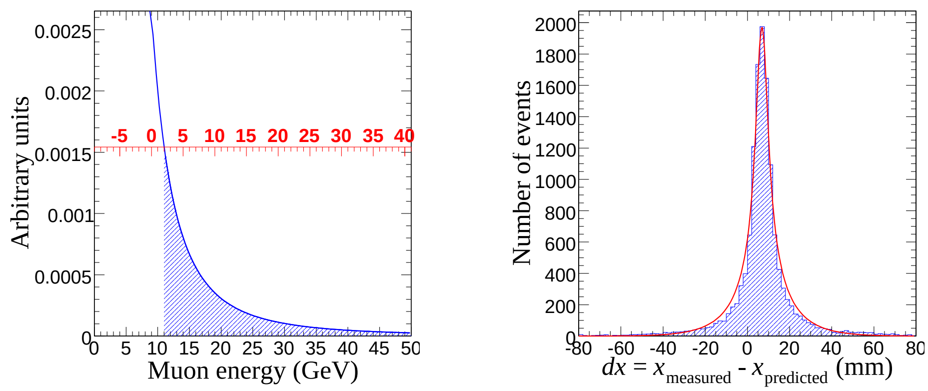

Figure E-4. Cosmic ray muon spectrum (left). Muon hit *dx*-residuals in ME+2/2 chambers (right), where the histogram corresponds to the measured data and the line gives our expectations for the multiple scattering contribution.

pattern of the rightmost plot is driven by combinatorics, not by statistics. In a perfect world when each track going through a chamber would give exactly one ALCT and one CLCT, the only bins that would be populated are $1 \times 1 = 1$ (one track), $2 \times 2 = 4$ (two tracks), $3 \times 3 = 9$ (three tracks), etc. Overlapping tracks in one projection give rise to additinal entries in bins $2 \times (2-1) = 2$, $3 \times (3-1) = 6$, etc. Occasional spurious 1d-LCTs would give the same patterns: $1 \times (1+1) = 2$, $2 \times (2+1) = 6$. Other combinations, like $1 \times 3 = 3$, $1 \times 5 = 5$, $1 \times 7 = 7$, are very rare. This is exactly the pattern we observe.

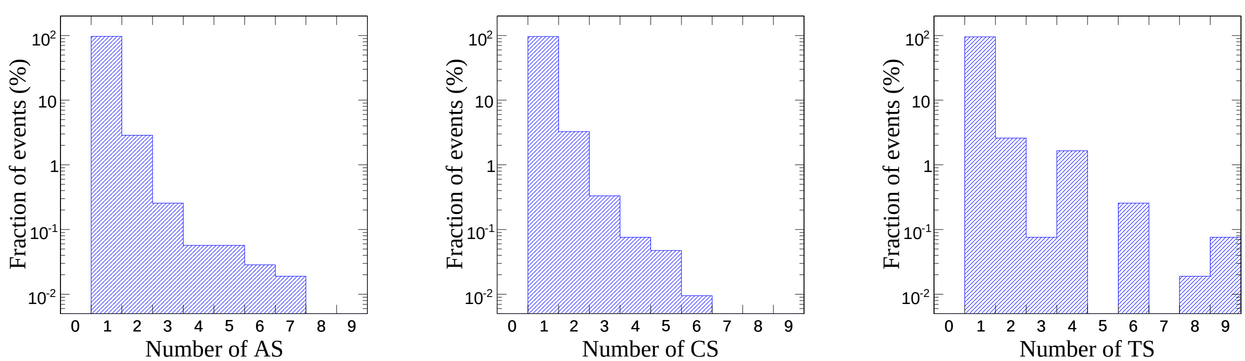

Figure E-5. Distributions of numbers of anode (left), cathode (center), and combined 2-d track segments found in the ME+2 chambers.

Table E-1 shows the numbers of events with different combinations of found segments. About 95% of the events were simple as they had only 1 AS and 1 CS (and, therefore, only 1 2d-TS). All events with multiple segments were visually scanned using an event display. Most of the events with 1 anode segment and 2 cathode segments (and vise versa) looked like they had 2 close-by tracks and the anode (or cathode) segment searching algorithm was not able to separate them. Events with 2 anode segments and 2 cathode segments were either clean 2-track events or more complex broad showers. The final $\approx$1% of events with 3 or more segments in 1 or both projections were all due to broad showers with many hits spread over the chamber. It is worthwhile pointing out that, in cases when there were 2 or more track segments found in the ME+2 chambers, the reconstructed segment closest to the predicted muon track position typically ($>$ 80%) had a better quality than all other segments. Figure E-6 shows the distribution of the pattern qualities for the closest and all other segments.

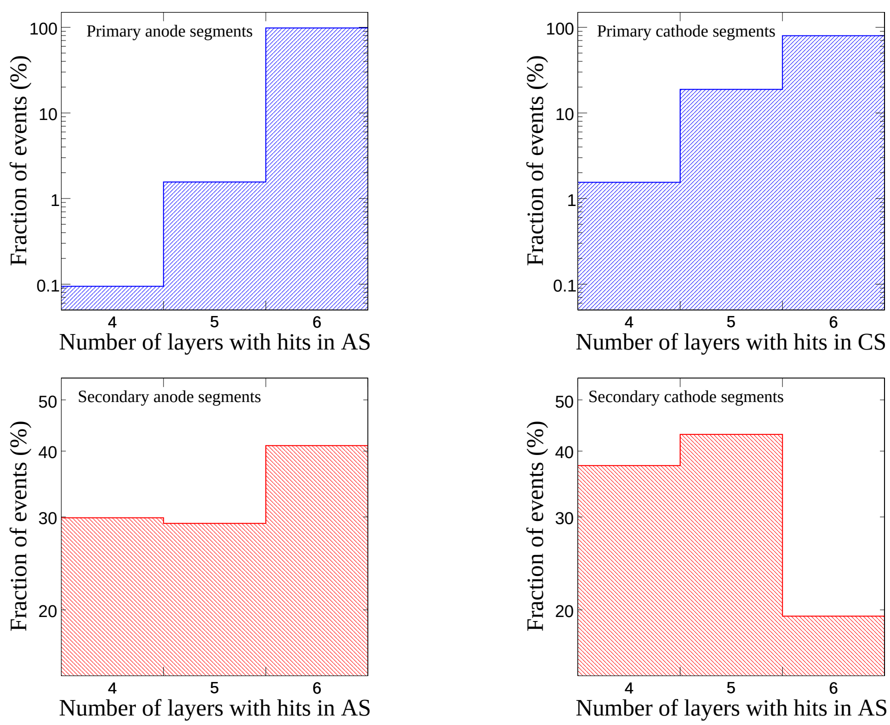

Figure E-6. Quality (number of layers with hits) distributions of primary (upper plots) and secondary (lower plots) segments in ME+2 chambers. The primary segment is the one closest to the predicted muon track position; all others are secondary.

Finally, we benchmarked the CPU performance of the algorithm using MTCC data. The average time required to reconstruct all segments in a chamber with at least 1 track was approximately 0.3 ms (Intel Pentium M 1.6 GHz processor). At this speed, the algorithm is well suited for the High-Level trigger.

Table E-1. Number of events (with fraction in brackets) for different numbers of anode (AS) and cathode (CS) segments in the ME+2 chambers.

ME+2		AS		
		1	2	3 or more
CS	1	10011 (95.1%)	113 (1.1%)	6 (0.06%)
	2	160 (1.5%)	171 (1.6%)	13 (0.12%)
	3 or more	5 (0.05%)	17 (0.16%)	26 (0.25%)

REFERENCES

[1] D. H. Perkins, *Introduction to High Energy Physics*, 4th edition, Cambridge University Press, Cambridge, UK (2000).

[2] D. Griffiths, *Introduction to Elementary Particles*, 2nd edition, Wiley-VCH, Weinheim, Germany, (2008).

[3] A. Bettini, *Introduction to Elementary Particle Physics*, Cambridge University Press, Cambridge, UK (2008).

[4] R. Martin, *Nuclear and Particle Physics*, 2nd edition, John Wiley and Sons Ltd, Chichester, UK (2009).

[5] J. J. Thompson, *Carriers of Negative Electricity*, Nobel Lecture, Royal Swedish Academy of Sciences, Stockholm, Sweden (December 11, 1906).

[6] C. D. Anderson, S. H. Neddermeyer, *Note on the Nature of Cosmic-ray Particles*, Phys. Rev. **51**, 884 (1937).

[7] M. L. Perl, et al. *Evidence for Anomalous Lepton Production in* $e^{+}e$ *Annihilation*, Phys. Rev. Lett. **35**, 1489 (1975).

[8] F. Reines, et al. *Detection of the Free Neutrino: a Confirmation*, Science **124**, 103 (1956).

[9] S. Fukuda, et al., *Constraints on Neutrino Oscillations Using 1258 Days of Super-Kamiokande Solar Neutrino Data*, arXiv.org:hep-ex/0103033 (2001); Phys. Rev. Lett. **86**, 5656 (2001).

[10] S. Fukuda, et al., *Determination of Solar Neutrino Oscillation Parameters Using 1496 Days of Super-Kamiokande-I Data The Super-Kamiokande Collaboration*, arXiv.org:hep-ex/0205075 (2002); Phys. Lett. **B539**, 179 (2002).

[11] KATRIN collaboration, *KATRIN: A Next Generation Tritium Beta Decay Experiment with Sub-eV Sensitivity for the Electron Neutrino Mass*, arXiv.org:hep-ex/0109033 (2001).

[12] C. Amsler, et al. (Particle Data Group), Phys. Lett. **B667**, 1 (2008) and 2009 partial update for the 2010 edition (http://pdg.lbl.gov).

[13] E. Rutherford, *Nuclear Constitution of Atoms*, Proc. Roy. Soc. **A97**, 374 (1920).

[14] J. Chadwick, *The Existence of a Neutron*, Proc. Roy. Soc. **A136**, 692 (1932).

[15] M. Gell-Mann, *A Schematic Model of Baryons and Mesons*, Phys. Lett. **8**, 214 (1964).

[16] G. Zweig, *An $SU(3)$ Model for Strong Interaction Symmetry and Its Breaking*, CERN Report No.8182/TH.401 (1964); *An $SU(3)$ Model for Strong Interaction Symmetry and Its Breaking: II*, CERN Report No.8419/TH.412 (1964).

[17] R. P. Feynman, *Very High-Energy Collisions of Hadrons*, Proceedings of the 3rd Topical Conference on High Energy Collision of Hadrons, Stony Brook, N. Y. (1969); Phys. Rev. Lett. **23**, 1415 (1969).

[18] B. J. Bjrken and S. L. Glashow, *Elementary Particles and $SU(4)$*, Phys. Lett. **11**, 255 (1964).

[19] M. Kobayashi and T. Maskawa, *CP-Violation in the Renormalizable Theory of Weak Interaction*, Prog. Theor. Phys. **49**, 652 (1973).

[20] E. D. Bloom, et al., *High-Energy Inelastic e-p Scattering at 6° and 10°*, Phys. Rev. Lett. **23**, 930 (1969).

[21] M. Breidenbach, et al., *Observed Behavior of Highly Inelastic Electron-Proton Scattering*, Phys. Rev. Lett. **23**, 935 (1969).

[22] J. J. Aubert, et al., *Experimental Observation of a Heavy Particle J*, Phys. Rev. Lett. **33**, 1404 (1974).

[23] J.-E. Augustin, et al., *Discovery of a Narrow Resonance in e^+e^- Annihilation*, Phys. Rev. Lett. **33**, 1406 (1974).

[24] J. A. Appel, et al., *Observation of a Dimuon Resonance at 9.5 GeV in 400-GeV Proton-Nucleus Collisions*, Phys. Rev. Lett. **39**, 252 (1977).

[25] F. Abe, et al. (CDF Collaboration), *Observation of Top Quark Production in $\bar{p}p$ Collisions with the Collider Detector at Fermilab*, Phys. Rev. Lett. **74**, 2626 (1995).

[26] S. Abachi, et al. (D0 Collaboration), *Observation of the Top Quark*, Phys. Rev. Lett. **74**, 2632 (1995).

[27] E. Klempt and A. Zaitsev, *Glueballs, Hybrids, Multiquarks. Experimental Facts Versus QCD Inspired Concepts*, Phys. Rep. **454**, 1 (2007); arXiv.org:hep-ph/0708.4016 (2007).

[28] G. Taubes, *Mastering Nature's Strong Force*, Science **270**, 1756 (1995).

[29] A. Ali, C. Hambrock and M. J. Aslam, *Tetraquark Interpretation of the BELLE Data on the Anomalous $\Upsilon(1S)\pi^+\pi^-$ and $\Upsilon(2S)\pi^+\pi^-$ Production Near the $\Upsilon(5S)$ Resonance*, Phys. Rev. Lett. **104**, 162001 (2010).

[30] C. Semay, F. Buisseret and B. Silvestre-Brac, *Towers of Hybrid Mesons*, Phys. Rev. **D79**, 094020 (2009).

[31] D. Diakonov, V. Petrov, and M. Polyakov, *Exotic Anti-Decuplet of Baryons: Prediction from Chiral Solitons*, Zeitschrift fur Physik **A359**, 305 (1997).

[32] A.R. Dzierba, C.A. Meyer and A.P. Szczepaniak, *Reviewing the Evidence for Pentaquarks*, J. Phys. (Conf. Ser.) **9**, 192 (2005).

[33] G. R. Farrar and G. Zaharijas, *Nuclear and Nucleon Transitions of the H Dibaryon*, Phys. Rev. **D70**, 014008 (2004); arXiv.org:hep-ph/0308137 (2003).

[34] G. R. Farrar, *Detecting Gluino-Containing Hadrons*, Phys. Rev. Lett. **76** 4111 (1996); arXiv.org:hep-ph/9603271 (1996).

[35] I. A. D'Souza and C. S. Kalman, *Preons: Models of Leptons, Quarks and Gauge Bosons as Composite Objects*, World Scientifice, River Edge, NJ, USA (1992).

[36] D. DeCamp et al. (ALEPH Collaboration), *Determination of the Number of Light Neutrino Species*, Phys. Lett. **B231**, 519 (1989).

[37] P. A. M. Dirac, *The Quantum Theory of the Electron*, Proc. Roy. Soc. **A117**, 610 (1928).

[38] C. D. Anderson, *The Positive Electron* Phys. Rev. **43**, 491 (1933).

[39] A.D. Sakharov, *Violation of CP invariance, C asymmetry, and baryon asymmetry of the universe*, Pisma Zh. Eksp. Teor. Fiz. **5**, 32 (1967); Sov. Phys. JETP Lett. **5**, 24 (1967).

[40] S. Weinberg, *Implications of Dynamical Symmetry Breaking*, Phys. Rev. **D13**, 974 (1976).

[41] L. Susskind, *Dynamics of Spontaneous Symmetry Breaking in the Weinberg-Salam Theory*, Phys. Rev. **D20**, 2619 (1979).

[42] H1 Collaboration, *Search for Leptoquark Bosons in ep Collisions at HERA*, arXiv.org:hep-ex/0506044; Phys. Lett. **B629**, 9 (2005).

[43] K. A. Brueckner, *Meson-Nucleon Scattering and Nucleon Isobars*, Phys. Rev. **86**, 106 (1952).

[44] D. P. Barber, et al., *Discovery of Three-Jet Events and a Test of Quantum Chromodynamics at PETRA*, Phys. Rev. Lett. **43**, 830 (1979).

[45] J. C. Maxwell, *A Dynamical Theory of the Electromagnetic Field*, Phil. Tran. Roy. Soc. **155**, 459 (1865).

[46] J. D. Jackson, *Classical Electrodynamics*, 3rd edition, Wiley, New York, USA (1999).

[47] H. Hertz, *Electric Force Radiation (Uber Strahlen elektrischer Kraft)*, Reports of Prussian Academy of Science (Sitzungsberichte der Preussischen Akademie der Wissenschaften) **1888**, 1297, Berlin, Germany (1888).

[48] A. Einstein, *On the Electrodynamics of Moving Bodies (Zur Elektrodynamik bewegter Korper)*, Ann. Phys. (Berlin) **17**, 891 (1905).

[49] H. Hertz, *Ueber Einen Einfluss des Ultravioletten Lichtes auf Die Electrische Entladung*, Ann. Phys. (Berlin) **267**, 983 (1887).

[50] A. Stoletow, *On a Kind of Electrical Current Produced by Ultra-violet Rays*, Phil. Mag. **26**, 317 (1888).

[51] A. Einstein, *On a Heuristic Viewpoint Concerning the Production and Transformation of Light (Uber Einen Die Erzeugung und Verwandlung Des Lichtes Betreffenden Heuristischen Gesichtspunkt)*, Ann. Phys. (Berlin) **17**, 132 (1905).

[52] G. Arnison, et al. (UA1 Collaboration), *Experimental Observation of Isolated Large Transverse Energy Electrons with Associated Missing Energy at* $\sqrt{s}$ = 540 *GeV*, Phys. Lett. **B122**, 103 (1983).

[53] M. Banner (UA2 Collaboration), *Observation of Single Isolated Electrons of High Transverse Momentum in Events with Missing Transverse Energy at the CERN* $\bar{p}p$ *Collider*, Phys. Lett. **B122**, 476 (1983).

[54] F. J. Hasert et al. (Gargamelle Collaboration), *Search for Elastic Muon-neutrino Electron Scattering*, Phys. Lett. **B46**, 121 (1973).

[55] F. J. Hasert et al. (Gargamelle Collaboration), *Observation of Neutrino-like Interactions without Muon or Electron in the Gargamelle Neutrino Experiment* , Phys. Lett. **B46**, 138 (1973).

[56] G. Arnison et al. (UA1 Collaboration), *Experimental Observation of Lepton Pairs of Invariant Mass Around* 95 *GeV/*c^2 *at the CERN SPS Collider*, Phys. Lett. **B126**, 398 (1983).

[57] P. Bagnaia (UA2 Collaboration), *Evidence for* $Z^0 \Rightarrow e^+e$ *at the CERN* $\bar{p}p$ *Collider*, Phys. Lett. **B129**, 130 (1983).

[58] I. Newton, *The Mathematical Principles of Natural Philosophy (Philosophiae Naturalis Principia Mathematica)*, London, UK (July 1686); translated by A. Motte, London, UK (1729); translated by I. B. Cohen and A. Whitman, University of California Press, California, USA (1999).

[59] H. Cavendish, *Experiments to Determine the Density of the Earth*, Phil. Tran. Roy. Soc. **88**, 469 (1798).

[60] A. Einstein, *Gravitation Field (Die Feldgleichungen der Gravitation)*, Sitzungsberichte der Preussischen Akademie der Wissenschaften, Berlin, 844 (1915).

[61] A. Einstein, *Foundation of General Relativity (Die Grundlage der allgemeinen Relativittstheorie)*, Ann. der Phys., **49**, 769 (1916).

[62] F. W. Dyson, A. S. Eddington, C. Davidson, *A Determination of the Deflection of Light by the Sun's Gravitational Field, from Observations Made at the Total Eclipse of 29 May 1919*, Phil. Tran. Roy. Soc. **220A**, 291 (1920).

[63] R. V. Pound, G. A. Rebka Jr., *Gravitational Red-Shift in Nuclear Resonance*, Phys. Rev. Lett. **3**, 439 (1959).

[64] R. V. Pound, G. A. Rebka Jr., *Apparent Weight of Photons*, Phys. Rev. Lett. **4**, 337 (1960).

[65] T. Kundic, et al., *A Robust Determination of the Time Delay in 0957+561A,B and a Measurement of the Global Value of Hubble's Constant*, ApJ. **482**, 75 (1997).

[66] I. I. Shapiro, et al., *Fourth Test of General Relativity: New Radar Result*, Phys. Rev. Lett. **26**, 1132 (1971).

[67] E. B. Fomalont, S. M. Kopeikin, *The Measurement of the Light Deflection from Jupiter: Experimental Results*, ApJ. **598**, 704 (2003).

[68] K. Nordtvedt Jr., *Testing Relativity with Laser Ranging to the Moon*, Phys. Rev. **170**, 1186 (1968).

[69] J. G. Williams, S. G. Turyshev, D. H. Boggs, *Progress in Lunar Laser Ranging Tests of Relativistic Gravity*, Phys. Rev. Lett. **93**, 1017 (2004).

[70] I. Ciufolini, E. C. Pavlis, *A Confirmation of the General Relativistic Prediction of the Lense-Thirring Effect*, Nature, **431**, 958 (2004).

[71] R. A. Hulse, J. H. Taylor, *Discovery of a Pulsar in a Binary System*, ApJ. **195**, 51 (1975).

[72] M. Kramer, et al., *Tests of General Relativity from Timing the Double Pulsar*, Science, **314**, 97 (2006).

[73] B. P. Abbott, et al., *LIGO: the Laser Interferometer Gravitational-Wave Observatory*, Rep. Prog. Phys. **72**, 076901 (2009).

[74] F. Acernese, et al., *Virgo Status*, Class. Quantum Grav. **25**, 184001 (2008).

[75] B. P. Abbott et al. (The LIGO Scientific Collaboration, The Virgo Collaboration), *Searches for Gravitational Waves from Known Pulsars with S5 LIGO Data*, ApJ. **713**, 671 (2010).

[76] S. Perlmutter et al., *Measurements of* Ω *and* Λ *from* 42 *High-Redshift Supernovae*, arXiv.org:astro-ph/9812133 (1998); ApJ. **517**, 565 (1999).

[77] G. Hinshaw et al., *Five-Year Wilkinson Microwave Anisotropy Probe (WMAP) Observations: Data Processing, Sky Maps, and Basic Results* arXiv.org:astro-ph/0803.0732 (2008); ApJ. **180**, 225 (2009).

[78] C. Rovelli, *Notes for a Brief History of Quantum Gravity*, arXiv.org:gr-qc/0006061 (2000).

[79] P. Ramond, *Dual Theory for Free Fermions*, Phys. Rev. **D3**, 2415 (1971).

[80] A. Neveu and J.H. Schwarz, *Factorizable Dual Model of Pions*, Nucl. Phys. **B31**, 86 (1971).

[81] J.L. Gervais and B. Sakita, *Field Theory Interpretation of Supergauges in Dual Models*, Nucl. Phys. **B34**, 632 (1971).

[82] Yu. A. Golfand and E. P. Likhtman, *Extension of the Algebra of Poincare Group Generators and Violation of P invariance*, JETP Lett. **13**, 323 (1971).

[83] J. Wess and B. Zumino, *Supergauge Transformations in Four Dimensions* , Nucl. Phys. **B70**, 39 (1974).

[84] D.V. Volkov and V.P. Akulov, *Is the Neutrino a Goldstone Particle?*, Phys. Lett. **B46**, 109 (1973).

[85] S. Martin, *A Supersymmetry Primer*, arXiv.org:hep-ph/9709356v5 (2008).

[86] H. Baer and X. Tata, *Weak Scale Supersymmetry: From Superfields to Scattering Events*, Cambridge University Press, Cambridge, UK (2006).

[87] I. J. R. Aitchinson, *Supersymmetry in Particle Physics*, Cambridge University Press, Cambridge, UK (2007).

[88] S. Dimopoulos and H. Georgi, *Softly Broken Supersymmetry and SU*(5), Nucl. Phys. **B193**, 150 (1981).

[89] A. H. Chamseddine, R. Arnowitt and P. Nath, *Locally Supersymmetric Grand Unification*, Phys. Rev. Lett. **49**, 970 (1982).

[90] H. Baer, X. Tata and J. Woodside, *Gluino-cascade-decay Signatures at the Fermilab Tevatron Collider*, Phys. Rev. **D41**, 906 (1990).

[91] R. M. Barnetta, J. F. Gunionb and H. E. Haberc, *Discovering Supersymmetry with Like-sign Dileptons*, Phys. Lett. **B315**, 349 (1993).

[92] H. K. Dreiner, M. Guchait and D. P. Roy, *Like Sign Dilepton Signature for Gluino Production at LHC with or without R Conservation*, arXiv.org:hep-ph/9310291 (1993); Phys. Rev. **D49**, 3270 (1994).

[93] M. Guchait and D. P. Roy, *Like Sign Dilepton Signature for Gluino Production at LHC Including Top Quark and Higgs Boson Effects*, arXiv.org:hep-ph/9412329 (1994); Phys. Rev. **D52**, 133 (1995).

[94] H. Baer, C. h. Chen, F. Paige and X. Tata, *Signals for Minimal Supergravity at the CERN Large Hadron Collider II: Multilepton Channels*, arXiv.org:hep-ph/9512383 (1995); Phys. Rev. **D53**, 6241 (1996).

[95] K. T. Matchev and D. M. Pierce , *Supersymmetry Reach of the Fermilab Tevatron via Trilepton, Like-sign Dilepton, and Dilepton Plus Tau Jet Signatures*, arXiv.org:hep-ph/9904282v2 (1999); Phys. Rev. **D60**, 075004 (1999).

[96] K. T. Matchev and D. M. Pierce, *New Backgrounds in Trilepton, Dilepton and Dilepton Plus Tau Jet SUSY Signals at the Tevatron*, arXiv.org:hep-ph/9907505 (1999); Phys. Lett. **B467**, 225 (1999).

[97] J. Done (CMS Collaboration), *Search for Supersymmetry Using Like Sign Dilepton Events at CDF*, FNAL-Thesis-1999-13, Texas A&M University, College Station, TX, USA (1999).

[98] A. A. Affolder, et al. (CDF Collaboration), *Search for Gluinos and Squarks Using Like-Sign Dileptons in p anti-p Collisions at* $\sqrt{s} = 1.8$ *TeV*, arXiv.org:hep-ex/0106061 (2001); Phys. Rev. Lett. **87**, 251803 (2001).

[99] A. Yurkewicz (D∅ Collaboration), *Search for Evidence of Supersymetry in the Like-sign Dimuon Chanel at the D∅ Experiment*, FNAL-Thesis-2004-11, Michigan State University, East Lansing, MI, USA (2004).

[100] M. Worcester (CMS Collaboration), *Inclusive Search for Anomalous High-*p_T *Like-sign Lepton Pair Production at the Fermilab Tevatron Collider*, FNAL-Thesis-2004-05, University of California, Los Angeles, CA, USA (2004).

[101] D. Acosta, et al. (CDF Collaboration), *Inclusive Search for Anomalous Production of High-*p_T *Like-sign Lepton Pairs in p anti-p Collisions at* $\sqrt{s} = 1.8$ *TeV*, arXiv.org:hep-ex/0405063 (2004); Phys. Rev. Lett. **93**, 061802 (2004).

[102] S. Abdullin and F. Charles (CMS Collaboration), *Search for SUSY in (leptons +) Jets + Missing ET Final States*, CMS Note 1998/073 (1998); arXiv.org:hep-ph/9811402 (1998); Nucl. Phys. **B547**, 60-80 (1999).

[103] A. Drozdetski, D. Acosta and G. Mitselmakher (CMS Collaboration), *First Detailed Study on the CMS SUSY Discovery Potential with Two Same-sign Muons in the mSUGRA Model*, CMS AN-2004/003 (2004).

[104] D. Acosta, et al. (CMS Collaboration), *Potential to Discover Supersymmetry in Events with Muons, Jets and Missing Energy in pp Collisions at* $\sqrt{s} = 14$ *TeV with the CMS Detector*, CMS Note 2006/134 (2006).

[105] ALEPH Collaboration, *ALEPH: A Detector for Electron-positron Annihilations at LEP*, Nucl. Instrum. and Methods **A294**, 121 (1990).

[106] DELPHI Collaboration, *The DELPHI Detector at LEP*, Nucl. Instrum. and Methods **A303**, 233 (1991).

[107] L3 Collaboration, *The Construction of the L3 Experiment* , Nucl. Instrum. and Methods **A289**, 35 (1990).

[108] OPAL Collaboration, *The OPAL Detector at LEP*, Nucl. Instrum. and Methods **A305**, 275 (1991).

[109] ALEPH Collaboration, *Search for Scalar Leptons in $e^+ e$ Collisions at Centre-of-mass Energies up to 209 GeV* Phys. Lett. **B526**, 206 (2002).

[110] DELPHI Collaboration, *Searches for Supersymmetric Particles in $e^+ e^-$ Collisions up to 208 GeV and Interpretation of the Results within the MSSM*, Eur. Phys. J. **C31**, 421 (2003).

[111] L3 Collaboration, *Search for Scalar Quarks and Scalar Leptons at LEP*, Phys. Lett. **B580**, 37 (2004).

[112] OPAL Collaboration, *Search for Anomalous Production of Dilepton Events with Missing Transverse Momentum in $e^+ e^-$ Collisions at $\sqrt{s} = 183$ GeV to 209 GeV*, Eur. Phys. J. **C32**, 453 (2004).

[113] ALEPH Collaboration, DELPHI Collaboration, L3 Collaboration and OPAL Collaboration, Proceedings of the XXXVI Rencontres de Moriond, Electroweak Interactions and Unified Theories, Les Arcs, France, March 11–17 (2001).

[114] F. Abe, et al. (CDF Collaboration), *The CDF Detector: an Overview*, Nucl. Instrum. and Methods **A271**, 387 (1988).

[115] R. Blair, et al. (CDF Collaboration), *The CDF-II detector: Technical Design Report*, FERMILAB-PUB-96-390-E (1996).

[116] D. Acosta, et al. (CDF Collaboration), *Measurement of the J/ψ Meson and b-hadron Production Cross Sections in $p\overline{p}$ Collisions at $\sqrt{s} = 1960$ GeV*, Phys. Rev. **D71**, 032001 (2005).

[117] S. Abachi, et al (D∅ Collaboration), *The D∅ Detector*, Nucl. Instrum. and Methods **A338**, 185 (1994).

[118] S. Abachi, et al (D∅ Collaboration), *The D∅ Upgrade: the Detector and Its Physics*, FERMILAB-PUB-96-357-E (1996).

[119] V. Abazov, et al (D∅ Collaboration), *The Upgraded D∅ Detector*, Nucl. Instrum. and Methods **A565**, 463 (2006).

[120] D∅ Collaboration, *Search for Squarks and Gluinos in Events with Jets and Missing Transverse Energy Using 2.1 fb^{1} of $p\bar{p}$ Collision Data at $\sqrt{s} = 1.96$ TeV*, Fermilab-PUB-07/668-E; arXiv.org:hep-ex/0712.3805 (2007); Phys. Lett. **B660**, 449 (2008).

[121] T. Aaltonen, et al. (CDF Collaboration), *Inclusive Search for Squark and Gluino Production in $p\bar{p}$ Collisions at $\sqrt{s}$ = 1.96 TeV*, CDF Note 9229; arXiv.org:hep-ex/0811.2512v1 (2008); Phys. Rev. Lett. **102**, 121801 (2009).

[122] T. Aaltonen, et al. (CDF Collaboration), *Search for Supersymmetry in $p\bar{p}$ Collisions at $\sqrt{s}$ = 1.96 TeV Using the Trilepton Signature for Chargino-Neutralino Production*, CDF Note 9176; Phys. Rev. Lett. **101**, 251801 (2008).

[123] S. Somalwar, et al. (CDF Collaboration), *SUSY Searches at Tevatron*, Proceedings of *XX*th Hadron Collider Physics Symposium, Evian, France (November, 2009).

[124] D∅ Collaboration, *Search for Associated Production of Charginos and Neutralinos in the Trilepton Final State Using* 2.3 fb^{-1} *of Data*, Fermilab-PUB-09/003-E (2009); arXiv.org:hep-ex/0901.0646 (2009); Phys. Lett. **B680**, 34 (2009).

[125] The LHC study group, *The Large Hadron Collider: Conceptual Design*, CERN/AC 1995-05 (1995).

[126] L. Evans and P. Bryant (LHC Collaboration), *LHC Machine*, JINST **3**, S08001 (2008).

[127] The CMS Collaboration, *CMS, the Compact Muon Solenoid: Technical Proposal*, CERN/LHCC 1994-038 (1994).

[128] S. Chatrchyan, et.al. (CMS Collaboration), *The CMS Experiment at the CERN LHC*, JINST **3**, S08004 (2008).

[129] *LHC Energy consumption*, http://lhc-machine-outreach.web.cern.ch/lhc-energy-consumption.htm (2007).

[130] Proceedings of the LHC Performance Workshop, Chamonix, France, 25-29 January (2010).

[131] *Gainesville Regional Utilities Annual Report 2007-2008*, http://www.gru.com/Pdf/AnnualReport2008/2007-2008_GRU_Annual_Report.pdf (2008).

[132] The CMS Collaboration, *The Muon Project Technical Design Report*, CERN/LHCC 1997-032 (1997).

[133] M.C. Fouz, et al., *The CMS Muon System*, Nucl. Instr. and Meth. **A446**, 366 (2000).

[134] The CMS Collaboration, *CMS Physics Technical Design Report Volume 1: Detector Performance and Software*, CERN/LHCC 2006-001 (2006).

[135] D. Acosta, et al., *Large CMS Cathode Strip Chambers: Design and Performance*, Nucl. Instrum. and Methods **A453**, 182 (2000).

[136] Yu. Erchov, et al., *Cathode Strip Chamber for CMS ME1/1 Endcap Muon Station*, Phys. of Part. and Nucl. Lett. **3**, 73 (2006).

[137] G. Charpak, et al., *High-accuracy Localization of Minimum Ionizing Particles Using the Cathode-induced Charge Centre-of-gravity Read-out*, Nucl. Instrum. and Methods **167**, 455 (1979).

[138] M.M. Baarmand, et al., *Spatial Resolution Attainable with Cathode Strip Chambers at the Trigger Level*, Nucl. Instrum. and Methods **A425**, 92 (1999).

[139] D. Lazic, et al., (CMS Collaboration), *The CMS Magnet Test and Cosmic Challenge (MTCC) Operational Experience and Lessons Learnt*, CMS NOTE-2007/005 (2007); Nuclear Physics, **B172**, 3 (2007).

[140] The CMS Collaboration, *Measurement of the charge ratio of atmospheric muons with the CMS detector*, arXiv.org:hep-ex/1005.5332v1 (2010), CMS PAS MUO-10-001 (2010), submitted to Phys. Lett. B.

[141] The CMS Collaboration, *Performance of CMS Muon Reconstruction in Cosmic-ray Events*, arXiv.org:physics.ins-det/0911.4994v2 (2009), JINST **5**, T03022 (2010).

[142] The CMS Collaboration, *First Measurement of the Underlying Event Activity at the LHC with* $\sqrt{s} = 0.9$ *TeV*, arXiv.org:hep-ex/1006.2083 (2010); CMS-QCD-10-001 (2010); CERN-PH-EP-2010-014 (2010).

[143] The CMS Collaboration, *First Measurement of Bose-Einstein Correlations in Proton-Proton Collisions at* $\sqrt{s} = 0.9$ *TeV and* $\sqrt{s} = 2.36$ *TeV at the LHC*, CMS-QCD-10-003 (2010); CERN-PH-EP-2010-010 (2010); arXiv.org:hep-ex/1005.3294 (2010); Phys. Rev. Lett. **105**, 032001 (2010).

[144] The CMS Collaboration, *Transverse Momentum and Pseudorapidity Distributions of Charged Hadrons in pp Collisions at* $\sqrt{s} = 0.9$ *TeV and* $\sqrt{s} = 2.36$ *TeV*, CMS-QCD-09-010 (2009); CERN-PH-EP-2010-003 (2010); arXiv.org:hep-ex/1002.0621 (2010); J. High Energy Phys. **02**, 041 (2010).

[145] The CMS Collaboration, *J/ψ Prompt and Non-prompt Cross Sections in pp Collisions at* $\sqrt{s} = 7$ *TeV*, CMS-PAS-BPH-10-002 (2010).

[146] The CMS Collaboration, *Measurement of the W and Z Inclusive Production Cross Sections at* $\sqrt{s} = 7$ *TeV with the CMS Experiment at the LHC*, CMS-PAS-EWK-10-002 (2010).

[147] D. Barge, et al. (CMS Collaboration), *Data Driven Background Study for New Physics Searches with Same Sign Dileptons at* $\sqrt{s} = 10$ *TeV*, CMS AN-2009/138 (2009).

[148] A. G. Bryer, et al. (CMS Collaboration), *Search for Supersymmetry in Same-Sign Dilepton Final States with CMS Detector at LHC*, CMS AN-2009/168 (2009).

[149] D. Barge, et al. (CMS Collaboration), *SUSY Sensitivity and Discovery Potential Using di-leptons at $\sqrt{s} = 7$ TeV*, CMS AN-2010/077 (2010).

[150] B.C. Allanach, *SOFTSUSY: A Program for Calculating Supersymmetric Spectra*, arXiv.org:hep-ph/0104145 (2001).

[151] M. Muhlleitner, A. Djouadi, Y. Mambrini, *SDECAY: A Fortran Code for the Decays of the Supersymmetric Particles in the MSSM*, arXiv.org:hep-ph/0311167 (2003).

[152] A. Djouadi, M.M. Muhlleitner, M. Spira, *Decays of Supersymmetric Particles: The Program SUSY-HIT (SUspect-SdecaY-Hdecay-InTerface)*, arXiv.org:hep-ph/0609292 (2006).

[153] T. Sjostrand and S. Mrenna and P. Skands, *PYTHIA 6.4 Physics and Manual*, arXiv.org:hep-ph/0603175 (2006).

[154] D. Stump, et al., *Inclusive Jet Production, Parton Distributions, and the Search for New Physics*, arXiv.org:hep-ph/0303013 (2003).

[155] W. Beenakker, R. Hoepker and M. Spira, *PROSPINO: A Program for the Production of Supersymmetric Particles in Next-to-leading Order QCD*, arXiv.org:hep-ph/9611232 (1996).

[156] J. Alwall, et al., *MadGraph/MadEvent v4: The New Web Generation*, arXiv.org:hep-ph/0706.2334 (2007); JHEP **9**, 028 (2007).

[157] The CMS Collaboration, *The Trigger and Data Acquisition project, Volume I. The Level-1 Trigger, Technical Design Report*, CERN/LHCC 2000-038 (2000).

[158] The CMS Collaboration, *The Trigger and Data Acquisition project, Volume II. Data Acquisition and High-Level Trigger*, CERN/LHCC 2002-026 (2002).

[159] The CMS Collaboration, *Trigger Menus for "Trigger Reviews", v0.2: 8E29, 1E31 in 3_0_x (10 TeV with startup conditions)*, https://twiki.cern.ch/twiki/bin/view/CMS/TSG_24_XI_08 (2008).

[160] The CMS Collaboration, *Lean trigger menus v0.3 (10 TeV, startup conditions)*, https://twiki.cern.ch/twiki/bin/view/CMS/TSG_18_II_09 (2009).

[161] G. Abbiendi, et al. (CMS Collaboration), *Muon Reconstruction in the CMS Detector*, CMS AN 2008/097 (2008).

[162] D. Barge, et al. (CMS Collaboration), *Muon Identification in CMS*, CMS AN 2008/098 (2008).

[163] The CMS Collaboration, *V+Jets Cross-PAG. Baseline Event Selection*, https://twiki.cern.ch/twiki/bin/view/CMS/VplusJets (2008).

[164] S. Baffioni, et al. (CMS Collaboration), *Electron Reconstruction in CMS*, Eur. Phys. J. **C49**, 1099 (2007).

[165] W. Adam, et al. (CMS Collaboration), *Reconstruction of Electron with the Gaussian-Sum Filter in the CMS Tracker at the LHC*, CMS NOTE 2005/001 (2005).

[166] S. Abdullin, A. Drozdetskiy, et al., *GARCON: Genetic Algorithm for Rectangular Cuts OptimizatioN. User's Manual for Version 2.0*, arXiv.org:hep-ph/0605143 (2006).

[167] R. Remington, et al. (CMS Collaboration), *Data-driven Estimation of the QCD Background in a SUSY Search with 2 Same-sign Muons*, CMS AN-2010/058 (2010).

[168] R. Remington, et al. (CMS Collaboration), *Commissioning the Data-driven Estimation of the QCD Background in Di-Muon SUSY Searches with 7 TeV Collision Data*, CMS AN-2010/170 (2010).

[169] D. Dobur, et al. (CMS Collaboration), *Data-driven Estimation of Muon Isolation Efficiency Using b-jets from QCD*, CMS AN-2010/169 (2010).

[170] D. Dobur, et al. (CMS Collaboration), *Comissioning of a Measurement of Muon Isolation Using b-jets at 7 TeV*, CMS AN-2010/185 (2010).

[171] D. Barge, et al. (CMS Collaboration), *Data Driven Background Study for New Physics Searches with Same Sign Dileptons at* $\sqrt{s}$ *= 10 TeV*, CMS AN-2009/138 (2009); report by P. Kalavase on Leptonic SUSY CMS meeting, http://indico.cern.ch/conferenceDisplay.py?confId=71418 (October 21st, 2009).

[172] The CMS Collaboration, *The CMS physics Reach for Searches at 7 TeV*, CMS NOTE 2010/008 (2010).

[173] D. Acosta, et.al., *Efficiency of Finding Muon Track Trigger Primitives in CMS Cathode Strip Chambers*, CMS Note 2007/031 (2007); Nucl. Instrum. and Methods **A592**, 26-37 (2008).

[174] D. Acosta, et.al. (CMS Collaboration), *Performance of the CMS Cathode Strip Chambers with Cosmic rRys* , JINST **5**, T03018 (2010).

[175] D. Acosta, et.al. (CMS Collaboration), *Design Features and Test Results of the CMS Endcap Muon Chambers*, Nucl. Instrum. and Methods **A94**, 504 (2002).

[176] G. Alverson, et al., *IGUANA Architecture, Framework and Toolkit for Interactive Graphics*, arXiv.org:cs.se/0306042 (2003); ECONF, C0303241, (2003).

[177] W. Adam, et al. (SUSY group, CMS Collaboration), *Search for Single-Lepton SUSY Signatures (RA4): Background Determinations*, https://twiki.cern.ch/twiki/bin/view/CMS/SusyRA4SingleLeptonOrganization (2009).

[178] O.C. Allkofer, et al., *The Absolute Cosmic Ray Muon Spectrum at Sea Level*, Phys. Lett. **B36** 425 (1971).

BIOGRAPHICAL SKETCH

Yuriy Pakhotin was born on May 8th, 1977, in the city of Berdsk which is located in Novosibirsk region of Russia. In the same year his family moved to the city of Tselinograd (now Astana) in Kazakhstan. After graduation with honors from high school in 1994 he moved back to Siberia and began undergraduate study at the Novosibirsk State University (Novosibirsk, Russia).

Under supervision of Prof. Guram Kezerashvili he wrote bachelor's thesis "Position Monitor for the High Energy Gamma-quanta Beam" and graduated with honor in 1998. Then he entered the Master program in High Energy Physics at the same university that he finished with honor in 2000. The title of his master's thesis was "Development of the Interaction System of Laser Radiation and Positron Beam at VEPP-4M Collider". For the next 3 years he worked at the Budker Institute for Nuclear Physics (Novosibirsk, Russia) as a research assistant and at the Novosibirsk State University as a teaching assistant. In 2003 he entered the Doctorate program in High Energy Physics at the University of Florida (Gainesville, Florida).

Under supervision of Prof. Guenakh Mitselmakher and co-supervision of Prof. Andrey Korytov he wrote doctor's thesis "Compact Muon Solenoid Experiment Discovery Potential for Supersymmetry in Same-charge Di-lepton Events". In August 2010 he graduated with Doctor of Philosophy degree from the University of Florida.